2020

Boron Isotopes and FTIR Analysis to Determine Past Fire Occurrence in the Upper Nepean Catchment

Rebecca Ryan
University of Wollongong

Boron Isotopes and FTIR Analysis to Determine Past Fire Occurrence in the Upper Nepean Catchment

Abstract

Bushfires have shaped the Australian landscape for millennia and with increasing concerns surrounding the effects of climate change on national fire regimes, the importance of developing more extensive fire records becomes critical in management and mitigation. Existing methods are historically limited or prevent distinction of severity, hindering a continuous, long-term record of past fire activity. The aim of this study was to calibrate two novel techniques- boron isotopes and Fourier Transform Infrared (FTIR) spectroscopy- against known fire occurrence in alluvial sediments to determine their suitability as proxies. Alluvial sediments provide an insight into signal transport to reservoirs and lake sediments, which offer an enduring record of past fire activity. This study employed both geochemical and infrared spectroscopy analysis techniques to determine changes in the boron isotope ratio (δ11B) and molecular composition of the sediment profile with depth. A methods comparison was conducted with potassium bromide (KBr) discs and attenuated total reflectance (ATR)-FTIR. Clay samples underwent alkali fusion, cation exchange and boron specific chromatography and analysis by multicollector inductively coupled plasma mass spectrometry (MC-ICP-MS) for the determination of δ11B values. The results from the FTIR proxy highlight the exposure of charcoal-rich layers to higher temperatures and pyrolysis conditions, largely effecting C-C, C-N and C-O bonds by thermal decomposition. Higher severity is also punctuated by a shift from aliphatic to aromatic compounds- a trait associated with higher temperatures. In association with this, boron isotopes highlighted a significant peak in δ11B value at the surface of the charcoal-rich layer, suggesting enrichment of 11B from ash or the temperature-induced transformations of boric acid, resulting in speciation and fractionation. This speciation is confirmed in the FTIR spectra.

Degree Type

Thesis

Degree Name

Bachelor of Science (Honours)

Department

School of Earth, Atmospheric and Life Sciences

Advisor(s)

Anthony Dosseto

Keywords

Geochemistry

Boron Isotopes and FTIR Analysis to Determine Past Fire Occurrence in the Upper Nepean Catchment

A thesis submitted in partial fulfilment of the requirements for the award of the degree of BACHELOR OF SCIENCE (HONOURS)

By Rebecca Ryan (5415755)

Supervisor: Professor Anthony Dosseto

SCHOOL OF EARTH, ATMOSPHERE AND LIFE SCIENCES

FACULTY OF SCIENCE, MEDICINE AND HEALTH

THE UNIVERSITY OF WOLLONGONG

October 2020

UNIVERSITY OF WOLLONGONG AUSTRALIA

The information in this thesis is entirely the result of investigations conducted by the author, unless otherwise acknowledged, and has not been submitted in part, or otherwise, for any other degree or qualification.

Rebecca Ryan

7th October 2020

Acknowledgements

It is not without the support of many that this year has been possible. Firstly, I would like to acknowledge and thank my supervisor Professor Anthony Dosseto for all his support, guidance, encouragement and ongoing feedback throughout the year. Thank you for being so enthusiastic and allowing me to experience so many great opportunities from the field to the lab. In addition, I would like to thank Shawn Lu for showing me the ropes in the lab and assisting with field work.

Thank you to Pavel Dlapa and Ivan Šimkovic from Comenius University for assisting with FTIR interpretation and analysis by KBr discs. I would also like to thank Matt Forbes for all your help with the TCN analyser as well as Ross Bradstock, Owen Price and Rebecca Gibson (NSW DPIE) for aiding with access to fire severity maps. Thank you to Scott Mooney and Mark Constantine from UNSW for their assistance with baseline-correction of FTIR spectra.

In addition, my thanks go to Florian Dux and Alex Franke for all your help in the lab and for always being up for a laugh. I would also like to acknowledge Mark Quoyle for assisting with fieldwork as well as Beau Byers, Gabby Apps, Florian Dux and Dafne Koutamanis for reading my thesis and providing feedback.

Special thanks to close family and friends who have supported me throughout the year. Particular thanks to my mother Debbie and brother Tim for supporting me through the stressful times and celebrating my wins. I am so grateful to have you both as my number one supporters.

Abstract

Bushfires have shaped the Australian landscape for millennia and with increasing concerns surrounding the effects of climate change on national fire regimes, the importance of developing more extensive fire records becomes critical in management and mitigation. Existing methods are historically limited or prevent distinction of severity, hindering a continuous, long-term record of past fire activity. The aim of this study was to calibrate two novel techniques- boron isotopes and Fourier Transform Infrared (FTIR) spectroscopy- against known fire occurrence in alluvial sediments to determine their suitability as proxies. Alluvial sediments provide an insight into signal transport to reservoirs and lake sediments, which offer an enduring record of past fire activity.

This study employed both geochemical and infrared spectroscopy analysis techniques to determine changes in the boron isotope ratio ($\delta^{11}B$) and molecular composition of the sediment profile with depth. A methods comparison was conducted with potassium bromide (KBr) discs and attenuated total reflectance (ATR)-FTIR. Clay samples underwent alkali fusion, cation exchange and boron specific chromatography and analysis by multicollector inductively coupled plasma mass spectrometry (MC-ICP-MS) for the determination of $\delta^{11}B$ values.

The results from the FTIR proxy highlight the exposure of charcoal-rich layers to higher temperatures and pyrolysis conditions, largely effecting C-C, C-N and C-O bonds by thermal decomposition. Higher severity is also punctuated by a shift from aliphatic to aromatic compounds- a trait associated with higher temperatures. In association with this, boron isotopes highlighted a significant peak in $\delta^{11}B$ value at the surface of the charcoal-rich layer, suggesting enrichment of ^{11}B from ash or the temperature-induced transformations of boric acid, resulting in speciation and fractionation. This speciation is confirmed in the FTIR spectra.

Table of Contents

List of Figures

List of Appendix

List of Tables

1 Introduction

The term “fire regime” has gained more common usage in literature in recent decades; its definition evolving with advances in our understanding (Krebs *et al.*, 2010; Sawyer *et al.*, 2018a). Fire regimes can be defined as a collection of several fire-related components that determine ecosystem and landscape response following fire. These components include i) time since last fire (the amount of time elapsed since the last fire occurrence at a given site), ii) frequency (the number of fires occurring within a given unit of time), iii) intensity (the energy output of the event), iv) seasonality (the timing of fire events in relation to annual changes in climate) (Sawyer *et al.*, 2018a), v) type (whether the fire is occurring above or below ground or at a canopy level) and vi) severity (the amount of material consumed) (Gosling, Cornelissen and McMichael, 2019). In severe cases, the effects of fire on the landscape may be permanent (Certini, 2005; Gosling, Cornelissen and McMichael, 2019).

A fire event may stem from natural or anthropogenic origins. Natural fire events are controlled by a combination of climate and vegetation (Earl and Simmonds, 2017) or could be ignited by lightning strikes. Fire has played an important role in the evolution of humans, with detection in the geological record occurring as early as the Carboniferous. Over the past 25 000 years, however, fire activity across a number of geological regions has seen an increase in prevalence, likely as a result of anthropogenic activity (Gosling, Cornelissen and McMichael, 2019), either in the form of arson or prescribed burning for management (Earl and Simmonds, 2017). Prescribed fires are typically low to moderate in severity, limiting their effects to the understorey (Sawyer *et al.*, 2018b) and can promote rejuvenation of vegetation, remove undesired species and increase available nutrients. There are no long term or irreversible changes to the ecosystem, however, the temperature of the fire may alter the hydrophobicity of the soil, promoting water runoff and decreased absorption (Certini, 2005). This is in contrast with high severity fires in which the canopy is completely consumed by fire (Certini, 2005; Sawyer *et al.*, 2018a). High severity fires are also characterised by a significant reduction in organic matter, loss of structure and porosity of soil, leaching and nutrient loss due to volatilisation (Figure 1.1) (Certini, 2005).

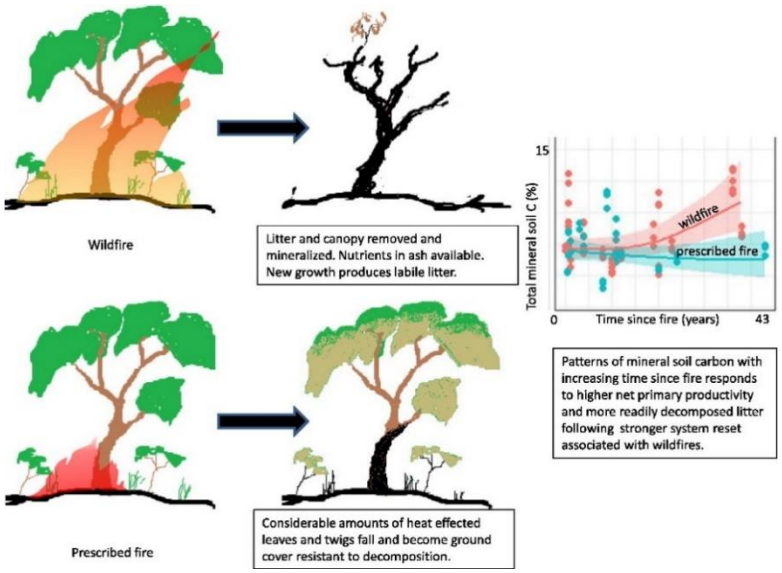

Figure 1.1 Graphical representation of the varying effects of a high-severity fire (wildfire) contrast to low severity fires (prescribed fires) (Sawyer *et al.*, 2018a).

As global environments continue to diversify in response to climate change, it is expected that fire regimes, too, will experience modifications at local, regional and national scales (Bento-Gonçalves *et al.*, 2012) Australia maintains status as the most fire-prone continent globally, with an immense variation of fire regimes across the nation (Bradstock, 2010). High frequency, low severity fires dominate in the north whilst low frequency, high severity fires are more prevalent in the south (Bradstock, 2010). Drought and large scale rainfall events further intensify the variation of fire regimes (Bradstock, 2010). Global climatic change is largely the result of atmospheric circulation phenomena, with the El Niño Southern Oscillation (ENSO) and Indian Ocean Dipole (IOD) acting as the dominant climatic drivers in the Australian context (Bradstock, 2010; Bradstock *et al.*, 2014). Both of these phenomena have been known to alter the vegetation through fluctuations in rainfall from changed sea surface temperatures (White *et al.*, 2006). ENSO is measured using the Southern Oscillation Index (SOI), calculated as the normalised difference between the average sea level pressures between both Darwin and Tahiti. A negative SOI causes an El Niño event in the south-east of Australia, resulting in significant rainfall deprivation and promoting drought and bushfires (Mariani *et al.*, 2016). The Pacific Decadal Oscillation (PDO) has also been known to contribute to changes in rainfall. ENSO and PDO-related droughts have resulted in landscape-scale bushfires (Figure 1.2) (White *et al.*, 2006) due to altered fuel loads, plant productivity and decomposition of organic matter (Bradstock, 2010; Earl and Simmonds, 2017; Sawyer *et al.*, 2018b). Additionally, changes to atmospheric circulation determine whether the region is fuel-limited, or moisture limited. A fuel-limited system constrains progression and ignition of fires to fuel availability whilst moisture limited systems result from excess moisture, confining the fire activity to drier areas (Nelson, 2010). Frequency of lightning-induced fires may also be effected under changed climatic conditions (Bradstock, 2010). Existing climate models

suggest an increase in temperature in eucalypt forests accompanied by a possible change in precipitation at a local level in the future. This could significantly increase fire activity across much of Australia (Sawyer *et al.*, 2018b).

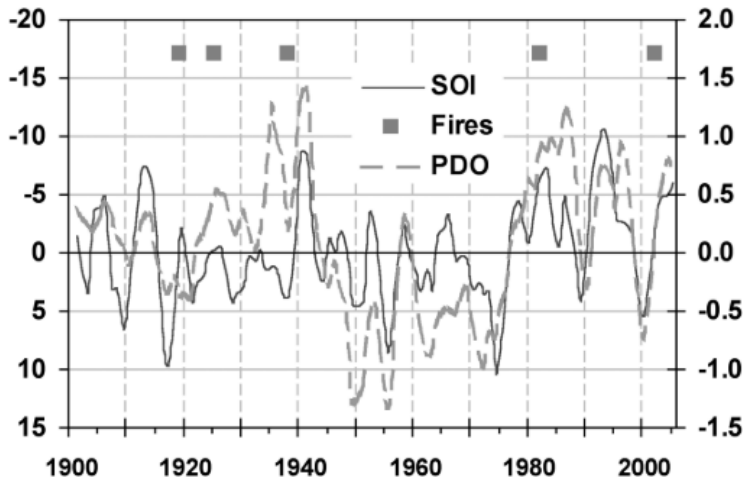

Figure 1.2 The relation between averages in the Southern Oscillation Index (SOI) and Pacific Decadal Oscillation (PDO) with respect to major fire severity in the Cotter Catchment in the Australian Capital Territory (ACT) (White *et al.*, 2006).

Fires have the potential, not only to devastate townships, infrastructure and ecosystems but they also have an extensive effect on water catchments by significantly reducing yield and increasing turbidity of reservoirs and streams that feed high-quality drinking water supplies (White *et al.*, 2006). Initially, the response of a catchment to a severe fire event is an increase in yield due to elevated hydrophobicity of the soil combined with increased runoff from rainfall (White *et al.*, 2006). This gives rise to the mobilisation of large quantities of ash, sediment, organic material and dissolved materials which causes an immediate increase in turbidity as well as the potential input of excess nutrients such as nitrogen and phosphorus (Mariani *et al.*, 2016). In excess, these nutrients can result in eutrophication of waterways, corrosion of copper pipes for water transport and poses an immediate risk to human health by affecting the oxygen transport capacity of red blood cells (Mariani *et al.*, 2016). In addition, elevated turbidity can hinder the accurate detection of bacteria and viruses in the water, promote bacterial growth and prevent the successful disinfection of the water. This is of particular concern since large quantities of the water collected in catchments supply potable drinking water to various populations (Smith *et al.*, 2011).

Revegetation of a catchment can occur over varying time durations and is heavily dependent on the dominant species of the catchment (Heath *et al.*, 2016). Catchments in which rapid-recovery resprouter species dominate experience a marked difference in hydrological response post-fire which contrasts with those dominated by obligate seeder species (Heath *et al.*, 2016). Since obligate seeders require more extensive time periods to regain root structures with the equivalent capacity to maintain

soil structure as the pre-fire state, these catchments tend to experience extensive erosion and multi-decadal water yield losses post-fire. In contrast, rapid-resprouter dominated catchments experience only minor erosional events and short term water yield deficits (Heath *et al.*, 2016). The ability to identify and predict major fire events is, thus, of major importance in allowing for the implementation of fire response and preparedness plans, as well as mitigation measures for post-fire recovery (Doerr *et al.*, 2014).

With dynamic climate, the extensive nature and large-scale impacts of fire emphasise a need for accurate and evolving modelling techniques. Many of the existing models rely on remote sensing data, limiting the fire record to the last 20-40 years (Morgan *et al.*, 2014) or the analysis of charcoal in its various forms. Whilst charcoal analysis is the most common method for identifying fire occurrence, it lacks the ability to determine severity and smaller fragments are easily mobilised by wind or water, thus resulting in an incomplete record of past fire activity. Investigation of new methods for reconstructing past fire severity and occurrence is therefore required to increase preparedness and meditative measures for future fire events.

1.1 Aims and Objectives

The aim of this study is to calibrate two novel techniques- boron isotopes and Fourier Transform Infrared (FTIR) spectroscopy against known fire occurrence in the Upper Nepean Catchment to determine their suitability as proxies. This was achieved using the following key objectives:

i) Determine changes in $\delta^{11}B$ and molecular composition with depth to identify fire-induced changes.
ii) Determine changes in molecular composition between fractions to identify changes with depth, identifying the effects of fire on the matrix.
iii) Determine the ability of the two proxies to substantiate the 2013 bushfire.
iv) Compare FTIR methods to determine variation between instruments.

This study also aimed to compare results against two existing methods for determining past fire occurrence- radiocarbon dating and total carbon and nitrogen analysis, to identify advantages and advances in understanding using these novel methods. This was achieved using the following objectives:

i) Compare results from samples collected from different times since last fire and sites.
ii) Determine reproducibility and additional understanding gained between proxies.

If successful, these proxies have the potential to significantly extend our fire record and allow for the formulation of more accurate models of future fire events.

2 Literature Review

2.1 Introduction

Few methods have been employed to determine past fire occurrence in alluvial depositional environments. By analysing alluvial sediments, the role of material transport and, ultimately, the signal of the proxy, can be understood before application to reservoir and lake sediments which will provide a more long-term record. Boron isotopes and Fourier Transform Infrared (FTIR) spectroscopic analysis have been investigated for quantification as proxies against known fire occurrence and have shown some success in previous studies, as outlined in the remainder of this chapter.

2.2 Existing Alluvial Methods

Fires have the capacity to significantly alter the flow of water and sediment in alluvial systems through the removal of vegetation, causing instability that can be detected through analysis of the hydrograph and channel evolution pre- and post-fire (Prosser, 1987; Meyer *et al.*, 1992; Pierce, Meyer and Jull, 2004; Eaton *et al.*, 2010). High severity fires are distinguished by the complete consumption of the canopy of the vegetation, resulting in mineralisation in the form of ash (Sawyer *et al.*, 2018a). This process is accompanied by the addition of combustion residues (Meyer *et al.*, 1992), loss of organic material, leaching, loss of nutrients due to volatilisation (Certini, 2005) and increased water repellence (Figure 2.1) (Shakesby *et al.*, 2003)

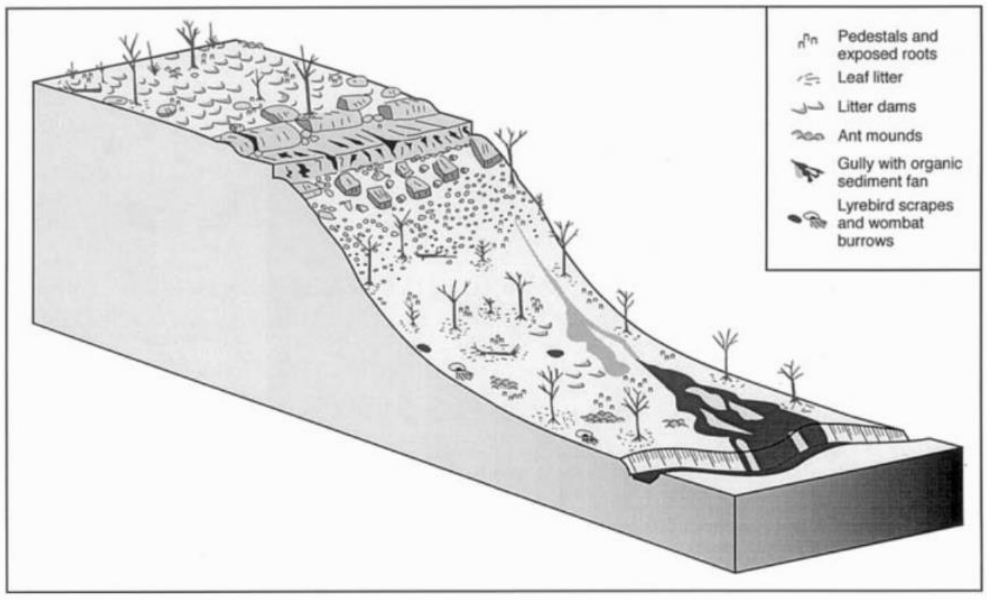

Figure 2.1 Schematic image of the erosional features that developed in the post-fire landscape of the Blue Gum Creek Valley of New South Wales (Shakesby *et al.*, 2003).

If a high severity fire event is followed in short succession by a significant storm or rainfall event, these changes can be detected on the hydrograph in the form of a peak due to increased runoff and overland flow. This has a notably larger magnitude than a rainfall or storm event alone (Figure 2.2) (Prosser,

1987). This analysis of the hydrograph can also be accompanied by field studies analysing changes to the channel width and depth over time. One method has employed an automatic level, stadia rod and tape measure with fixed benchmarks to conduct a yearly survey determining pre- and post-fire variations and comparing results against the hydrograph to explain trends (Eaton *et al.*, 2010). This method presents some issues for the reconstruction of past fire history. Firstly, low to moderate severity fires result in minimal alteration to infiltration and therefore, runoff is insufficient for sediment entrainment. Therefore, rates of erosion remain relatively unaltered so low to moderate severity fires cannot be determined from analysis of the hydrograph alone (Prosser, 1987). Furthermore, this method relies on the occurrence of a storm or significant rainfall event prior to adequate revegetation for improved channel stability. This is not always the case in practice and is highly subjective to the climatic conditions of the site. The surveying methods used by Eaton *et al* (2010), are contingent on yearly assessments of the site for comparison with the hydrograph which may prevent detection of smaller changes to the channel between surveys. Additionally, to accurately determine the impact of the fire event, surveying is required for a minimum of five years post-fire. Therefore, these methods of surveying and analysis of the hydrograph are best suited to providing a preliminary understanding of the site, however, to reconstruct a fire record of a range of fire severities, these methods are deficient.

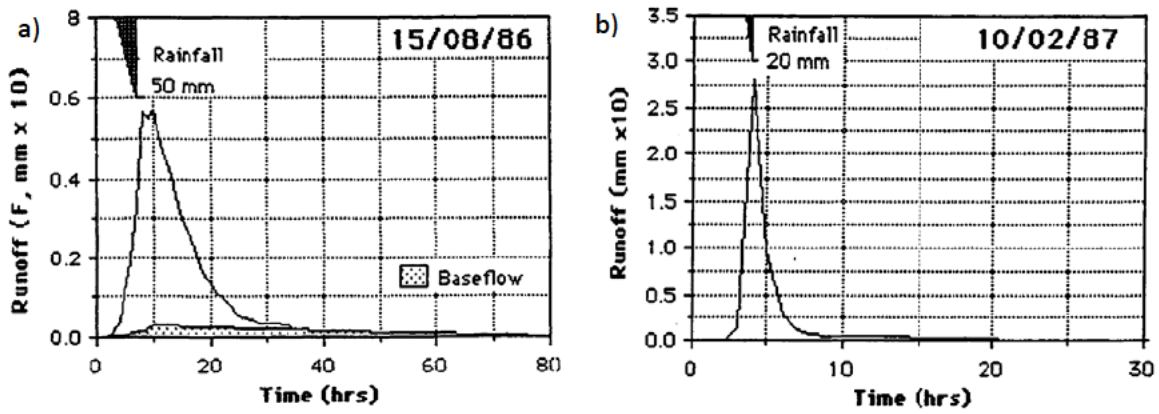

Figure 2.2 a) A typical hydrograph for Limekiln Creek, NSW and b) the hydrograph following the first major rainfall event, 8 days post-fire. There is a significant increase in runoff post-fire contrast to the typical runoff, despite less rainfall (Prosser, 1987).

Debris and hyper-concentrated flows can emanate as a result of a high severity fire event followed by a large intensity storm or rainfall event and the stratigraphic layers they establish can be analysed to determine a fire history (Pierce, Meyer and Jull, 2004; Bigio, Swetnam and Pearthree, 2017). Extreme discharges may result following increased rainfall events and can entrain sediment in the form of debris flows through rilling, gullying and slope wash processes. Following a fire event, these debris flows can present in the sedimentary record as a thick, boulder-dominated layer that is charcoal rich

(Pierce, Meyer and Jull, 2004). These layers may be further distinguished by the matrix colour and presence of burned soil or sediment layers, such as in the form of fire reddened layers. Charcoal is most commonly found in the fine-grained matrix of both debris flows and hyper-concentrated flows and is typically concentrated in layers of burned soil surfaces, dominated by charred wood, twigs and, in some cases, a white ash layer (Bigio, Swetnam and Pearthree, 2017). Analysis of these layers can be used to determine the percentage of charcoal to estimate the severity of the fire. Fragments of coarse angular charcoal are interpreted as representing "large fire events" (Pierce, Meyer and Jull, 2004). Samples may also be classified based on the certainty of which they are "fire-related" where matrix colour and position in relation to burnt soil surfaces is taken into account in conjunction with angular charcoal presence (Bigio, Swetnam and Pearthree, 2017). Similar to the analysis of the hydrograph, this method relies on the occurrence of significant rainfall prior to revegetation after a high fire severity event in order for sufficient sediment flow to initiate a debris or hyper-concentrated flow. The occurrence of these layers in the stratigraphic record is also highly subjective and site-specific. Whilst in some locations, a thick layer is deposited signifying the occurrence of the debris flow, other sites may only display a thin, marginal facies that is difficult to distinguish against the adjacent layers of the stratigraphic profile (Pierce, Meyer and Jull, 2004). Large basin areas tend to experience more dilute flows due to insufficient entrainment of sediment and the charcoal may remain suspended such that no charcoal is present in fire-related hyper-concentrated and streamflow layers post-fire (Meyer *et al.*, 1992). Therefore, this method also limits the fire record to high severity fires and is highly subjective in its success to both site and climatic conditions.

Analysis of the size and shape of charcoal can allow for the determination of whether a fire has occurred *in situ* or in the surrounding catchment area (Jull and Geertsema, 2006; Kennedy, Tech and Horn, 2008; Bordy *et al.*, 2018). Charcoal forms as a result of incomplete combustion of organic material (Lynch *et al.*, 2007; Stivrins *et al.*, 2019) and can occur in three main size fractions: fine particulate material or soot, microcharcoal, and macrocharcoal (Lynch *et al.*, 2007). Fine particulate charcoal can be transported by wind and may, therefore, originate from outside the catchment of interest, microcharcoals are typically from fires that arise within the catchment but did not directly impact the site itself and macrocharcoals represent an *in situ* fire since they are least likely to be transported (Lynch *et al.*, 2007; Kennedy, Tech and Horn, 2008). The shape of charcoal can be used to confirm or contrast hypotheses on the origin of the fire. Fragile, angular charcoal typically identifies with *in situ* fires since reworking has not occurred from transport and traction (Bordy *et al.*, 2018). There are several key issues with this method. Firstly, there are a number of assumptions made in terms of distinguishing the origin of a fire and various aspects, such as roundness and fragility, are subject to individual interpretation. Fine charcoal fragments are poorly preserved in the stratigraphic

record and are easily transported through wind and flood events. In instances of preservation, layers of fine charcoal can be difficult to identify against adjacent layers in the sediment profile (Nelson, 2010). Finally, whilst this method can be applied for the estimation of the origin of a fire, it cannot be used to determine whether the fire is the result of anthropogenic or natural processes (Black, Mooney and Haberle, 2007) nor to distinguish severity.

Radiocarbon dating of charcoal is the most common method of determining a chronology of fire events in an alluvial setting. Charcoal samples representative of fire-affected sedimentary layers are typically pre-treated in preparation for accelerator mass spectrometry (AMS) ^{14}C dating (Gillespie *et al.*, 1992; Nelson, 2010). The chronology formed from the radiocarbon ages of the samples has been calibrated against other dating techniques, such as optically stimulated luminescence (OSL) or tree ring reconstructions (Nelson, 2010). A variety of predicaments arise when using this method for the reconstruction of a fire record for a given site. Firstly, contamination can often occur due to the ease of transport of charcoal. The fragments dated may not be primary, instead, originating from a past fire event, having been mobilised during an erosion event, soil creep or mass flow from a flood (Gillespie *et al.*, 1992; Bordy *et al.*, 2018). For this reason, radiocarbon dating of macrofossils, such as seeds, needles or twigs is preferable to limit dating of a younger event (Pierce, Meyer and Jull, 2004). Multiple tests may be run per charcoal layer and averaged as one possible mechanism to increase consistency between the results (Jull and Geertsema, 2006). During pre-treatment of the charcoal fragments, there may be limited to no recovery of the graphite fraction for analysis due to significant contributions of clay or disintegration of the charcoal. This can introduce some complications in layers that are more clay-rich (Jull and Geertsema, 2006). As with many of the previous methods outlined, radiocarbon dating also does not distinguish fire severity, only occurrence. Calibrating the chronology determined against OSL and tree-ring reconstructions introduces additional issues. Tree ring reconstructions limit the chronology to the life of the tree and assume that the tree survives the fire event. In severe fire events, trees may not be preserved and therefore, a record of fire scars may not be maintained for calibration (Stivrins *et al.*, 2019). OSL uses a correction for quartz through preheating at 110°C to allow for comparable sensitivities between samples. Fires can reach temperatures >400°C (Guo and Bustin, 1998), causing an increase in the sensitivity of the sample and resulting in possible systematic errors which could result in an underestimation of the age (Singhvi *et al.*, 2011). Hence, there is an absence in verified, long-term proxies for the determination of past fire occurrence and their severity that will be explored using isotopic and spectroscopic alternatives in this study.

2.3 Boron Isotopes

Boron exists in the natural environment almost exclusively bonded to oxygen, forming either a hydrosoluble tetrahedral (tetrahydroxyborate [$B(OH)_4^-$]) or trigonal (trihydroxy boric acid [H_3BO_3]) complex and has two stable isotopes- ^{10}B and ^{11}B which experience preferential enrichment in each of these forms respectively (Lemarchand, Schott and Gaillardet, 2005; Sun *et al.*, 2019). ^{10}B and ^{11}B experience a relative abundance in nature of 20% and 80% respectively (Lemarchand, Schott and Gaillardet, 2005). The trigonal and tetrahedral complexes form an equilibrium (Equation (1)) that is highly pH-dependent. In the case of soils, however, it has been found that the tetrahedral species is most prevalent irrespective of the pH (Gonfiantini and Pennisi, 2006).

$$B(OH)_3 + OH^- \leftrightarrow B(OH)_4^- \quad (1)$$

Due to high geochemical reactivity and large mass discrepancies between the two isotopes (Xiao *et al.*, 2013), boron experiences significant isotopic fractionation in the natural environment (Lemarchand *et al.*, 2012; Xiao *et al.*, 2013; Ercolani, Lemarchand and Dosseto, 2019), a property that has shown to be advantageous for determining weathering reactions (Romer and Meixner, 2014; Ercolani, Lemarchand and Dosseto, 2019). The isotope ratio is generally expressed as $\delta^{11}B$, which is written as follows:

$$\delta^{11}B = \left(\frac{^{11}B/^{10}B_{\text{sample}}}{^{11}B/^{10}B_{\text{reference}}} - 1 \right) \times 10^3 \quad (2)$$

Rivers and biomass are typically enriched in ^{11}B, whilst depletion (or enrichment in ^{10}B) is typical of clay minerals and the organic and inorganic surface (Peltola and Åström, 2006). The most significant fractionation of boron occurs during the neoformation of secondary phases in which newly formed solids become enriched in the lighter isotope, leaving a heavier residual solution (Ercolani, Lemarchand and Dosseto, 2019). Adsorption of boron onto clay minerals is considered to be a two-step process. Initially, boron is adsorbed onto the mineral surface forming a coating through ligand exchange, replacing hydroxyl groups (Goldberg, 1997). Over time and with increasing burial, boron migrates and undergoes substitution with silicon and aluminium in the tetrahedral crystal lattice of the clay structure (Goldberg, 1997; Williams *et al.*, 2001). Due to this enrichment of boron in silicate mineral phases contrast to carbonates, it can be used to trace silicate phase changes (Schmitt *et al.*, 2012).

The biogeochemical cycle of boron is dominated largely by the biosphere. Boron is an essential micronutrient for plants, contributing to cell wall construction and nitrogen fixation (Cividini *et al.*, 2010). Nutrients typically accumulate in the topsoil as a result of throughfall and litter decomposition, experiencing a depletion as a result of active absorption by plant roots (Figure 2.3) (Gaillardet and

Lemarchand, 2009; Cividini *et al.*, 2010). During this absorption process, there is a slight preference for ^{10}B, resulting in a small enrichment of ^{11}B in soil solution (Cividini *et al.*, 2010). Once boron is uptaken by various plants, boron isotope fractionation in the plant depends on factors such as the species of plant as well as the section of the plant analysed, for example, the xylem sap experiences an enrichment in ^{10}B, whilst the leaves are enriched in ^{11}B, causing a lower and higher $\delta^{11}B$ value respectively (Figure 2.4) (Marentes, Vanderpool and Shelp, 1997).

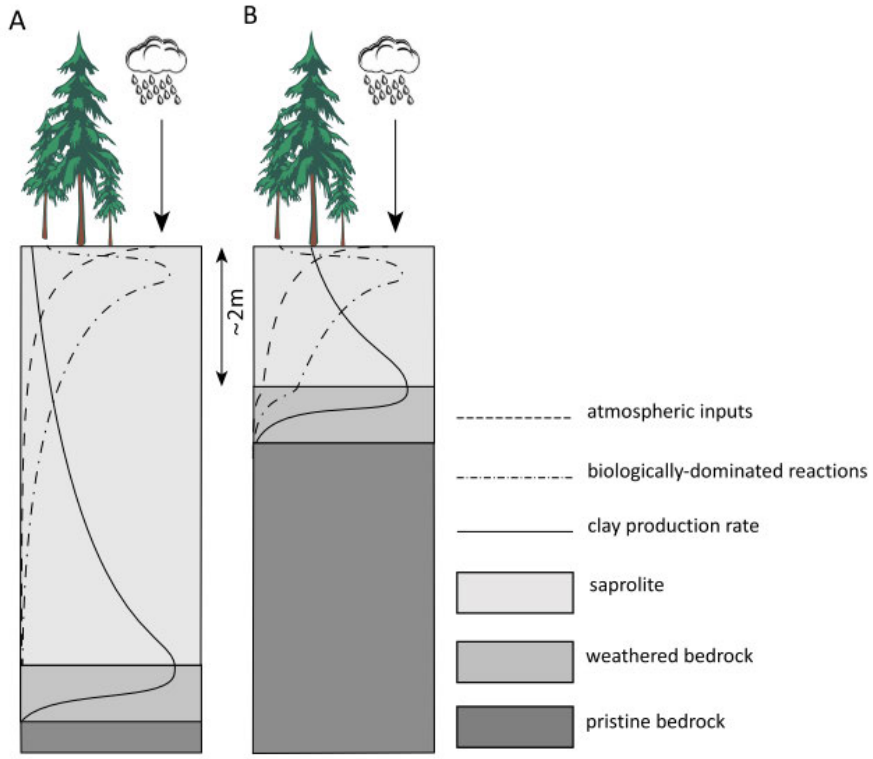

Figure 2.3 Schematic of the potential parameters controlling the B isotope composition of the clay fraction of both soils and the dissolved load. Atmospheric input and biological recycling decline with depth. A) highlights a thick weathering profile, less influenced by atmospheric inputs and biological recycling, a contrast to B) demonstrating a thinner weathering profile in which atmospheric inputs and biological processes dominate (Ercolani, Lemarchand and Dosseto, 2019).

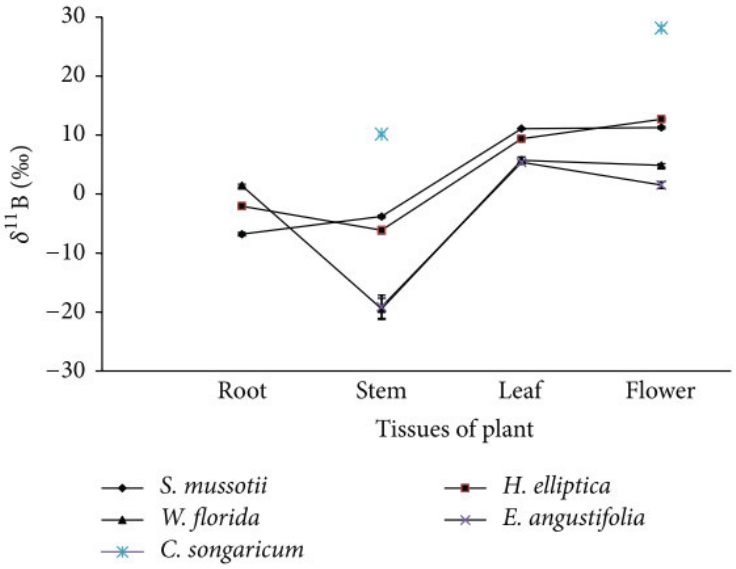

Figure 2.4 The changes in $\delta^{11}B$ for various plant components for 5 plant species (Xu *et al.*, 2015)

Drought, coupled with elevated temperatures can strengthen fixation of boron in the clay phase, limiting the amount of available B in the soil for uptake and increased generation of insoluble B-containing compounds (Sun *et al.*, 2019). Contributions from the atmosphere, such as through evaporation from seawater, biomass burning or dissolution of atmospheric dust, in conjunction with river export and chemical input are relatively negligible contrast to the continuous input from the biological sphere (Gaillardet and Lemarchand, 2009). This is particularly evident in tropical climates in which biological fluxes of boron are significantly greater than temperate climates (Figure 2.5) (Gaillardet and Lemarchand, 2009).

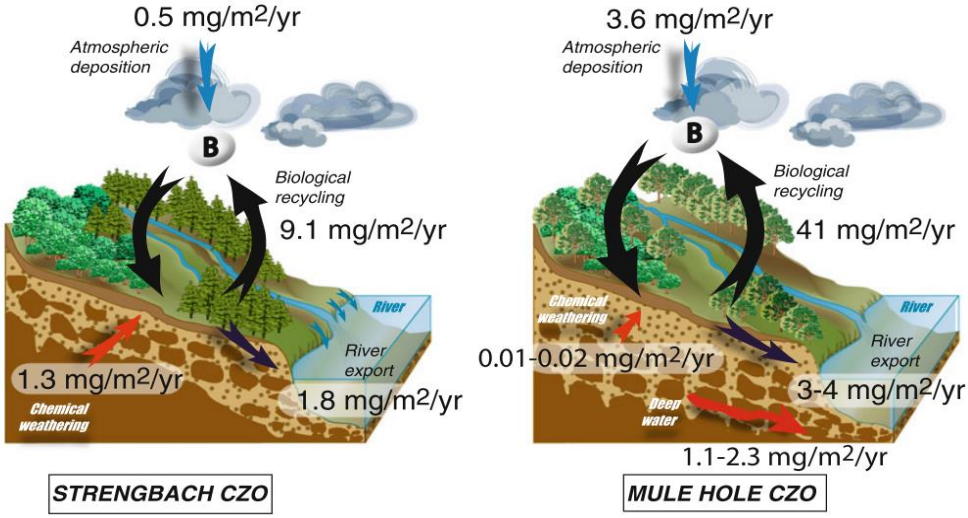

Figure 2.5 Fluxes of boron in the critical zone of both tropical (Mule Hole) and temperate (Strengbach) climates. Both climates highlight the significant effects of biological recycling in contrast to other fluxes of boron (Gaillardet and Lemarchand, 2009)

In recent decades, there have been a variety of methods used to extract boron for analysis with varying degrees of success, utility and reproducibility. Early methods weighed samples with approximately 10 µg of boron into nickel crucibles in conjunction with 6-10 times the amount of sodium hydroxide as flux. The samples were then heated until fusion was achieved, then samples were placed in an ice bath and transferred to a distillation flask. The solution was acidified with hydrochloric acid and volatilised in the presence of methyl alcohol, using a condenser. The volatilised solution was captured in the sodium hydroxide solution for colourimetric analysis (Shima, 1963). Methods were later altered to separate boron isotopes from silicate minerals using potassium carbonate fusion and boron-specific resin. This allowed for the determination of the sum of non-desorbed or fixed boron from clay samples (Vengosh *et al.*, 1991). Similarly, more recent methods have employed the use of the boron-specific resin- Amberlite, for the separation of boron from the clay matrix (Lemarchand *et al.*, 2002; Chetelat *et al.*, 2009). For the extraction of boron from water samples, the most common technique is the use of columns containing the Amberlite resin followed by a pH adjustment before conducting a microsublimation process in order to remove organic interference from the clay signal (Lemarchand *et al.*, 2002; Chetelat *et al.*, 2009). Solid samples were processed using alkali fusion, heating the samples with a fluxing agent in platinum crucibles at 950°C for 15 minutes. The resulting fusion glass was then dissolved with the aid of boiling water (Chetelat *et al.*, 2009). Plant samples typically follow a similar protocol to water samples with the addition of microwave digestion prior to cationic exchange chromatography and microsublimation (Roux *et al.*, 2014). Much of the geochemical cycle of boron remains unknown or poorly understood due to various difficulties in the acquisition of reliable boron isotope data (Roux *et al.*, 2014). Boron extraction methods used in this project will incorporate the use of alkali fusion with potassium carbonate, cation exchange chromatography and boron-specific chromatography.

A number of analytical techniques have been employed for the determination of boron isotope ratios in various sample types. Colourimetric analysis works on the basis that certain reagents, such as azomethine-H, methylene blue, curcumin and crystal violet, form colour complexes in the presence of boron. The major downfalls of this method are the requirement for often hazardous reagents, limiting utility, as well as the difficulty in distinguishing between ^{10}B and ^{11}B concentrations in the sample (Sah and Brown, 1997). The use of potentiometric methods has also been employed. For this method, boron is extracted from the sample matrix and treated using hydrofluoric acid (HF) to form a tetrafluoroborate ion. The resulting solution can then be analysed by potentiometric titration with a BF^- electrode. The key weakness of this method is the major utility issues through the use of HF as well as the interference of the sample matrix in the results (Sah and Brown, 1997). The most common methods now used for solutions are thermal ionisation mass spectrometry (TIMS) or multicollector

inductively coupled plasma mass spectrometry (MC-ICP-MS) (Xiao *et al.*, 2013). TIMS can be separated into positive thermal ionisation mass spectrometry (P-TIMS) and negative thermal ionisation mass spectrometry (N-TIMS). For P-TIMS, the boron in each sample is transformed into a positively charged ion and exists in the form of either an alkali or metal metaborate cation. In contrast, the process for N-TIMS involves the transformation to metaborate anions (Xiao *et al.*, 2013). Both TIMS methods carry a high level of accuracy and precision (Sah and Brown, 1997). N-TIMS does not require the input of alkali or metal salts and maintains a higher ionisation efficiency that allows for the detection of smaller quantities of boron (Xiao *et al.*, 2013). The major disadvantage of both TIMS methods is the isotopic fractionation that occurs throughout the analysis, with a progressive enrichment favouring the ^{11}B isotope as well as the extensive and time-consuming sample preparation required prior to analysing samples (Xiao *et al.*, 2013). Isobaric interference may also arise due to incorrect or incomplete purification of the boron prior to analysis (Sun *et al.*, 2019). In MC-ICP-MS, samples are in the form of an aqueous liquid and are introduced into the plasma through a nebuliser and spray chamber (Sah and Brown, 1997; Xiao *et al.*, 2013). The number of electrons and positive ions in the plasma are approximately equal, resulting in no charge (Sah and Brown, 1997). The peak intensities at masses 10 and 11 are then determined for the calculation of $\delta^{11}B$. Recent advances in this technique have allowed for greater precision than TIMS (Roux *et al.*, 2014) and requires less rigorous purification of boron samples. In addition, there is no interference at the masses for both of the stable isotopes and little suppression of boron ionisation (Xiao *et al.*, 2013) making a strong case for its use.

Boron isotope analysis as a method of determining past fire occurrence is currently a new and unexplored technique, with only one study to date exploring the changes in boron isotope ratios in sedimentary records as a proxy for fire (Peltola and Åström, 2006). When exposed to increases in temperature, boron is leached from rocks and organic matter (Kharaka and Hanor, 2003), therefore, boron isotopes analysis utilises plant-mineral interactions for the detection of signatures created as a result of altered vegetation cover (Lemarchand *et al.*, 2012). Analysis of stable boron isotopes in lake sediments collected in Finland and analysis using ICP-MS following aqua regia digestion produced encouraging results. A peak at approximately 40cm depth was observed for elemental boron concentrations and was accompanied by a decrease in $\delta^{11}B$ value. It was noted that this decrease in $\delta^{11}B$ value was associated with a small shift towards the lighter isotope (Figure 2.6). The authors suggest that this decrease was the result of leaching of wood ash following the burning of a predominantly wooden town in the early 19th century. The addition of ash leachates resulted in an elevated pH, causing increased tetrahedral coordination and adsorption of ^{10}B in the clay matrix, reducing the amount of available boron for plant uptake (Peltola and Åström, 2006). Through analysis of boron isotope concentrations and resulting plant-mineral interactions, it is also possible to

determine a record of changes in vegetation cover for a given area (Lemarchand *et al.*, 2012), which can also be advantageous in the context of analysing fire occurrence. Since high severity fires remove the canopy of vegetation (Certini, 2005), it is expected that there would be an altered $\delta^{11}B$ value as a result of both the addition of ash increasing pH and clay adsorption, as well as changed rates of plant uptake of boron from the soil solution. Analysis of the clay fraction should yield decreased $\delta^{11}B$ values for fire effected layers of the sedimentary record that can act as a sensitive proxy to trace the severity and intensity of bushfires.

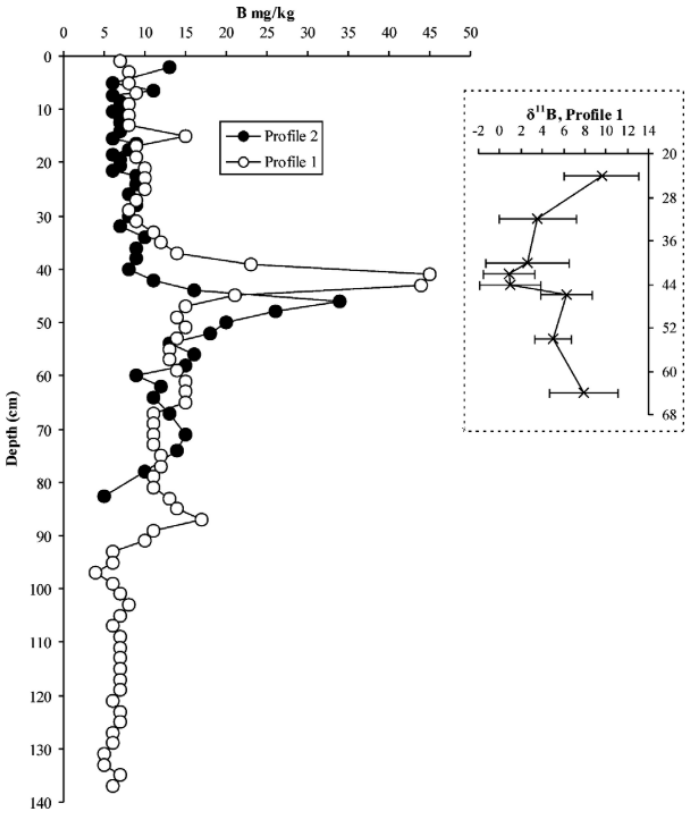

Figure 2.6 The concentration of boron in two profiles as well as the $\delta^{11}B$ values for the first profile taken from Permoflada Lake in Finland (Peltola and Åström, 2006)

2.4 Fourier Transform Infrared Spectroscopy (FTIR)

Infrared spectroscopy techniques operate on the basis of the unique vibrations emitted by molecular bonds and have been recognised as a robust method for the determination of charcoal in soils as well as the pyrolysis temperatures of charcoal (Cadd *et al.*, 2020). Bands within the spectra can be attributed to changes in components of soil to determine the effects of factors such as temperature and heating duration on chemical bonds (Figure 2.7). Fire may also result in the formation of new substances with high oxidation resistance, resulting in the formation of new peaks and bands in the spectra (Abakumov, Maksimova and Tsibart, 2018).

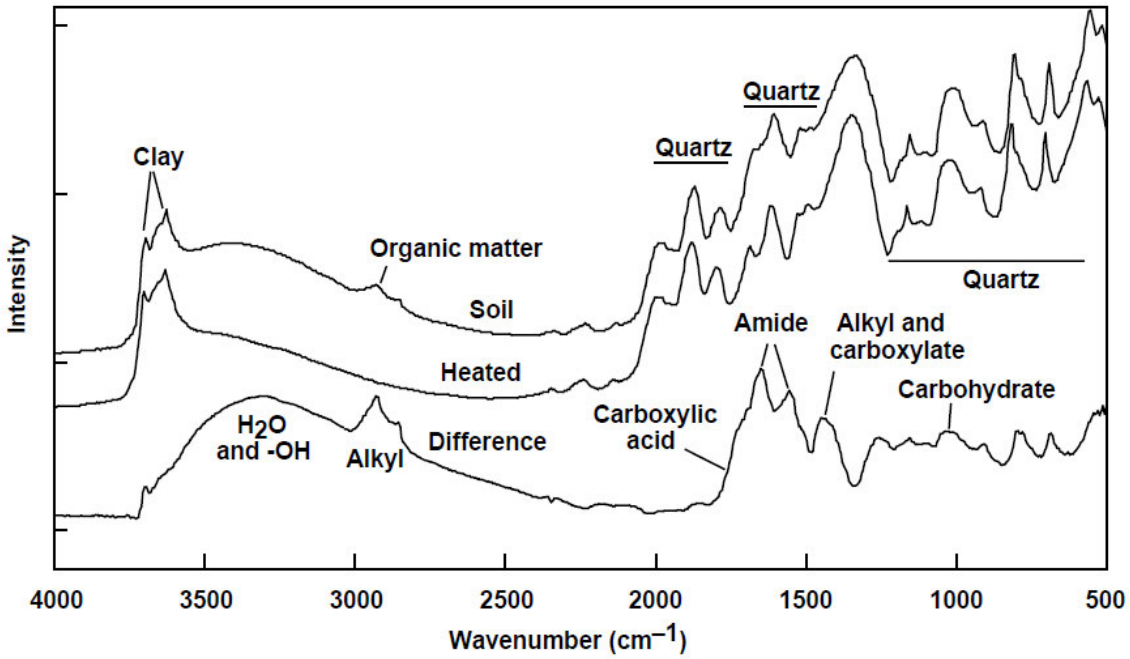

Figure 2.7 The mid-FTIR DRIFT spectrum formulated for soil samples before and after heating at 350°C, highlighting major mineral and organic species as well as the material lost from heating (shown through the "difference" spectrum) (Skjemstad, Janik and Taylor, 1998)

Previous methods have manufactured artificial charcoal at various temperatures under laboratory conditions to determine molecular changes under a range of heating conditions, thus correlating to different fire severities, using FTIR analysis (Guo and Bustin, 1998; Gosling, Cornelissen and McMichael, 2019). Reference samples were prepared using three different pretreatment methods: untreated, water and hydrogen peroxide. These samples then underwent heating at temperatures between 200 and 680°C to emulate the temperatures reached during a typical bushfire. FTIR was conducted on both reference and field samples to estimate the severity of the fire on the basis of the changes to the molecular composition (Gosling, Cornelissen and McMichael, 2019). There was a noticeable difference between spectra for charcoal generated at low (<400°C) compared with high temperatures (500-700°C) (Figure 2.8) (Gosling, Cornelissen and McMichael, 2019). Alternatively, charcoal reference samples have been manufactured by covering fungal and wood fragments beneath a thin layer of sand before heating to various temperatures between 200 and 600°C to correspond with the release of carbon monoxide and methane as well as the most common temperatures of bushfires recorded in the existing literature (Guo and Bustin, 1998). Similarly, the FTIR spectra produced for the reference charcoal samples were compared to inertinite and field-collected samples to estimate the changes in molecular composition following heating (Guo and Bustin, 1998). Analysis of laboratory-generated charcoal for comparison to field samples has proven advantageous in comparison to previous alluvial methods for determining past fire occurrence in that it allows for the determination of fire severity as either low or high (Gosling, Cornelissen and McMichael, 2019).

Through this, it is possible to reconstruct a fire record for various sites to determine not only fire occurrence but the frequency of high severity fires and the rate of change over time. Ratios of the functional groups can also be used to determine the degree of aromatisation, a characteristic also linked to the temperature and heating duration of the fire (Guo and Bustin, 1998). This can also be used to infer the vegetation types present as well as the influence of both anthropogenic and natural fire activities (Gosling, Cornelissen and McMichael, 2019). Understanding dominant vegetation communities is important for fire management purposes as some species burn at higher temperatures than others as well as determining how the landscape will respond and regenerate post-fire (Guo and Bustin, 1998). However, these studies analyse only the charcoal fraction which can be easily mobilised by wind or water and can be difficult to identify with the human eye. This method neglects the effects of fire and heating on the matrix of the sediment and soil samples collected.

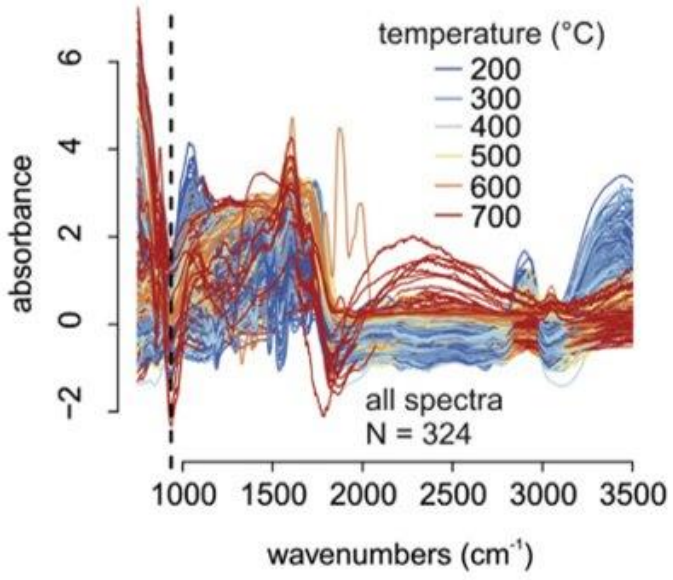

Figure 2.8 The FTIR absorbance spectra for reference charcoals produced at different temperatures between 200 and 700°C with noticeable variations between low- and high-temperature charcoals. This is particularly the case in the band at 2500 and 3500cm^{-1} where high temperatures experience an increase in peak and decrease in peak respectively contrast to low-temperature charcoals (Gosling, Cornelissen and McMichael, 2019).

Soil organic matter is the most responsive component to fire, with incomplete combustion resulting in significant biological and chemical transformations occurring post-fire that can be detected in the FTIR spectrum (Mastrolonardo *et al.*, 2014). Surface fires can generate heat transfer into the soil, resulting in a number of combustion-related processes, such as dehydration, dealkylation and decarboxylation. For charcoal that experiences dehydration, dealkylation or decarboxylation, there is a significant reduction to complete loss of peak at 3290cm^{-1}, 2920-2859cm^{-1} and 1732cm^{-1} respectively (Figure 2.9) (Mastrolonardo *et al.*, 2014). A carbonised environment may also arise as a result of combustion. This can significantly alter the chemical composition of the soil organic matter (Chen *et al.*, 2012), resulting in increased vibrational stretching and selective degradation of aliphatic

structures, linked to increases in soil water repellency (Simkovic *et al.*, 2008). Investigation of the changes to soil water repellency is typically through the simulation of heating conditions on either side of the threshold for soil hydrophobicity destruction (Simkovic *et al.*, 2008) as well as carbonising conditions in the laboratory (Chen *et al.*, 2012). Soil hydrophobicity was determined using a water drop penetration test in which droplets were placed on the surface of the sample in a petri dish and the time was recorded at the time of complete penetration. The FTIR spectra were then consulted to determine the functional groups causing destruction of water repellency within soil samples (Simkovic *et al.*, 2008). It was found that the region of the spectra responsible for the changes in soil water repellency was largely in the band of 3020-2800cm^{-1} which relates to the aliphatic stretching of both methyl and methylene groups (Simkovic *et al.*, 2008). To simulate carbonisation, samples were placed in a sealed chamber and heated at temperatures as reported in the literature. The FTIR results may also be compared to nuclear magnetic resonance (NMR) results to assist in determination of the molecular structure, and the change following heating (Chen *et al.*, 2012). Through this simulation, it was found that whilst many of the characteristic absorption peaks were removed following heating at temperatures >400°C, a broad absorption band remained at wavenumbers 1200-900cm^{-1}, associated with the presence of temperature resistant silicate minerals such as quartz (Chen *et al.*, 2012). There have, however, been inconsistencies and significant variations in the interpretations of the stretching and vibrational effects on bonds, likely due to or enhanced by the overlap of bands on the spectra (Simkovic *et al.*, 2008).

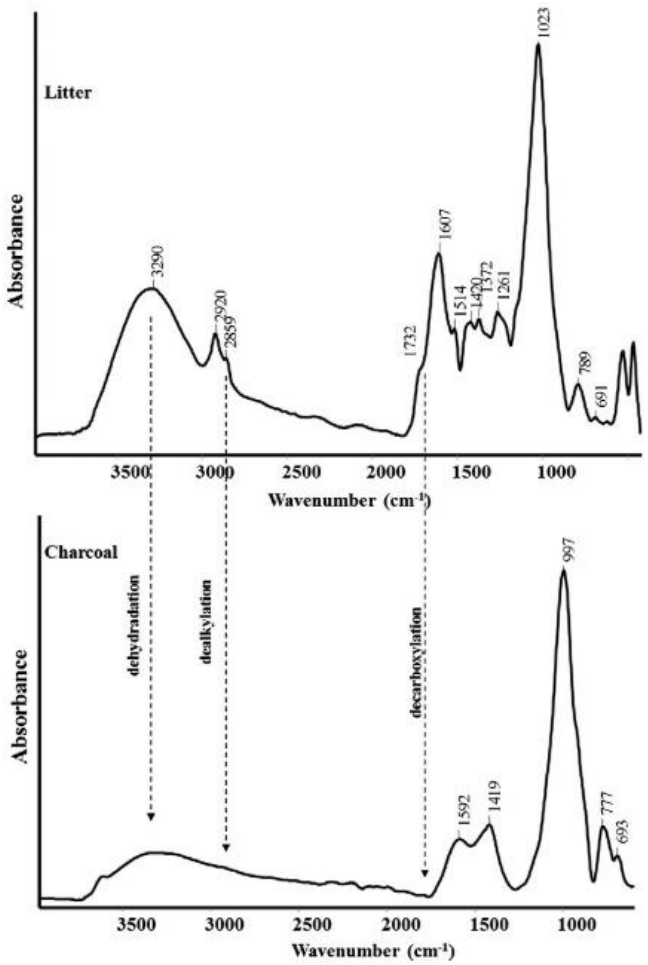

Figure 2.9 The ATR/FTIR spectra produced for both leaf litter and charcoal with the wavenumbers affected by key combustion processes identified by the dotted arrows. (Mastrolonardo *et al.*, 2014)

With increasing temperatures, the chemical composition of lignin, complex carbohydrates and sugars of leaf litter undergo several transformations that can be detected in distinct bands of the FTIR spectra (Lammers, Arbuckle-Keil and Dighton, 2009; Merino *et al.*, 2015). This is due to varying thermal stability between biopolymers, thus affecting the composition of various plant species and therefore, the response of functional groups to heating. For example, hemicellulose and cellulose have lower thermal stability when compared with lignin (Merino *et al.*, 2015). One method of analysis to test this change is the collection of leaves from various plant species which are sieved to ensure size consistency, followed by the simulation of a fire event of different temperatures in a muffle furnace (Lammers, Arbuckle-Keil and Dighton, 2009). Alternatively, soil samples containing burnt leaf litter have been collected directly after a fire event and prior to disturbance by rainfall. Visual assessment was used to determine the soil burn severity at the site by soil colour, litter consumption and degree of ash deposition parameters (Merino *et al.*, 2015). In both cases, analysis was then undertaken using FTIR spectroscopy to determine the changes in absorbance corresponding to different functional groups as well as between plant species (Figure 2.10) (Merino *et al.*, 2015). It was noted that the

changes to the FTIR spectra between plant species were largely the result of contributions from the transformation products of lignin and cellulose, affecting absorbance at bands at 1600cm^{-1} and 1375cm^{-1}. The five plant species analysed showed significant variation and no common trend could be determined, suggesting that chemical degradation of lignin is highly species-specific (Merino *et al.*, 2015). Combustion of plant material richer in nitrogen typically results in the formation of charred material that is largely composed of non-aromatic (or aliphatic) components which are relatively resistant to elevated temperatures. An increase in the bands around 1600-1400cm^{-1} reflects enrichment in nitrogen-containing compounds (Merino *et al.*, 2015). This method is advantageous for determining the approximate temperature of the fire since carbohydrates are transformed at approximately 250°C. Furthermore, it allows for the determination of the plant species being burnt as its composition determines the degree to which char is formed (Merino *et al.*, 2015). However, since this approach has only been applied on samples retrieved directly after a fire event or that have been manufactured in the laboratory, it is difficult to determine whether the response will be the same for sediment samples from a fire some years in the past.

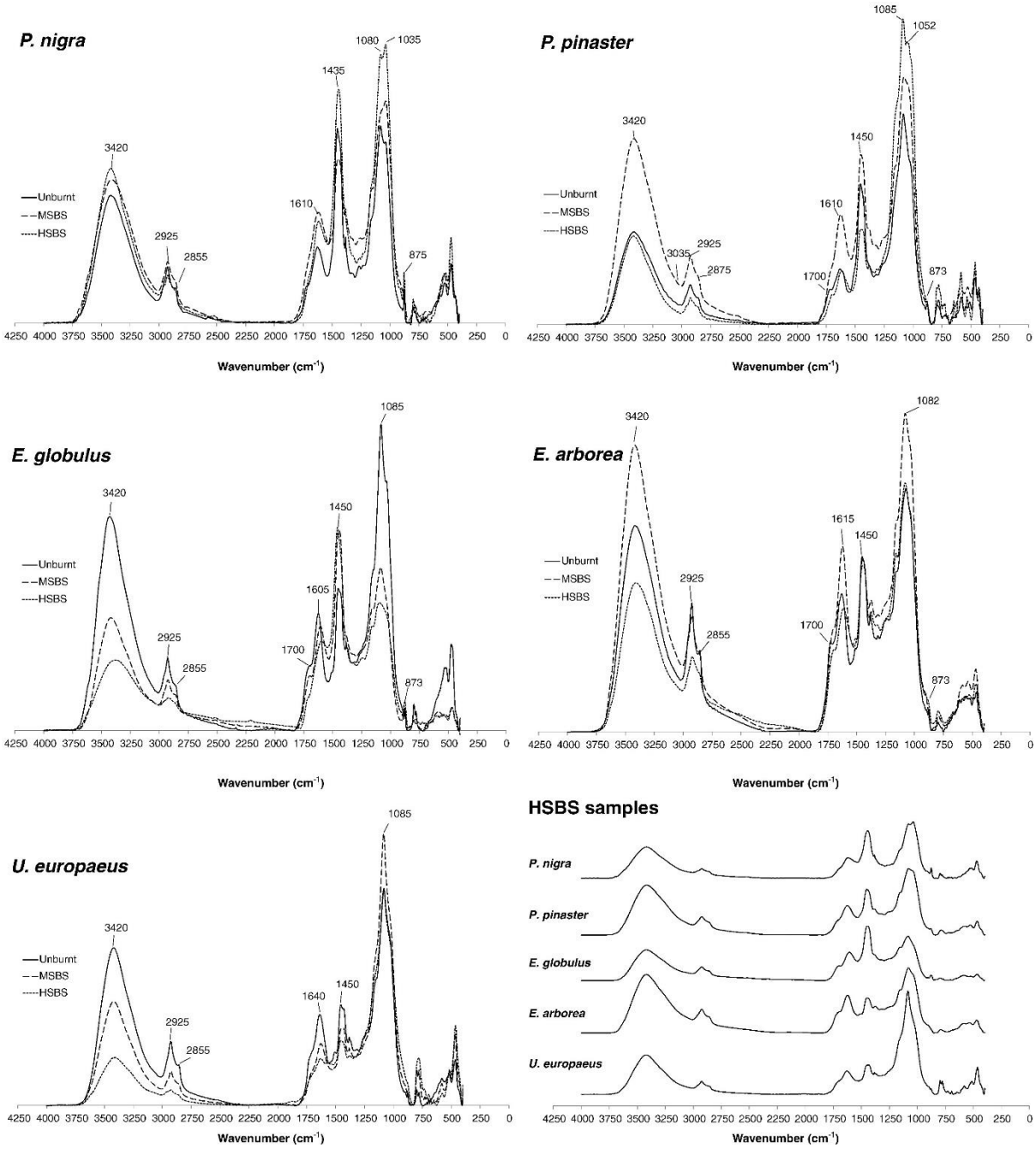

Figure 2.10 FTIR spectra for various plant species under differing burn severities: unburnt, moderate soil burn severity (MSBS) and high soil burn severity (HSBS). There is a noticeable difference between plant species and burn severities with a number of peaks increasing when exposed to moderate burn severities and reducing under high severity. Of particular note, there appears to be a shift in the peak at 1620-1600cm^{-1} between species (Merino et al., 2015).

A naturally occurring fire event is not solely a complete combustion reaction, often occurring in conjunction with pyrolysis conditions as a result of incomplete oxidation processes from reduced oxygen availability (Mastrolonardo *et al.*, 2014). Pyrolysis is an endothermic thermal decomposition process that can occur without the need for an oxidiser. Low density, thermal conductivity and density in conjunction with high specific heat cause wood fragments to undergo three stages of pyrolysis based on temperature (Bartlett, Hadden and Bisby, 2019). Doelsch *et al* (2009), analysed organic

matter under anaerobic and aerobic conditions for various time periods. With increased incubation, more significant chemical changes were observed under anaerobic conditions, particularly at 3300cm^{-1}, attributed to the elongation of carboxyl or alcohol bonds. This decrease in peak is also characteristic of increased dehydration (Doelsch *et al.*, 2009). Whilst this was not directly applied to fire-related samples, similarities can be drawn to samples that experienced pyrolysis, an incomplete combustion process occurring largely in a nitrogen atmosphere (Mastrolonardo *et al.*, 2014). A noticeable loss in peak as a result of degradation of the polysaccharide bond under anaerobic conditions was observed (Figure 2.11) (Doelsch *et al.*, 2009). There is a perceptible difference between char produced under forest fire versus pyrolysis conditions, with higher amounts of aromatics present following a forest fire. Furthermore, pyrolytic chars have increased presence of oxygen-containing functional groups (Esfandbod *et al.*, 2017). This has implications not only for predicting past fire, in that it allows the determination of fire-effected layers through increased aromatics and decrease in peak related to polysaccharide degradation, but also for the detection of sorption of chars to heavy metals in the environment. The sorption process occurs as a result of increased polarity of the fragments produced under pyrolysis conditions, causing increased metal-binding functionality (Esfandbod *et al.*, 2017). Previous studies employing the use of FTIR for the determination of past fire do not analyse the effects of incomplete combustion or pyrolysis on the matrix of the samples collected and Doelsch *et al* (2009) did not conduct studies on post fire samples. Therefore, this highlights an area of study yet to be explored.

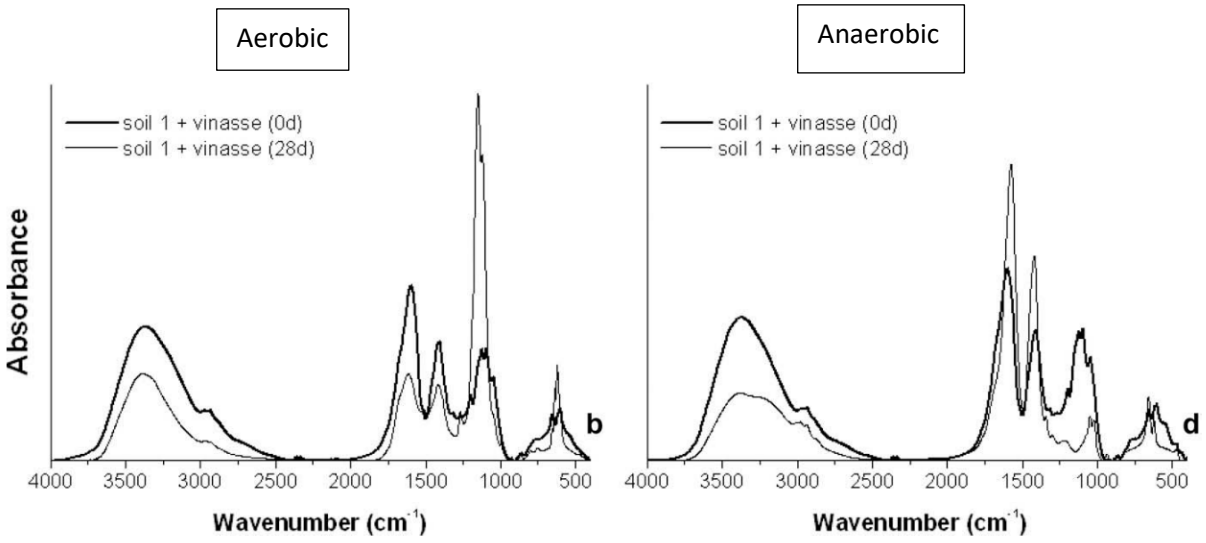

Figure 2.11 FTIR spectra of the soil + vinasse (20% waste from the fermentation industry) before and after 28 days of incubation under aerobic and anaerobic conditions. There is a noticeable reduction of the polysaccharide peak at 1200-1000 cm^{-1} under anaerobic incubation (Doelsch et al., 2009).

In summary, existing FTIR studies have focused efforts towards analysing molecular changes to charcoal and organic matter following fire events. Determination of temperature and severity has been achieved by comparison of field samples to laboratory-generated samples allowing for enhanced recognition of the aromatisation of the biopolymers when subject to heating and pyrolysis conditions. However, few studies have analysed changes to the matrix following fire, providing an opportunity for this study to bridge these gaps.

2.5 Conclusion

This project aims to test both boron isotopes and FTIR spectroscopy proxies against known fire occurrence to determine their viability. If successful, these methods have the potential to extend the existing fire record significantly and potentially bridge existing gaps in understanding of past fire regimes to assist with more accurate modelling of their response to changing climate.

3 Study Area

The Upper Nepean Catchment is situated approximately 20km west of Wollongong in New South Wales (NSW), Australia, covering approximately 25 134ha. It was designated as a state conservation area under the Sydney Catchment Authority (SCA) in February 2007 (Figure 3.1) (State of Management intent) and supplies high-quality raw drinking water to Greater Sydney, the Illawarra and Wollondilly Shires (Department of Environment and Heritage, 2017).

Figure 3.1 Regional context of the Upper Nepean Catchment (Office of Environment of Heritage, 2014)

3.1 Geology

The Upper Nepean catchment lies within the Sydney Basin - a major structural basin formed through crustal rifting during the early Permian. The basin was uplifted during the middle Triassic, forming dry land (Office of Environment of Heritage, 2014). Large braided rivers allowed transportation and deposition of quartz and Hawkesbury Sandstone from the northwest (Office of Environment of Heritage, 2014). The underlying geology is consistent with that of the Mittagong Formation, typified by interbedded shale and fine to medium-grained quartz (Gordon, 2017). Ashfield Shale extends below sea level in the watershed, separating the three primary river catchments- George's, Parramatta and Hawkesbury-Nepean; when weathered, a brightly coloured clay is produced (Haworth, 2003). Topography varies considerably, consisting of river gorges, exposed scarps and closed valleys, providing evidence for the occurrence of a number of geomorphological processes. The north-west to south-east axis diverts river flow away from the Illawarra Escarpment and incises gorges that allow for the supply of water to Greater Sydney (Department of Environment and Heritage, 2017).

3.2 Biodiversity and Petrology

Vegetation within the combined Hawkesbury-Nepean catchment is diverse, with 70% of the region dominated by native vegetation (Recher, Hutchings and Rosen, 1993). Plant species reflect changes in aspect, elevation, topography and edaphic conditions (Recher, Hutchings and Rosen, 1993), however, dry sclerophyll forest predominates (Gordon, 2017). The Upper Nepean Catchment also hosts seven ecological communities and a variety of threatened native plant and animal species (Department of Environment and Heritage, 2017).

Soil cover is largely derived from Hawkesbury sandstone origins, meaning that it is sandy and highly acidic (Department of Environment and Heritage, 2017), maintaining a pH between 4.5 and 6.5. The fertility of the soil is low and, when disturbed, it is easily eroded, raising concerns for water quality. The Upper Nepean Catchment area is a high bushfire hazard through both arson and lightning, which can cause disturbances, therefore, an appropriate fire management plan is required to ensure water quality is maintained (Office of Environment of Heritage, 2014).

3.3 Climate and the 2013 Bushfire

Temperate climate characterised by warm summers and no defined dry season predominate across much of the Sydney Basin (Black, Mooney and Haberle, 2007). Average annual rainfall is largely subject to altitude and distance from the coast (Black, Mooney and Haberle, 2007). The month of October 2013 saw bushfires devastate much of the coastal strip of New South Wales following the warmest September on record (Bureau of Meteorology, 2014). The Balmoral bushfire burned from the 17th-30th October 2013, during which time, it burnt approximately 12 136ha of dry sclerophyll forest (Doerr *et al.*, 2014). These fires were considered the worst since the 1960s in terms of losses; the spatial extent

and severity sparking water quality concerns (Doerr *et al.*, 2014). Heavy rainfall followed, resulting in flooding across much of the east coast at the end of March 2014 (Figure 3.2) (Bureau of Meteorology, 2015).

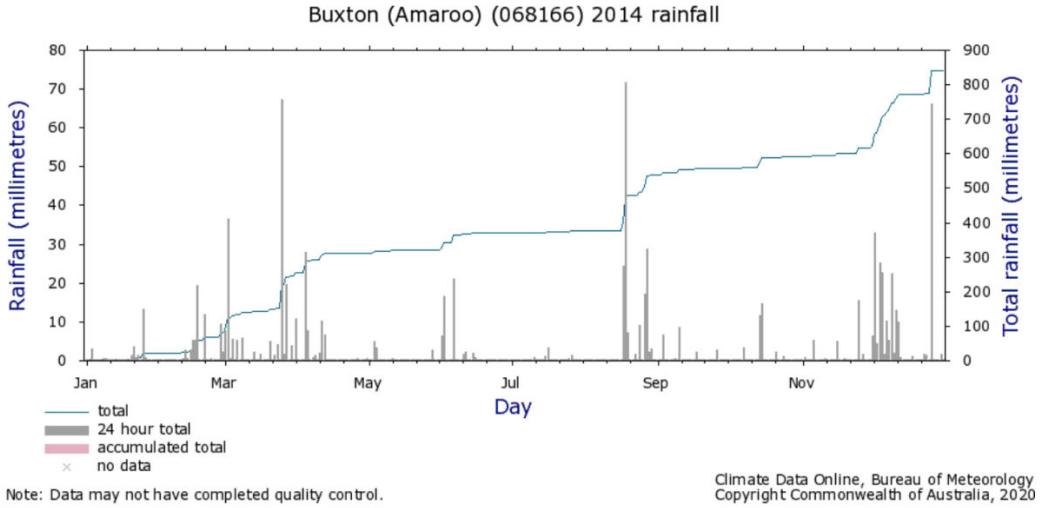

Figure 3.2 Rainfall for the 2014 year from the Buxton (Amaroo) reporting station, highlighting extensive rainfall (and potential for erosion events) on the 25th of March (67mm) and 18th August (71.4mm) (Bureau of Meteorology, no date).

3.4 Sample Sites

3.4.1 2017 Field Campaign

Two field campaigns have been undertaken in the Upper Nepean catchment that are discussed in this study. Preliminary results were determined from samples collected in 2017 from an unnamed tributary of Hornes Creek in the Yanderra Bargo region of NSW, henceforth referred to as Rebecca Creek (34°19'27 S, 150°33'58 E). It drained an area experiencing the highest severity fire in 2013 (Figure 3.3).

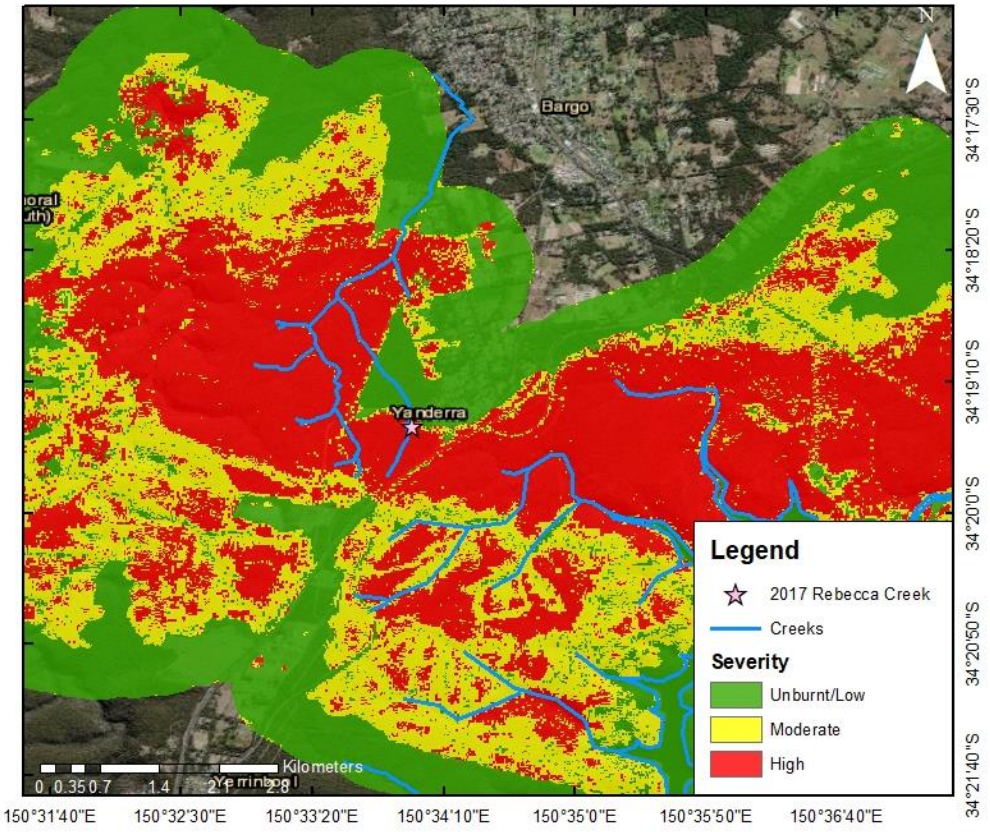

Figure 3.3 Study sites for the 2017 field campaign in relation to the fire severity map (adapted from NSW DPIE unpublished data).

Samples were collected at 5cm depth intervals, with additional collected where charcoal-rich layers occurred between these bands. Charcoal-rich layers were identified at 25-30cm and 37-40cm depth; after this point, bedrock was reached, and no additional samples were collected (Figure 3.4).

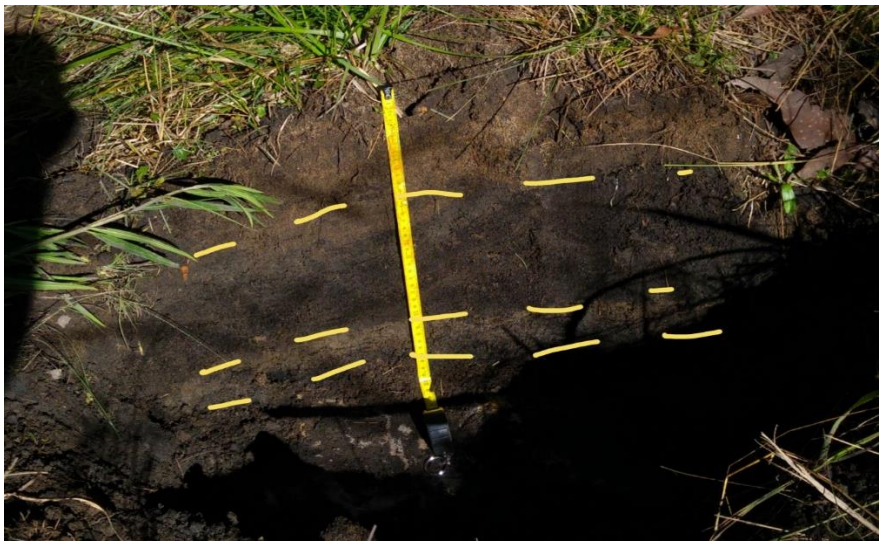

Figure 3.4 2017 Rebecca Creek pit with charcoal layers at 25-30cm and 37-40cm depth.

3.4.2 2020 Field Campaign

A second field campaign in the Upper Nepean Catchment was launched in March 2020. Four creeks were selected for analysis; Hornes Creek, Long Creek, Washhouse Gully and Rebecca Creek also located in the Yanderra Bargo Region of NSW (Figure 3.5). All four creeks sampled drained an area affected by the highest severity in 2013. The western side of the freeway was affected to some extent in the 2019-20 bushfires, however, did not directly affect the sites selected nor the area that they drain.

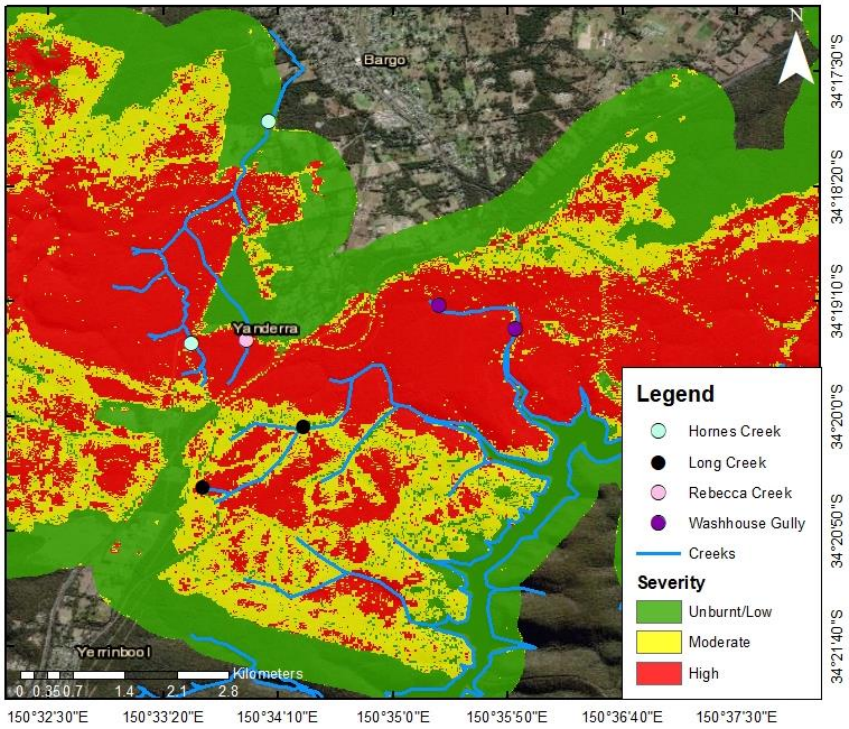

Figure 3.5 Fire Severity map following the 2013 bushfire highlighting study locations of Hornes Creek (aqua), Long Creek (black), Rebecca Creek (pink) and Washhouse Gully (Purple) respectively (adapted from NSW DPIE unpublished data).

Emphasis was placed on Washhouse Gully 1 Core 1 (34°19'22 S, 150°35'54 E) for comparison to the preliminary findings from the 2017 samples due to time constraints. The core was subsampled at 2cm depth intervals up to 32cm, beyond which point, large rock fragments prevented consistent subsampling and one sample was obtained for the remaining sediment between 32 and 43cm (Figure 3.6). A charcoal rich layer was identified at 24-32cm depth; however, charcoal fragments were dispersed throughout the surface layers of the core.

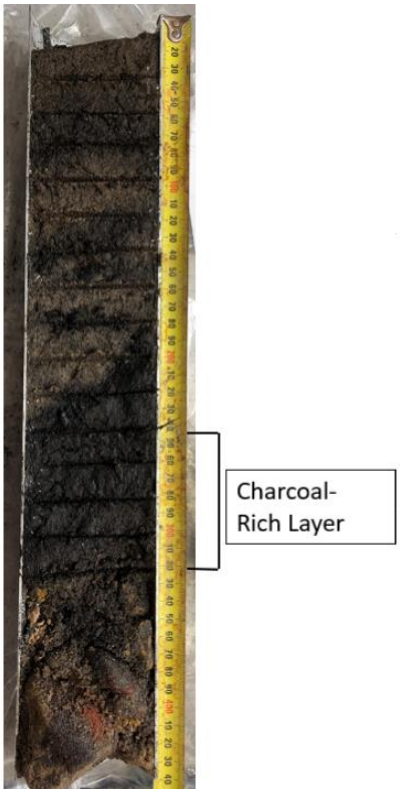

Figure 3.6 Washhouse Gully 1 Core 1 highlighting the primary charcoal layer at 24-32cm with charcoal also interspersed throughout the surface layers.

4 Methods

In this chapter, the methodology for the project is outlined. A general flow chart of the methods is summarised in Figure 4.1.

4.1 Field Methods

Following consultation with fire severity maps, sampling sites were selected such that they drained an area experiencing the highest severity in 2013 to maximise the signal to be detected by the two proxies. In the field, samples were selected on visual assessment of alluvial processes; this was typically on the banks of the creeks themselves. One-metre lengths of 75mm diameter aluminium tubes were hammered into the sediment and, once bedrock was reached, a plug was inserted creating a vacuum seal before removal of the aluminium tube, forming a core. Two cores were collected at each site to ensure the sample was both representative and of ample quantity for analysis. Each core was subsampled at two-centimetre depth intervals. Long Creek was a predominantly bedrock channel so taking a core was not possible and pits were dug. Samples were collected at 5cm depth intervals with additional samples collected for the occurrence of charcoal layers in between designated 5cm intervals.

4.2 Grain Size Analysis

All samples were first analysed on the Malvern Mastersizer 2000 for the determination of particle size distribution. Approximately ¼-½ a teaspoon of the bulk sample was sieved to 1mm to remove any large organic fragments. Background readings were first recorded to remove bias from the bath. The light energy reading was required to be below 120 before the water of the bath was clean enough to add samples. The sample was then added to the bath until the quantity was sufficient to fall within the desired obscuration range. This process was assisted by a sonic pulse to separate aggregated clasts of finer grain sizes. Three measurements were taken in total and averaged to report the percentage of sand (63-1000µm), silt (4-63µm) and clay (<4µm).

4.3 Sieving and Clay Separation

Each bulk sample was halved using a sample splitter for analysis. One half of the bulk was dry sieved to 2mm to separate plant material and large charcoal fragments. The <2mm fraction was then wet sieved using a 63µm sieve and dampened using de-ionised (DI) water. The resulting solutions were dried at 60°C, leaving a dry mud layer at the base of the beaker. This layer was extracted and placed into centrifuge tubes with approximately 0.250g of sodium hexametaphosphate to prevent aggregation of the clays during the separation phase. 40mL of DI water was added to these samples and combined using a mixing wheel. Once mixed, the samples were centrifuged and the liquid, containing the <2µm fraction, comprised of predominantly clay material with a small percentage of organics, was poured off into separate centrifuge tubes, leaving behind a solid. This was repeated four

times until the liquid fraction was predominantly clear following the last repetition to ensure maximum retention of the sample. The remaining liquids, containing the <2µm fraction of the sample, were centrifuged at a higher rpm, leaving a solid residue consisting of the <2µm fraction at the base of the tube and a predominantly clear liquid layer with some remaining organics above. The liquid was poured off and discarded, leaving the solid at the base of the tube. The solids of both fractions were freeze-dried to remove excess water to allow for the use of the <2µm fraction for both alkali fusion and FTIR spectroscopy and 2-63µm fraction for FTIR analysis alone.

4.4 Boron Isotope Analysis

4.4.1 Alkali Fusion

50mg of sample and approximately 250-270mg of potassium carbonate (K_2CO_3) were combined in platinum crucibles, ensuring a fine and well-mixed consistency. A blank and a standard were tested in conjunction with the samples. W2-a diabase rock standard was used as reference material to determine the accuracy of the procedure as it has a known $\delta^{11}B$ value of 12.2±0.4 (Gangjian *et al.*, 2013) and a procedural blank was prepared to determine contamination. These were then placed in the furnace at 950°C for forty minutes, forming a glass. 0.5mL of instrument quality (IQ) 30% hydrochloric acid (HCl) and 3mL of milli-Q water were added to the solid to dissolve the glass. Milli-Q water is ultrapure, containing less than 1ppb of total organic carbon (TOC) and IQ HCl contains less than or equal to 1ppb of metal contaminants so as to minimise possible contamination of the samples. A sonic bath was used to accelerate the dissolving process. Once predominantly dissolved, each sample was transferred to centrifuge tubes and filled with 40mL of milli-Q water. Samples were then centrifuged for 20 minutes duration at 4000rpm.

4.4.2 Cation Exchange Chromatography and Boron-Specific Chromatography

Cation exchange chromatography was used to remove excess cations from the solution, particularly the potassium from the K_2CO_3 used in alkali fusion. This step is important for reducing isobaric interference of other elements during MC-ICP-MS analysis. Due to the state of boron being that of $B(OH)_3$, it is not expected to be retained during cation exchange chromatography. 5mL of the sample was processed through columns containing 1.5mL cation exchange resin. To ensure all boron is recovered, 1mL of 0.01M IQ HCl was passed through twice and collected in the same vessel. In total, 7mL of solution was saved in 15mL centrifuge tubes. Once collected, a pH adjustment to between approximately pH 8-10, was conducted using 0.5M tech-grade sodium hydroxide (NaOH) that was first passed through an Amberlite column to remove any boron present in the solution. This improves the efficiency of the resin for extracting boron from the solution.

Following conditioning of the columns with 5mL of milli-Q water in 3 stages, all of the liquid sample collected during cation exchange chromatography and the pH adjustment were run through the

second set of columns, containing 0.5mL of the Amberlite resin. 2.5mL of milli-Q water was then added in 3 stages followed by 2.5mL of boron-free sodium chloride (NaCl), also in three stages. This step allows for the elution of silica through replacement in the resin by the chloride ion. A final addition of 2.5 mL of Milli-Q water was performed to ensure that all of the NaCl was removed from the resin prior to collection of the sample. 5mL of IQ HCl was then passed through the columns in three stages. A 10-minute break was allowed following the first 1mL addition before the remaining aliquots were passed through the columns. This was collected in a vile ready for analysis by Multi-collector Inductively Coupled Plasma Mass Spectrometry (MC-ICP-MS).

4.4.3 Multi-Collector Inductively Coupled Plasma Mass Spectrometry

The isotopic ratios of boron in each sample were determined using multi-collector inductively coupled plasma mass spectroscopy (MC-ICP-MS) using a ThermoFisher Neptune Plus. Using the quantities of ^{10}B and ^{11}B, the $\delta^{11}B$ value was also discerned. Since the plasma is an inefficient mechanism for dissociating large droplets of a sample (Thomas, 2001), the combination of a peristaltic pump and cyclonic spray chamber were used to promote the formation of an aerosol for entry into the plasma. The peristaltic pump operates using a small pump with minirollers rotating at the same speed, creating a constant pressure (Thomas, 2001) that feeds the sample into the APEX PFA ST nebuliser at approximately 100µl/min. This remains constant for all samples, standards and blanks. The nebuliser condenses the sample into an aerosol through pneumatic gas flow, where it is then passed into the cyclonic spray chamber (Thomas, 2001). A vortex is produced within the spray chamber through the interaction of the sample aerosol and the argon gas, discriminating droplets on the basis of size. The smaller droplets are carried into the interface region by the gas stream through two metal cones (Thomas, 2001)- a standard nickel (Ni) sample cone and Ni H skimmer cone, whilst the larger droplets are removed through the drain. The sample is then directed through the ion optics, into the mass separation device where the ions are separated based on their mass-to-charge ratio (Thomas, 2001). ^{10}B and ^{11}B are then collected in Faraday cups L3 and H3 respectively (Gangjian *et al.*, 2013).

A primary standard of 50 ppb NIST SRM 951 boric acid solution was produced and analysed before and after each sample to correct for mass bias. Secondary standards of both European Reference Material (ERM) AE120 and ERM AE121 boric acids with concentrations of 50ppb were also produced. The secondary standards have a known ratio of $^{11}B/^{10}B$ and were analysed as unknowns before and after all samples as a measurement of instrument accuracy.

4.5 Fourier Transform Infrared Spectroscopy

4.5.1 Attenuated Total Reflectance (Attenuated Total Reflectance

Samples were analysed using a Bruker Alpha Platinum ATR spectrometer, with a diamond attenuated total reflectance (ATR) accessory and KBr beamsplitter. The emitted infrared light spectra recorded a

4cm^{-1} resolution across the range of 4000-400cm^{-1} and conducted 64-128 scans per spectrum. Bulk samples were ground using an opal mortar and pestle to achieve a fine consistency. Prior to the determination of the fire-affected bands, a baseline correction spectra was performed in R using the 'baseline' package version 1.3-0 (Liland, Mevik and Canteri, 2020). FTIR was then performed on specific fractions (clay, sand, silt and charcoal) of the samples in order to determine changes in the matrix as a result of fire exposure.

4.5.2 Potassium Bromide (KBr) Discs

Bulk Washhouse Gully 1 Core 1 samples were sent to Comenius University in Slovakia for FTIR analysis by potassium bromide (KBr) discs. Each sample was prepared by first grinding approximately 1 g of sample to a fine powder using a zirconium oxide mill and, once homogenised, dried at 60°C for 24 hours. 2±0.05mg of the sample was then combined with 200mg of KBr and pressed into a small pellet. FTIR analysis was performed using a NICOLET 6700 FTIR spectrometer and OMNIC 8 software (Thermo Scientific). Spectra were recorded in the mid-infrared region from 4000-400cm^{-1} with resolution of 2cm^{-1}. The analysis was conducted in transmission mode and expressed as absorbance values averaged from 128 scans.

4.6 Total Carbon and Nitrogen Analysis

To determine the concentrations of both carbon (C) and nitrogen (N), samples were tested using an Elementar Element Analyser (EA). All samples were prepared for analysis by grinding 100-200mg of the bulk (Washhouse Gully 1 Core 1) and silt fraction (Rebecca Creek 2017 samples) to a fine, even consistency. A crucible was created using foil and approximately 50mg of the sample was added. The exact weight was recorded in the run sheet before the "crucible" was folded in such a way as to minimise sample leakage. Four blanks were tested at the beginning of the sequence, with the first two as test samples to allow cleaning and flushing of the system. Three 50mg phenylalanine samples were also analysed as primary standards for calibration after the blanks. One additional blank was analysed after the 3 standards and before the samples. A repeat sample was analysed every four, and phenylalanine primary standard every 10 samples, to account for drift. Phenylalanine was also analysed as a sample at the end of the sequence as a secondary standard to ensure quality control.

4.7 Radiocarbon Dating

The Rebecca Creek 2017 samples displayed two charcoal layers at 25-30cm and 37-40cm respectively. Charcoal fragments were hand-selected and sent to the University of Waikato in New Zealand for Accelerated Mass Spectrometry (AMS) radiocarbon dating. Samples were treated with HCl followed by NaOH and then HCl once more before filtration, rinsing and drying to graphite for analysis on the AMS spectrometer. Bomb radiocarbon dating was applied to the samples. This method analyses the period between 1950 and 2010. Tropospheric $\Delta^{14}C$ began increasing in 1955 due to aboveground

detonation of nuclear bombs in the Northern Hemisphere. These levels continued to rise, reaching a maximum in the mid-60s (Hua, Barbetti and Rakowski, 2013). Since then, atmospheric $\Delta^{14}C$ decreased through the absence of major atmospheric detonations and combustion of fossil fuels free from ^{14}C. Since the majority of nuclear detonation occurred in the Northern Hemisphere, there is a significant gradient not only between hemispheres but between high and low latitudes (Hua, Barbetti and Rakowski, 2013). For this reason, zones are applied when analysing samples using this method (Hua, Barbetti and Rakowski, 2013). The Southern Hemisphere zone 1 and 2 compilation was applied to the Rebecca Creek samples collected in 2017. The $\delta^{13}C$ was measured on the prepared graphite and the approximate ages determined against this calibration curve.

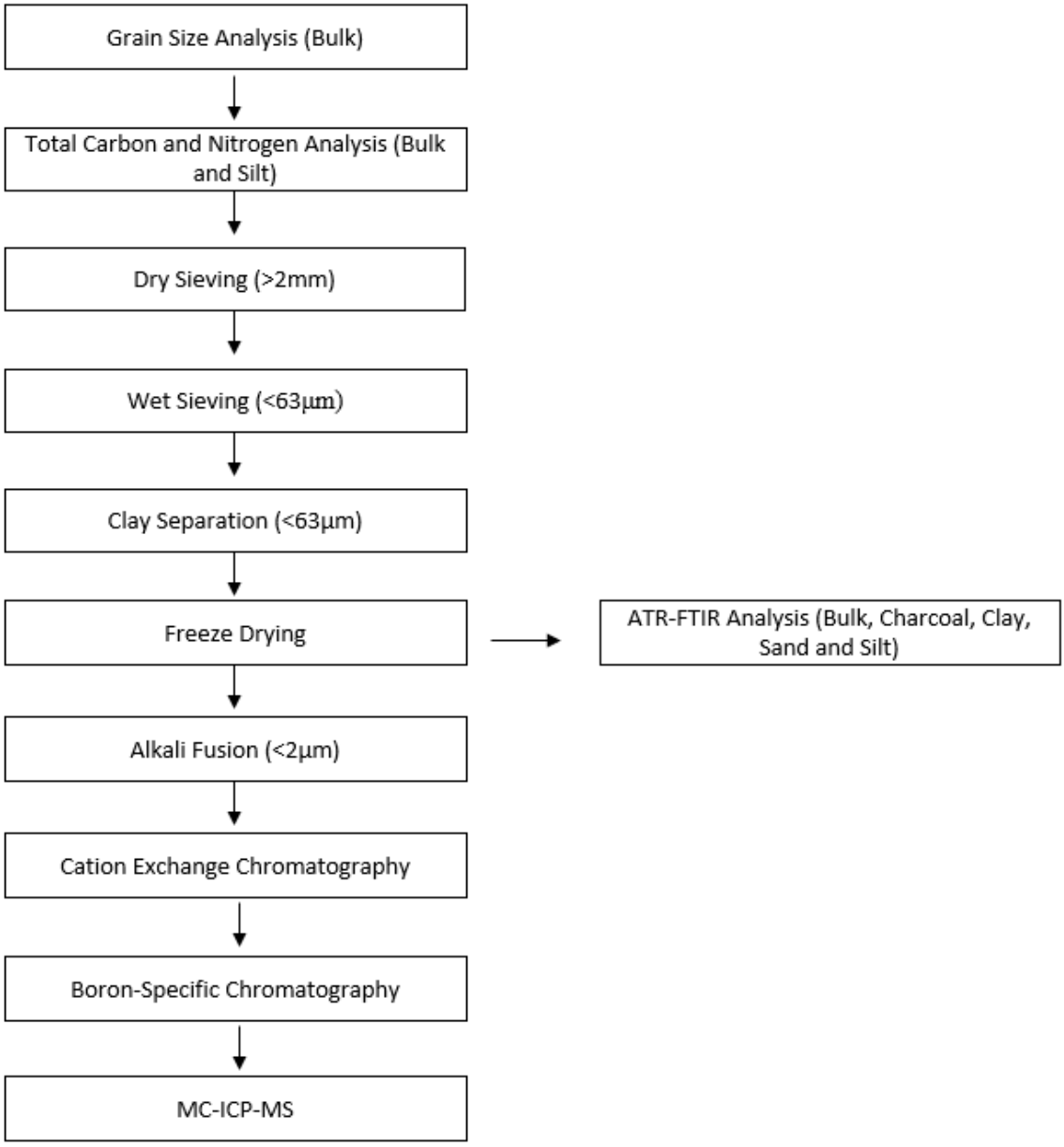

Figure 4.1 A summary of the various procedures used for sample preparation.

5 Results and Discussion- Washhouse Gully 1 Core 1

In this chapter, results from the 2017 Rebecca Creek samples are compared to Washhouse Gully 1 Core 1. Both sites analyse the 2013 bushfire.

5.1 Radiocarbon Dating

Radiocarbon ages for the 2017 Rebecca Creek samples highlight ages between cal BP -60.27 and cal BP-54.45 for 25-30cm depth. The charcoal-rich layer at 37-40cm depth recorded ages between cal BP -61.12 and cal BP-56.33 (Figure 5.1). AD 1950 is used as a "base year", representing 0 yr BP (Stuiver and Polach, 1977). Considering this, the radiocarbon results suggest years of 2004-2010 and 2006-2011 for 25-30cm and 37-40cm depth respectively. Using the median, this can be summarised to 2007±3 and 2009±2. Prior to the 2013 fire, the area had long since been burnt at high severity. Therefore, whilst it was initially hypothesised that the two charcoal-rich layers at 25-30cm and 37-40cm highlighted the occurrence of two separate fire events, the radiocarbon ages suggest derivation from the same event. Younger samples less than 100 years can experience some calibration issues (Pierce, Meyer and Jull, 2004) and it is, therefore, likely that the age discrepancy is analytical. The results, therefore, suggest that the charcoal may have been mobilised as a result of two separate erosion events, causing the formation of two charcoal layers within the sedimentary sequence. This could align with the two major rainfall events on the 25th March (67mm) and 18th of August (71.4mm) 2014, at which time revegetation would have been insufficient to reduce erosion potential of the catchment.

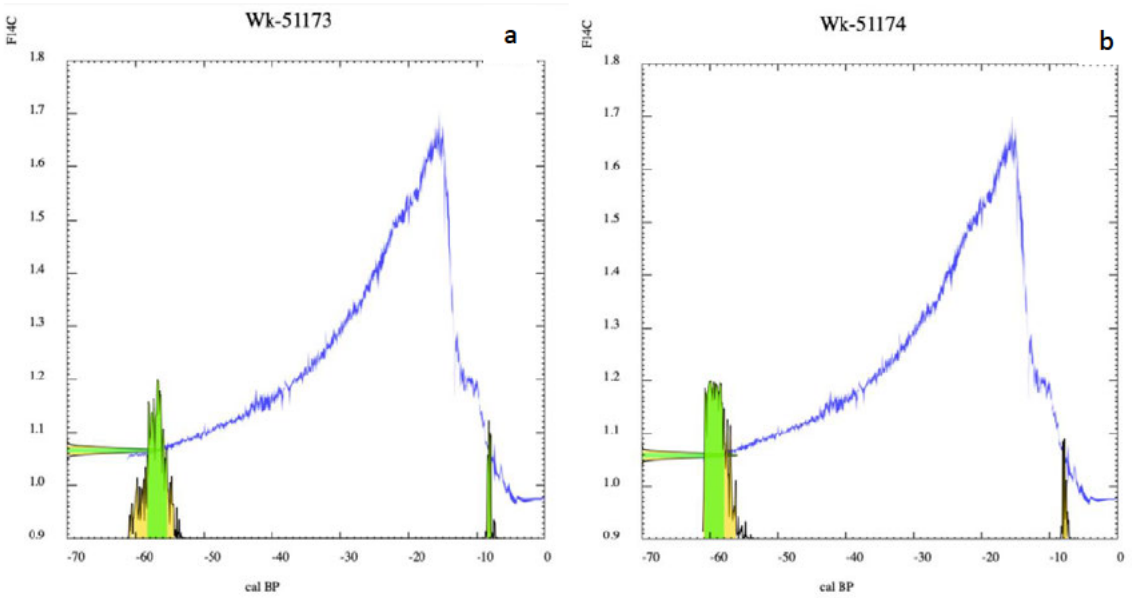

Figure 5.1 Radiocarbon ages for a) 25-30cm and b) 37-40cm with the fraction of modern ^{14}C (F14C) displayed on the y-axis and calibrated age between 1950 and 2010 on the y-axis in relation to changes to atmospheric ^{14}C (blue curve).

5.2 Grain Size Analysis

Grain size analysis of Washhouse Gully 1 Core 1 highlights a predominance of sand with concentrations largely between 60 and 80% for much of the core. The silt and sand fractions highlight an inverse relationship down core suggesting heterogeneous energy of the system over time. An increase in sand and subsequent decrease in silt concentrations are indicative of higher flow energy of the creek. Lower energy is punctuated by increased finer grain size concentrations and consequent reduction in sand. The clay fraction displays greater uniformity down core and highlights significantly decreased concentration contrast with the silt and sand fractions (Figure 5.2).

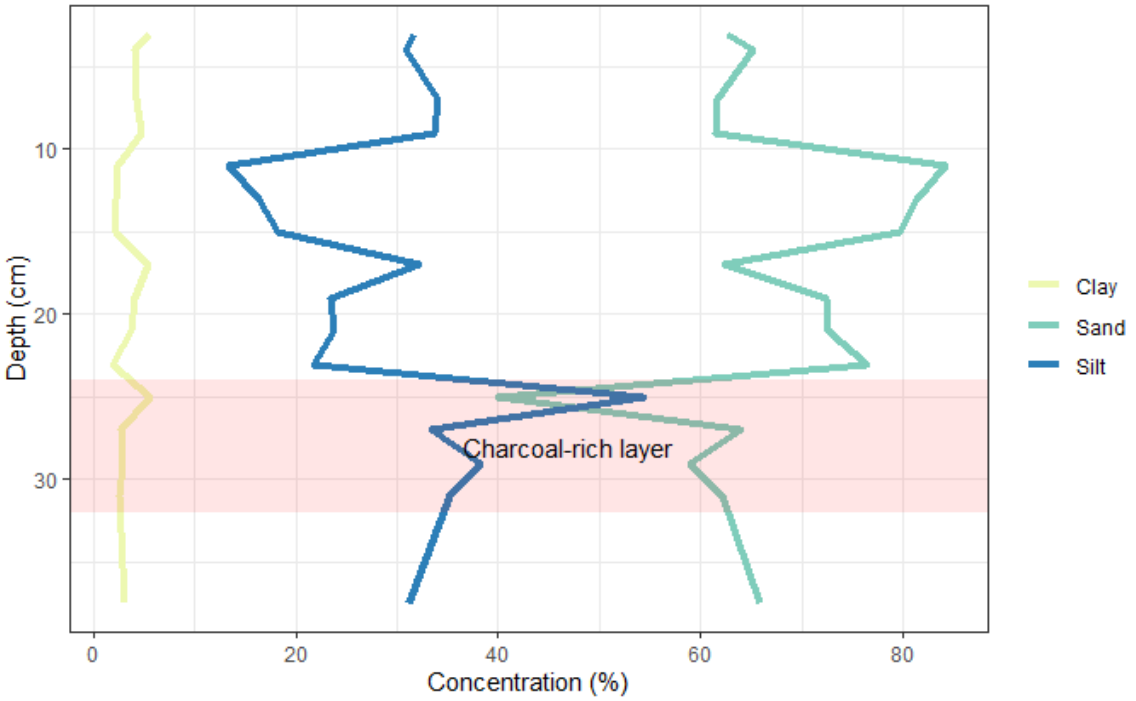

Figure 5.2 Grain size data for Washhouse Gully 1 Core 1, highlighting the changes in clay (yellow), sand (green) and silt (blue) in relation to the identified charcoal-rich layer at depth 24-32cm. This figure and all remaining figures in this section are produced using the ggplot2 package in Rstudio (Wickham, 2016).

Disturbances affecting vegetation, such as fire, result in increased sediment yield, due to destruction of vegetative stability and elevated surface runoff from altered raindrop penetration (Dinis *et al.*, 2020). These effects can be further accentuated by the terrain of the affected landscape, leading in background exceedances of as much as an order of magnitude (Lamb *et al.*, 2013). A number of factors contribute to this increase; in steep landscapes, the dry ravel process of gravity transport of sediment from hillslopes to channels is increased post-fire- a product of drier conditions and reduced vegetative cover (Florsheim *et al.*, 2016). Sediment supply and the dynamic interrelationship between storage, release and subsequent transport all contribute to the magnitude of debris flows, particularly in cases where the slope is steeper than the angle of repose (Dibiase *et al.*, 2017). Finer grain sizes create water quality concerns due to heightened turbidity and particle-associated contamination; its probability is

determined by the transmission ratio which determines the proportion of clay-sized material reaching the reservoir (Nyman *et al.*, 2020). The charcoal-rich layer for Washhouse Gully 1 Core 1 was likely deposited during the first major flood event following the 2013 bushfire, before such time that revegetation was sufficient to provide stability. Higher flow stages promote transport of coarser grain sizes (Shih and Komar, 1990), as highlighted by the peaks in sand at 26-28 and 30-32cm depth. A peak in finer grain sizes at approximately 24-26cm depth suggests the deceleration of this first flood event (Fisher *et al.*, 2008). Mobilisation of finer grain sizes is higher post-fire than an erosion event alone as a result of reduced stability (Dinis *et al.*, 2020).

A second, later erosion event is suggested at 16-20cm depth. This is characterised by a peak in the finer grain sizes at approximately 16-18cm, highlighting the deceleration of the second flood. The second event is less pronounced than the first erosion event. Deposits with a higher composition of finer grain sizes are more resistant to later erosion events as a result of vegetative colonisation and associated stability (Fisher *et al.*, 2008). Sandstone terrains have also proven a greater resilience to fire-induced erosion, despite high levels of soil water repellency (Doerr *et al.*, 2014). Since the Washhouse Gully 1 Core 1 samples are largely derived from Hawkesbury Sandstone parent material, this may explain the reduced erosion following later rainfall and flood events.

5.3 Total Carbon and Nitrogen Analysis

5.3.1 Nitrogen Composition

Fire typically alters a number of key processes driving the nitrogen cycle in the natural environment. Without fire, complex organic nitrogen is formed through the decomposition of plant litter. Microbial organisms decompose this nitrogen to a lower-molecular weight form that can undergo nitrification or mineralisation (Richards *et al.*, 2012). Fire not only volatises and pyrolises nitrogen (Nave, Vance and Swanston, 2011; Richards *et al.*, 2012), but also leads to nitrate leaching and subsequent soil acidification and cation stripping (Richards *et al.*, 2012). This occurs through a combination of temperature, hydrophobicity and pH effects which alters water infiltration and microbial activity (Richards *et al.*, 2012). The immediate effects of a fire should, therefore, see a decrease in nitrogen composition. The results for Washhouse Gully 1 Core 1, however, highlight an increase in nitrogen concentration in the charcoal-rich layer (Figure 5.3). This is mirrored in the 2017 Rebecca Creek samples where an increase in nitrogen concentration is evident in both 2013 fire charcoal-rich samples at 25-30 and 37-40cm (Figure 5.4). An increase in nutrient availability is typically observed post-fire as a result of fine root production, increased litter input, nitrogen fixation and incorporation of charred material into the topsoil (Orians and Milewski, 2007; Richards *et al.*, 2012). This would suggest that the fire affected layer was at 32-43cm depth for Washhouse Gully and 32-36cm for Rebecca Creek, proving at odds with other hypotheses to be presented in this chapter.

Several existing studies, however, have shown an increase in nitrogen concentration as a result of exposure to fire. Darker coloured ash, formed as a product of incomplete combustion conditions, resulted in an increase in total carbon and nitrogen concentrations (Dlapa *et al.*, 2013). Consequently, overland flow and leaching from ash can result in transport of cations and nitrates (Bodí *et al.*, 2014). Transport of nitrogen-containing compounds may be aided by the decomposition of ash and organics, facilitating the incorporation of nitrogen into the soil (Alcañiz *et al.*, 2018). This provides a potential explanation for the nitrogen enrichment displayed in the charcoal-rich layers for both Rebecca Creek and Washhouse Gully. Alternatively, ammonium is formed as a direct product of combustion. In the weeks and months following a fire event, nitrate forms of ammonium are produced through nitrification (Certini, 2005), thus also increasing the concentration of nitrogen in the soil.

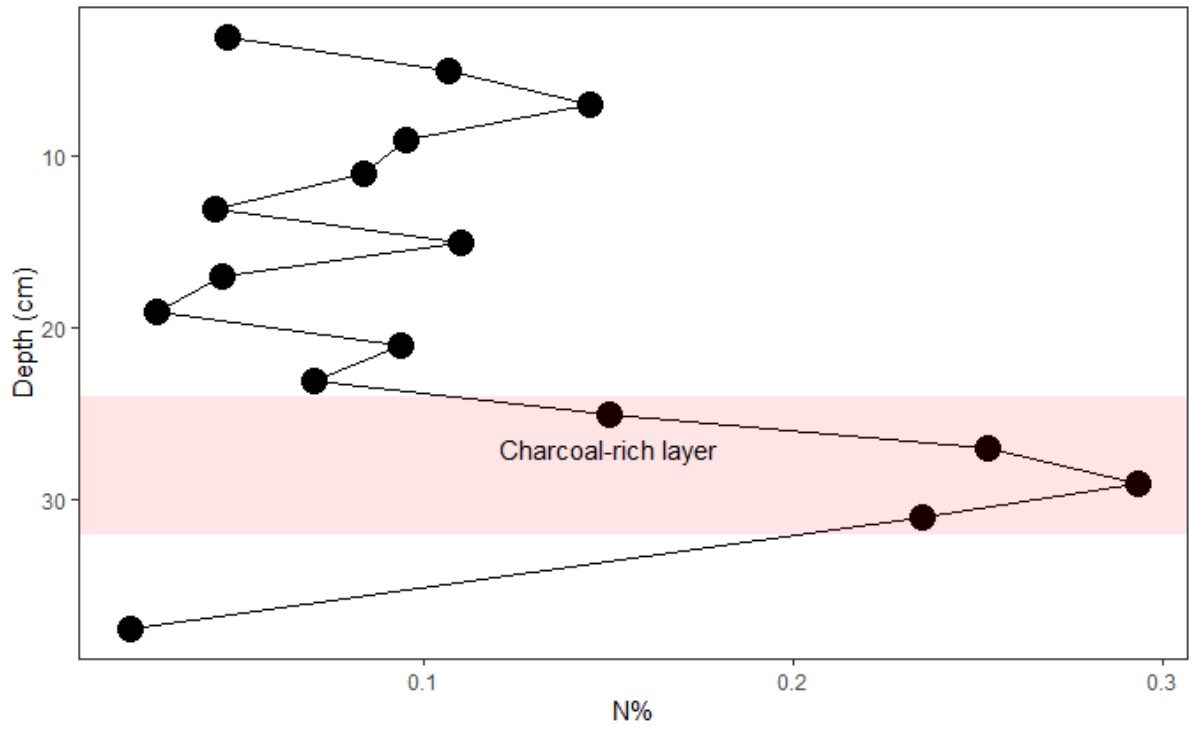

Figure 5.3 Nitrogen concentration as a function of depth for Washhouse Gully 1 Core 1 bulk fraction with respect to the charcoal-rich layer at 24-32cm (identified in red).

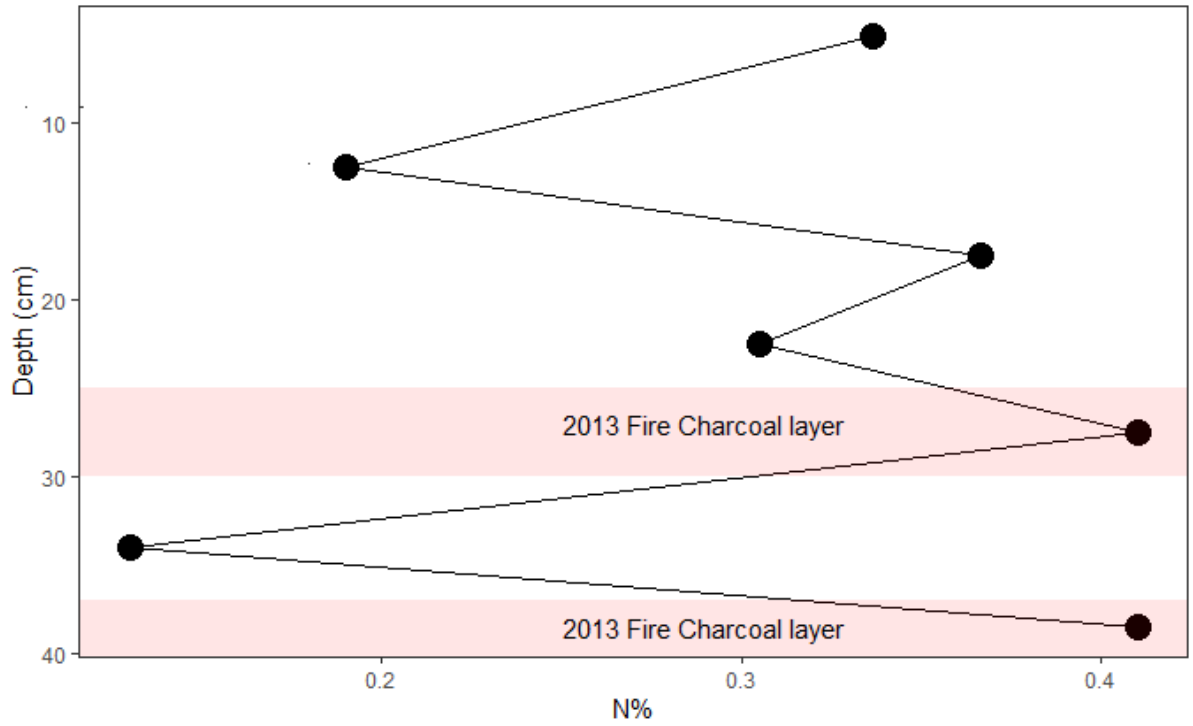

Figure 5.4 Nitrogen concentration as a function of depth for Rebecca Creek silt fraction with respect to the charcoal-rich layers at 25-30cm and 37-40cm depth (identified in red).

5.3.2 Carbon Composition

Natural forests and woodlands provide important sites for storage of organic carbon (Sawyer *et al.*, 2018b) that, when exposed to disturbances such as fire, may undergo transfer between the terrestrial sphere and the atmosphere (Sawyer *et al.*, 2018a). Fires create a spectrum of biologically fixed carbon from living plant tissue to fully consumed ash and soot. The heat of the fire rarely reaches beyond surface layers of approximately 0-5cm depth (Sawyer *et al.*, 2018b). In addition, the release of carbon dioxide into the atmosphere during a fire event has shown relatively short-term effects on the organic carbon stores of the soil (Kolka *et al.*, 2014). The carbon composition of Washhouse Gully 1 Core 1 highlights large variation in carbon concentration in the surface layers with a peak occurring within the charcoal rich layer at 24-32cm (Figure 5.5). The degree of combustion completeness influences the total carbon presence within the soil (Pereira, Úbeda and Martin, 2012). Higher combustion completeness results in reduced carbon composition (Pereira, Úbeda and Martin, 2012). Fire events are often a combination of both complete combustion and pyrolysis conditions (Mastrolonardo *et al.*, 2014). Considering the peak in carbon composition, this suggests that either temperature was insufficient to result in mineralisation to ash or pyrolysis conditions predominated in the 2013 fire. Comparing this to Rebecca Creek (Figure 5.6), there is no obvious trend with depth. This discrepancy may be the result of a variation between fractions. Total carbon and nitrogen analysis was conducted on the silt fraction for Rebecca Creek as the bulk fraction was not available at the time of analysis. The bulk fraction was analysed for Washhouse Gully; therefore, it is possible that the composition of

microcharcoals is more dominant in the silt fraction owing to their increased mobility throughout the sediment profile.

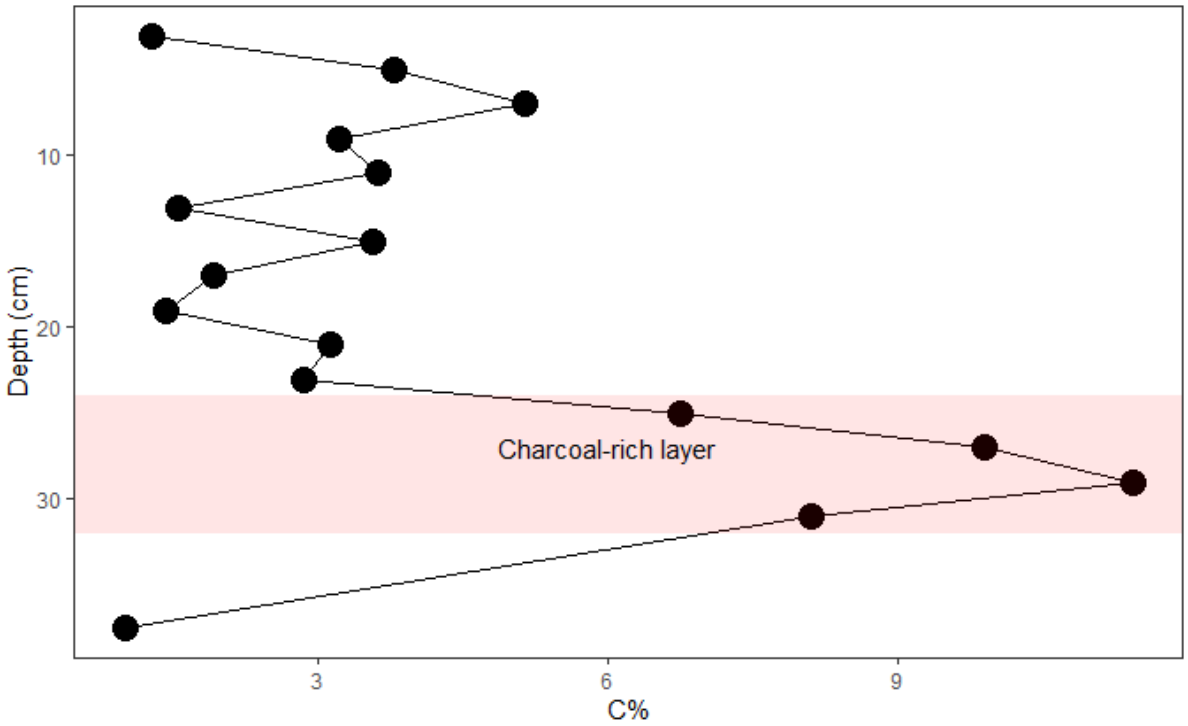

Figure 5.5 Carbon concentration changes as a function of depth for Washhouse Gully 1 Core 1 bulk fraction with relation to the identified charcoal layer at 24-32cm.

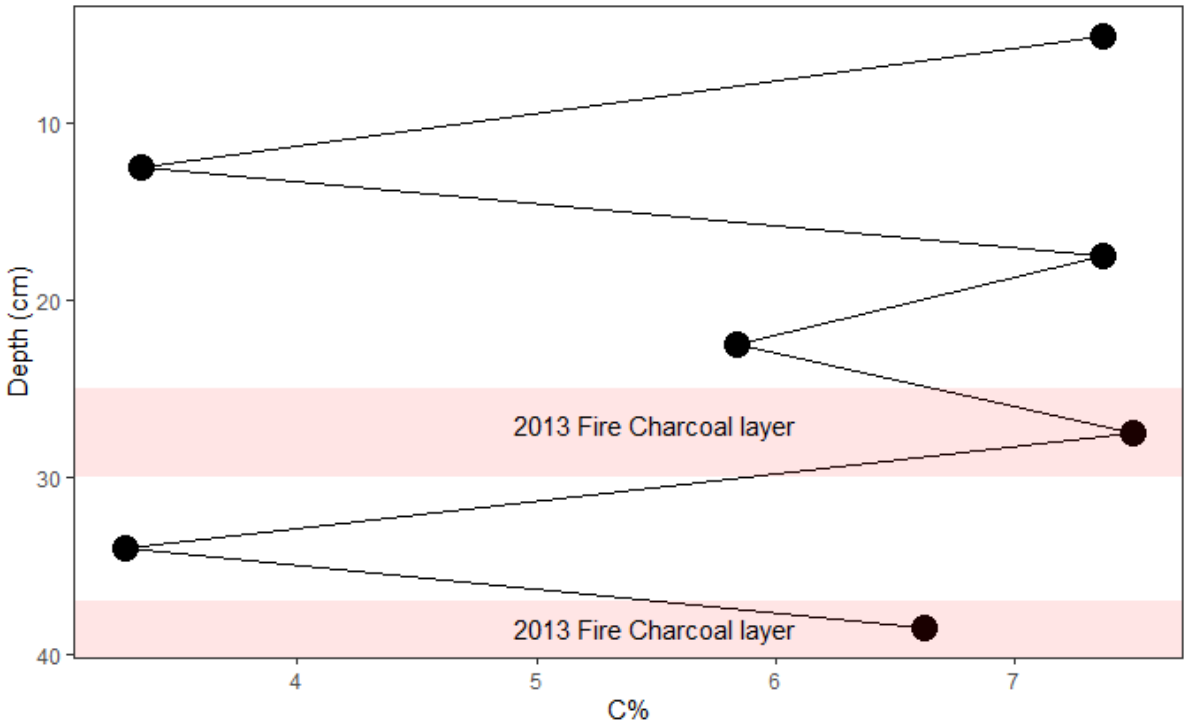

Figure 5.6 Carbon concentration as a function of depth for Rebecca Creek silt fraction with relation to the identified charcoal layers at 25-30cm and 37-40cm.

5.3.3 Carbon/Nitrogen Ratio

The carbon/nitrogen ratio (C/N) typically decreases with depth in the sediment profile as a result of organic matter decomposition (Krull, Thompson and Skjemstad, 2004). Charcoal, however, does not allow for microbial respiration, nor is it a source of available energy for microbial organisms, therefore it maintains a similar C/N ratio to the vegetation from which it originates (Krull, Thompson and Skjemstad, 2004). Therefore, charcoal-rich layers should have an increased C/N ratio. For Washhouse Gully 1 Core 1, this is not the case (Figure 5.7). A general increasing trend is evident with depth, the largest peak in C/N ratio is present at 18-20cm depth for Washhouse Gully 1 Core 1. This may suggest increasing charcoal presence with depth; however, this does not explain the reduced C/N ratio in the charcoal-rich layer. Similarly, Rebecca Creek highlights an increase in the C/N ratio between the designated fire-affected layers (32-36cm) (Figure 5.8). The charcoal layers for both creeks experienced an uncharacteristic increase in nitrogen concentration. Charcoal produced from the combustion of leaves and grasses typically results in higher nitrogen concentrations (Nocentini *et al.*, 2010) highlighting fuel to be the possible driver for this increase. The C/N ratio can also be affected by particle size; decreasing particle size results in a lower C/N ratio. This was hypothesised to occur due to increased composition of wood and bark in the coarser fractions (Nocentini *et al.*, 2010). Comparing the C/N ratio for Washhouse Gully to the grain size results discussed in section 5.2, there is no obvious correlation between peaks in finer grain sizes and the C/N ratio. However, comparison of the two creeks highlights a significantly lower C/N ratio for the silt fraction analysed for Rebecca Creek contrast with the bulk fraction from Washhouse Gully. This suggests that there are some grain size effects, however the peaks in finer grain sizes throughout the Washhouse Gully core are insufficient to significantly affect the C/N ratio. The lack of peak in the charcoal layer is likely linked to the elevated nitrogen composition which proved at odds with findings of existing studies. In comparison with Rebecca Creek, this highlights the inconsistencies associated with this technique as a proxy to determine past fire, suggesting site specific success.

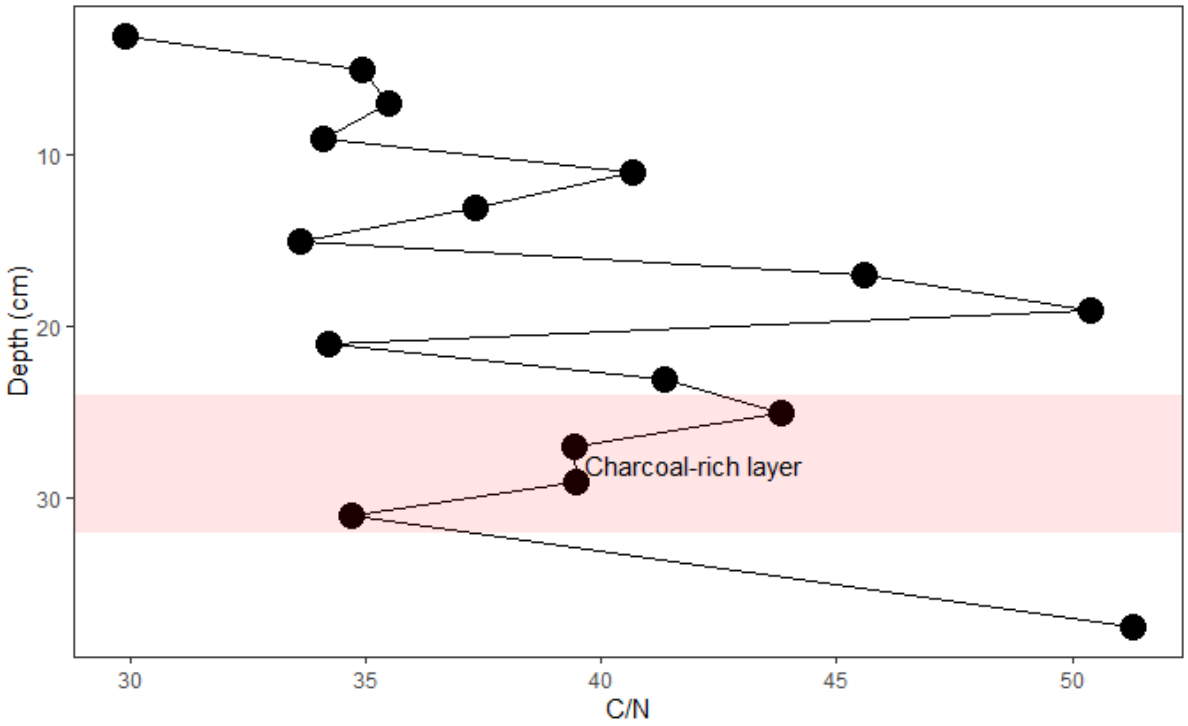

Figure 5.7 Carbon/Nitrogen ratio as a function of depth for Washhouse Gully 1 Core 1 bulk fraction with respect to the charcoal-rich layer at 24-32cm depth.

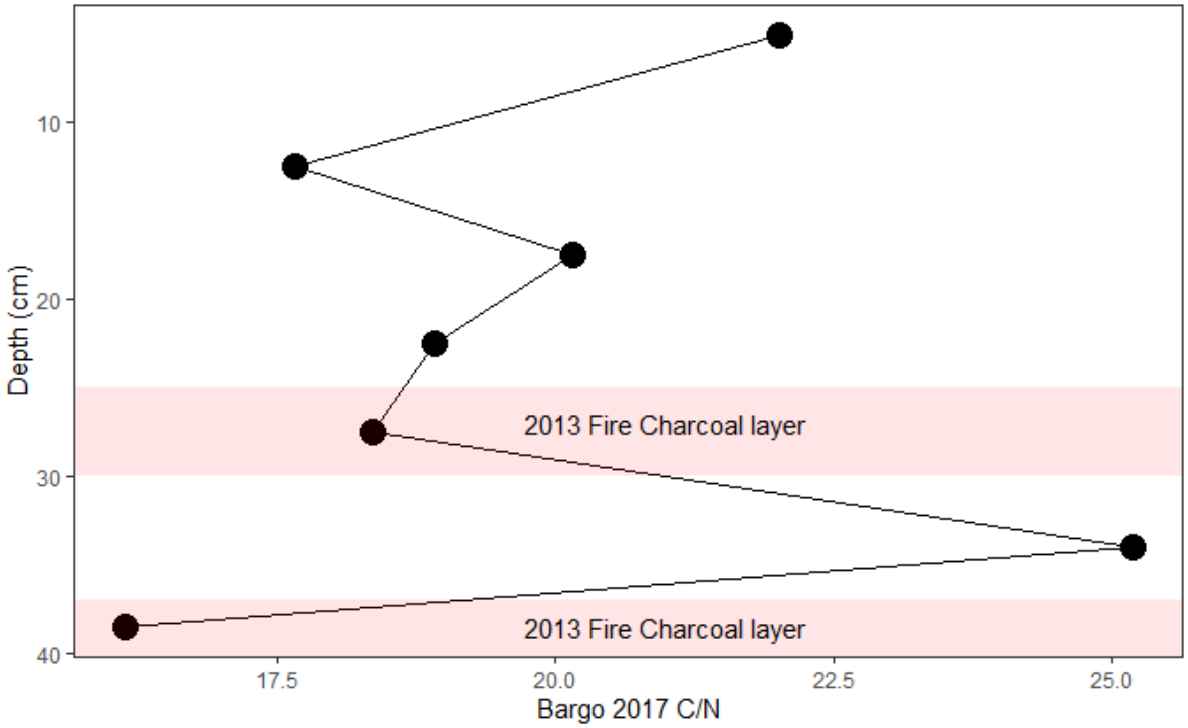

Figure 5.8 Carbon/Nitrogen ratio as a function of depth for Rebecca Creek 2017 silt fraction with respect to the 2013 bushfire charcoal-rich layers at 25-30cm and 37-40cm depth.

5.4 FTIR

Washhouse Gully 1 Core 1 samples were separated into five fractions- bulk (Figure 5.9), charcoal (Figure 5.10), clay (Figure (5.11), sand (Figure 5.12) and silt (Figure 5.13)- and analysed by attenuated total reflectance (ATR)-FTIR. These spectra were compared with the 2017 Rebecca Creek ATR-FTIR spectra for the bulk fraction to determine common trends (Figure 5.14). Spectra were analysed for peak height, shifts and area ratio changes between charcoal-rich and non-charcoal samples to investigate fire-induced changes to chemical bonds. A methods comparison was also conducted between attenuated total reflectance (ATR) and potassium bromide (KBr) discs for the Washhouse Gully 1 Core 1 bulk samples.

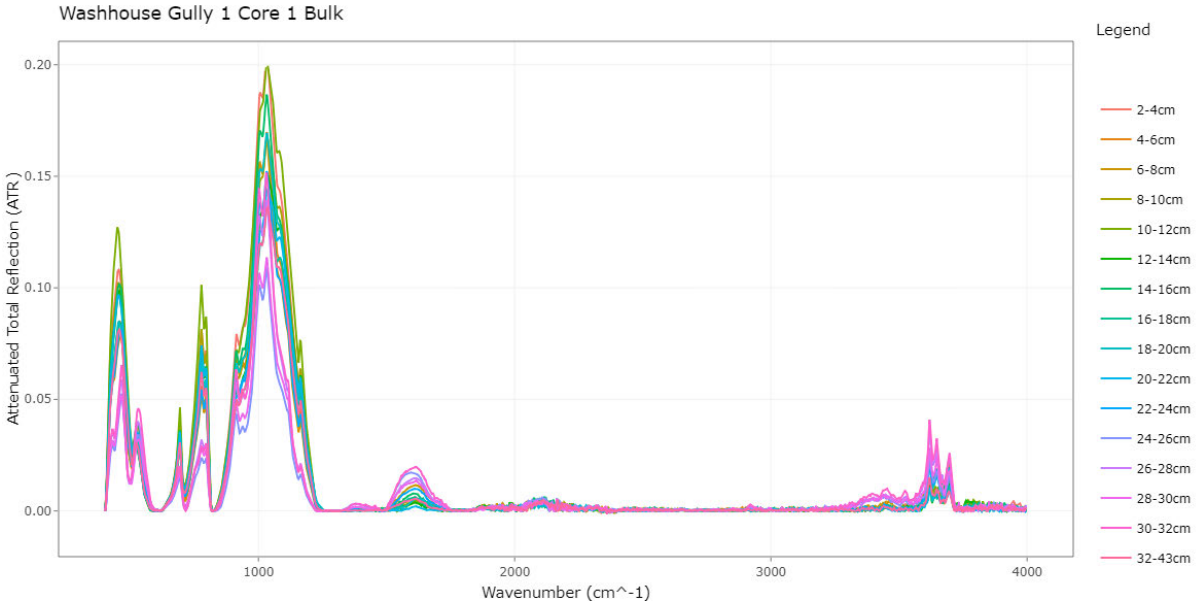

Figure 5.9 Complete (4000-400cm^{-1}) baseline-corrected ATR-FTIR spectra for the Washhouse Gully 1 Core 1 bulk fraction as a function of depth.

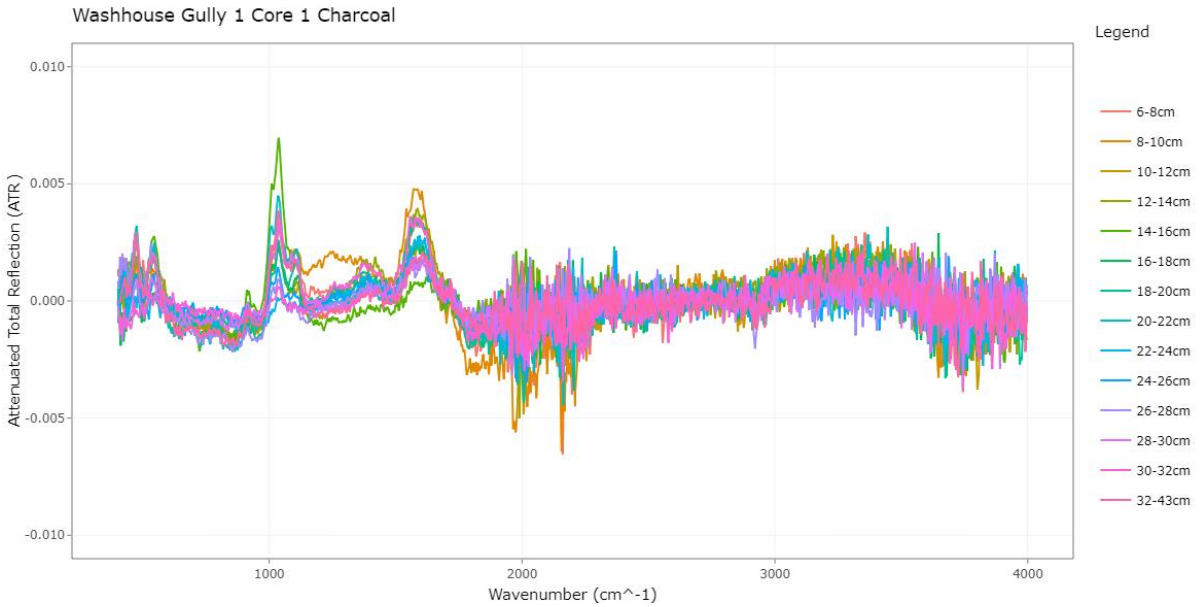

Figure 5.10 Complete (4000-400cm^{-1}) baseline-corrected ATR-FTIR spectra for the Washhouse Gully 1 Core 1 Charcoal fraction as a function of depth.

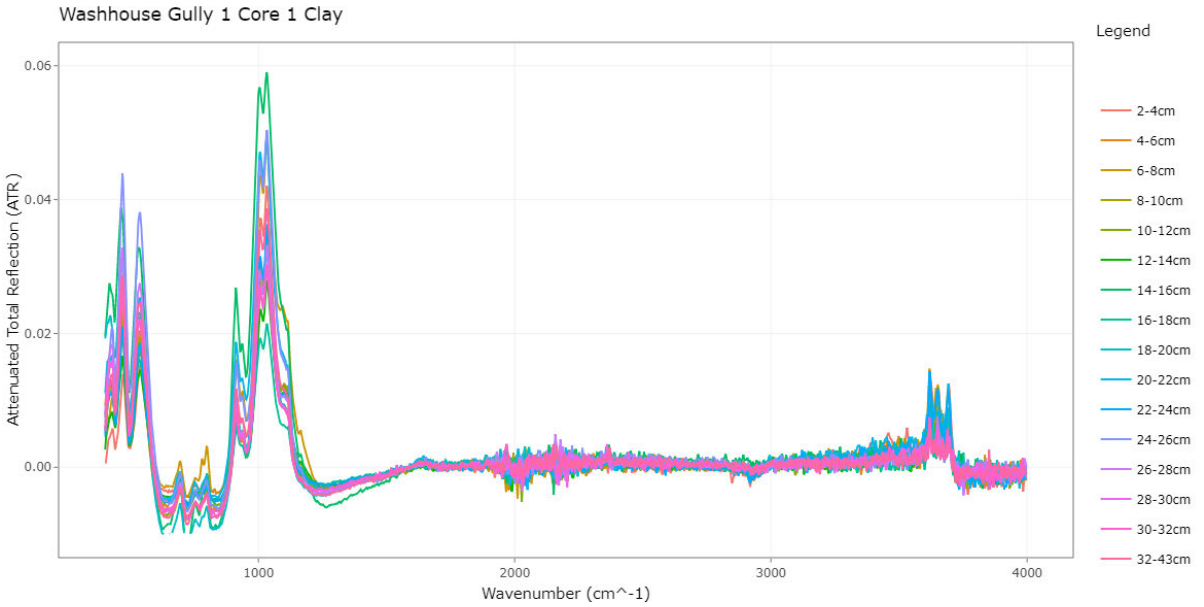

Figure 5.11 Complete (4000-400cm^{-1}) baseline-corrected ATR-FTIR spectra for the Washhouse Gully 1 Core 1 Clay fraction as a function of depth.

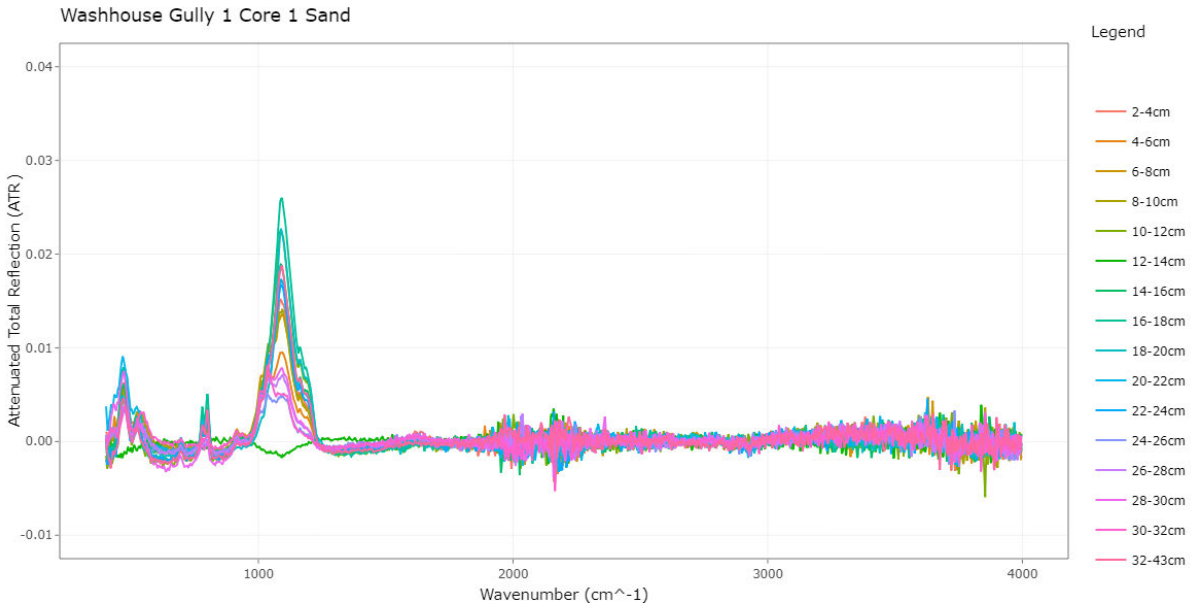

Figure 5.12 Complete (4000-400cm^{-1}) baseline-corrected ATR-FTIR spectra for the Washhouse Gully 1 Core 1 Sand fraction as a function of depth.

.

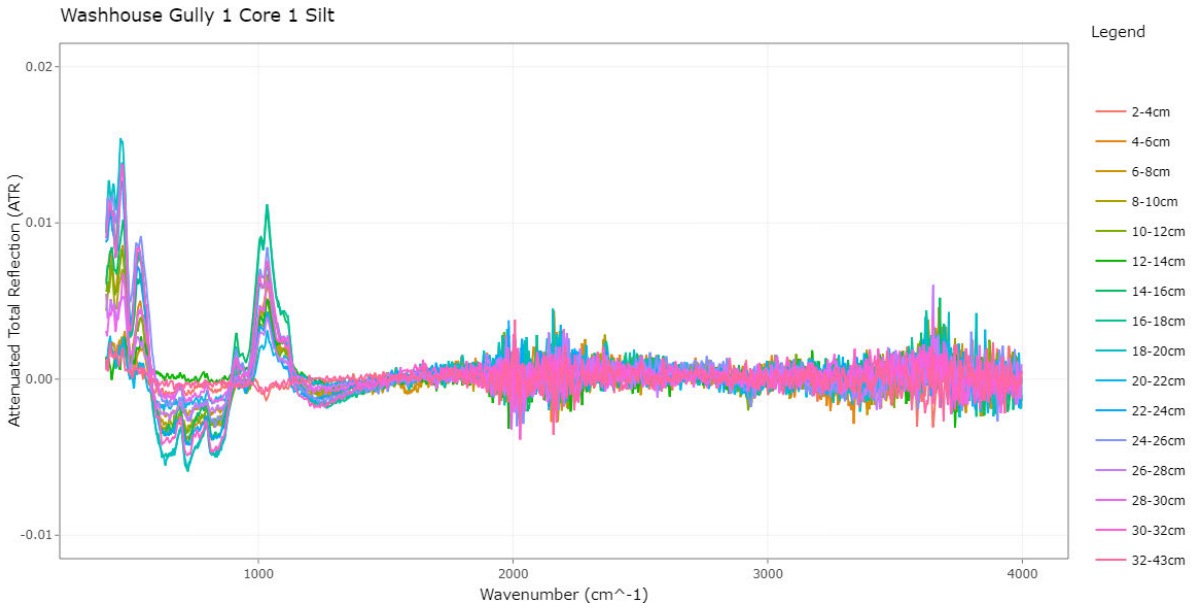

Figure 5.13 Complete (4000-400cm^{-1}) baseline-corrected ATR-FTIR spectra for the Washhouse Gully 1 Core 1 Silt fraction as a function of depth.

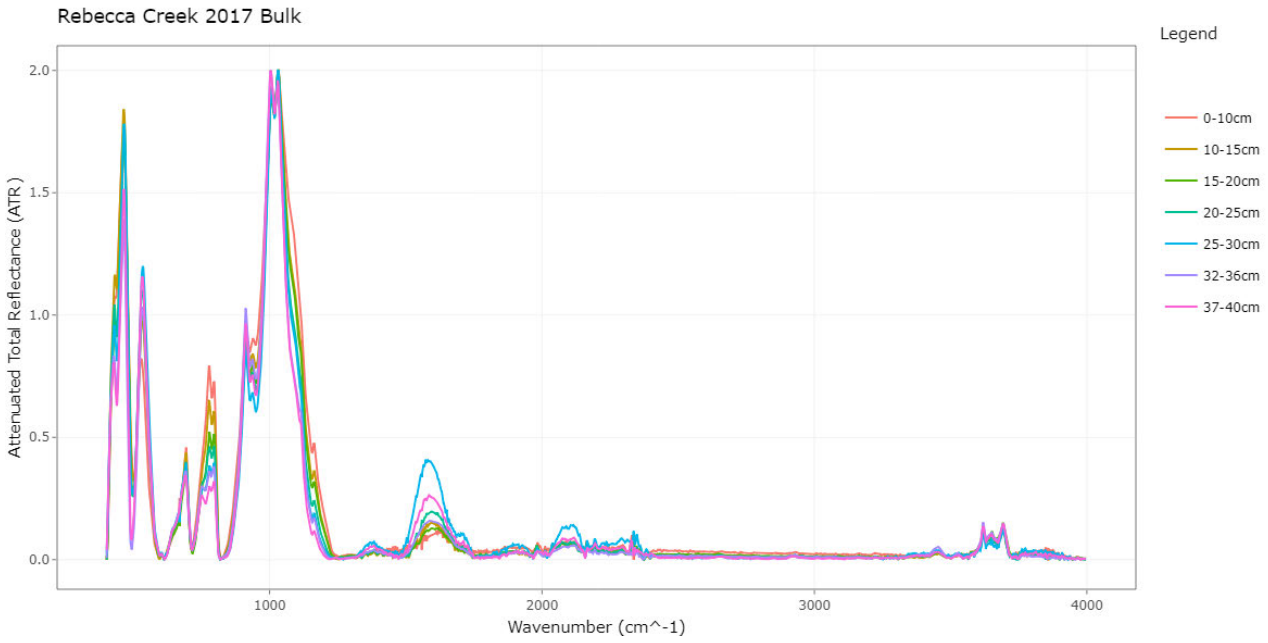

Figure 5.14 Complete (4000-400cm^{-1}) baseline-corrected ATR-FTIR spectra the Rebecca Creek 2017 bulk fraction samples as a function of depth.

5.4.1 Changes to Biopolymers, Organic Matter Composition and Mineralogy

Organic compounds may experience transformation or destruction at elevated temperatures, such as those experienced during a bushfire. Analysing the band at 1030cm^{-1}, the bulk fraction for Washhouse Gully 1 Core 1 highlights a decrease in peak intensity for two of the charcoal-rich samples at 24-26cm and 28-30cm (Figure 5.15) whilst the clay fraction shows no significant difference in peak intensity between samples for this band. The remaining three fractions show considerable variation with depth, with no obvious trend emerging between charcoal-rich and non-charcoal samples (Appendix D.2-5) Rebecca Creek displays a small decrease in peak intensity at 1030cm^{-1} for one of the charcoal rich layers at 37-40cm depth; however, the second charcoal layer does not show this decrease (Figure 5.16). Leaves and grasses are transformed at lower temperatures and have reduced aromatic and recalcitrant charcoal production contrast with woody debris; due to the transformation of carbohydrates at 250°C (Merino *et al.*, 2015). As temperatures increase during a fire, chemical transformations including the formation of aromatic ring structures and gradual condensation of smaller aromatic structures ensue (Merino *et al.*, 2015). A reduction in peak at 1030cm^{-1} is typically associated with symmetric C-O stretching resulting from heating of cellulose, hemicellulose and lignin (Mastrolonardo *et al.*, 2015; Merino *et al.*, 2015). Alternative hypotheses have suggested this peak at 1030cm^{-1} to highlight asymmetric Si-O-Si stretching vibrations of clay minerals (Smidt *et al.*, 2005). As higher combustion completeness is achieved, there is a reduction in ash organic carbon, forcing an increase in the relative mineral content (Bodí *et al.*, 2014). The contribution of the inorganic fraction becomes intensified with increasing temperature which can mask the contribution of the organic bonds (Merino *et al.*, 2015). All samples within the clay fraction display similar, high peak intensities

in the band at 1030cm^{-1}, suggesting Si-O-Si stretching; it is possible that, since the clay fraction likely has the least organic matter of the five fractions, it underwent transformation more rapidly and therefore, the inorganic contributions outweigh the organic signal. The bulk fraction for Washhouse Gully highlights a possible temperature gradient or discrepancy in vegetation type within the charcoal-rich layer. Sediments at 24-26cm and 28-30cm depth appear to have recorded either higher temperatures or may have a higher contribution from woody debris compared to the remaining charcoal-rich layer samples. Rebecca Creek highlights a similar trend with 37-40cm depth suggesting potential elevated temperature or increased woody debris signal compared with 25-30cm.

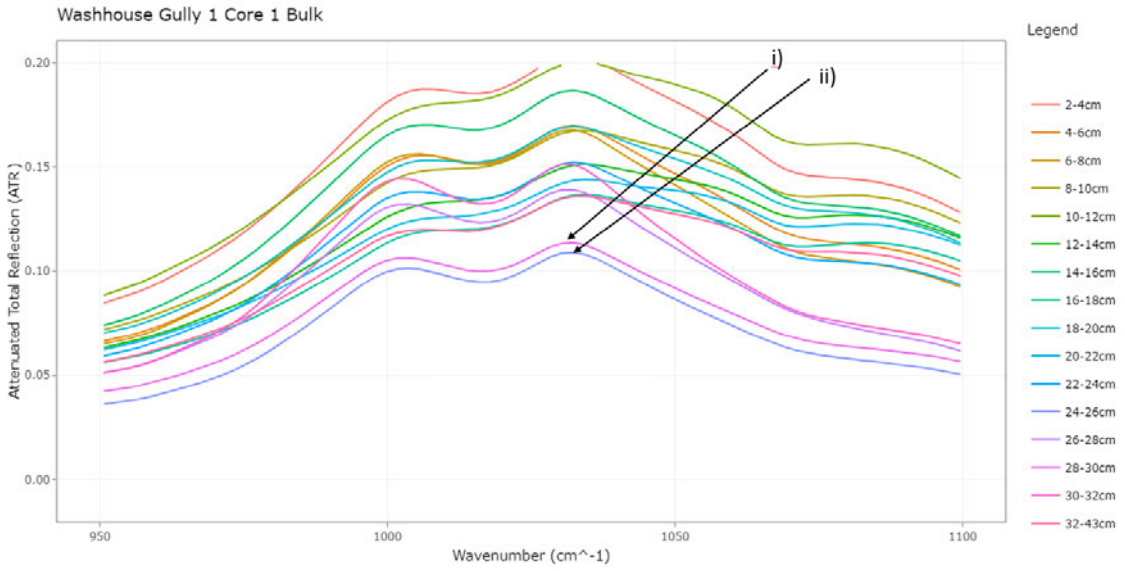

Figure 5.15 Baseline-corrected ATR-FTIR spectra highlighting the band at 1030cm^{-1} for the bulk fraction from Washhouse Gully 1 Core 1. Arrow i) indicates 28-30cm depth and ii) 24-26cm depth, emphasising the decrease in peak for charcoal-rich samples.

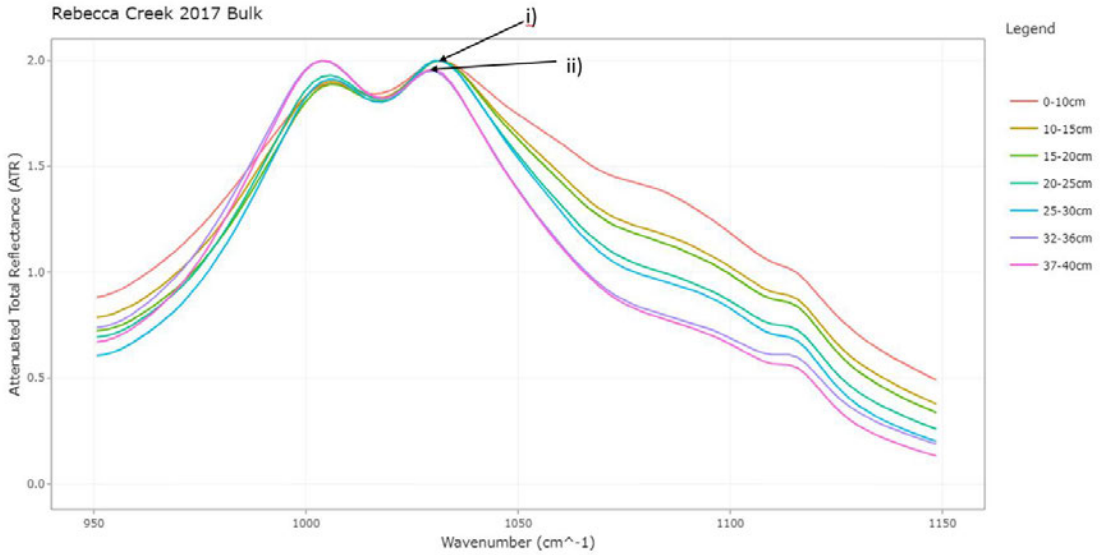

Figure 5.16 Baseline-corrected ATR-FTIR spectra highlighting the band at 1030cm^{-1} for the bulk fraction from Rebecca Creek 2017 samples. Arrow i) indicates 25-30cm depth and ii) 37-40cm depth, emphasising the decrease in peak for 37-40cm depth.

Other biopolymers affect different bands of the spectra. Polysaccharides are absorbed in the band from 1170-950cm^{-1} (Simkovic *et al.*, 2008). A decrease in absorption is evident for the bulk (Figure 5.17) and sand (Figure 5.18) fractions for Washhouse Gully 1 Core 1, suggesting the thermal decomposition of polysaccharide bonds during the 2013 bushfire. The peak at 1514cm^{-1} highlights transformations of lignin; transformation is initiated at relatively low temperatures and complete oxidation occurs at approximately 400-450°C. The intensity of the peak is determined by the degree of aromatisation (Mastrolonardo *et al.*, 2014). No obvious discrepancies are observed in the five fractions for Washhouse Gully 1 Core 1 suggesting either no fire occurrence or a lack of low to moderate severity fires. Rebecca Creek, however, highlights a small increase in peak intensity at around 1514cm^{-1} for both charcoal layers, suggesting a lower severity than that experienced at Washhouse Gully.

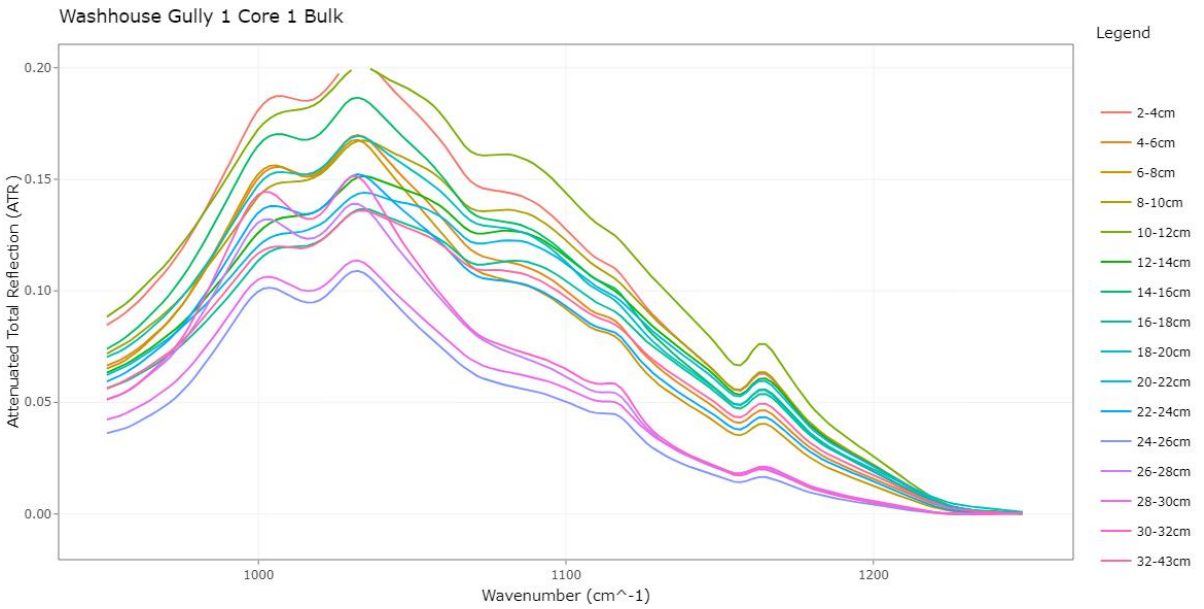

Figure 5.17 Baseline-corrected ATR-FTIR spectra highlighting the band around 1170 to 950cm^{-1} for the bulk fraction from Washhouse Gully 1 Core 1 as a function of depth. Charcoal-rich layers have a reduced peak intensity contrast with non-charcoal-rich samples.

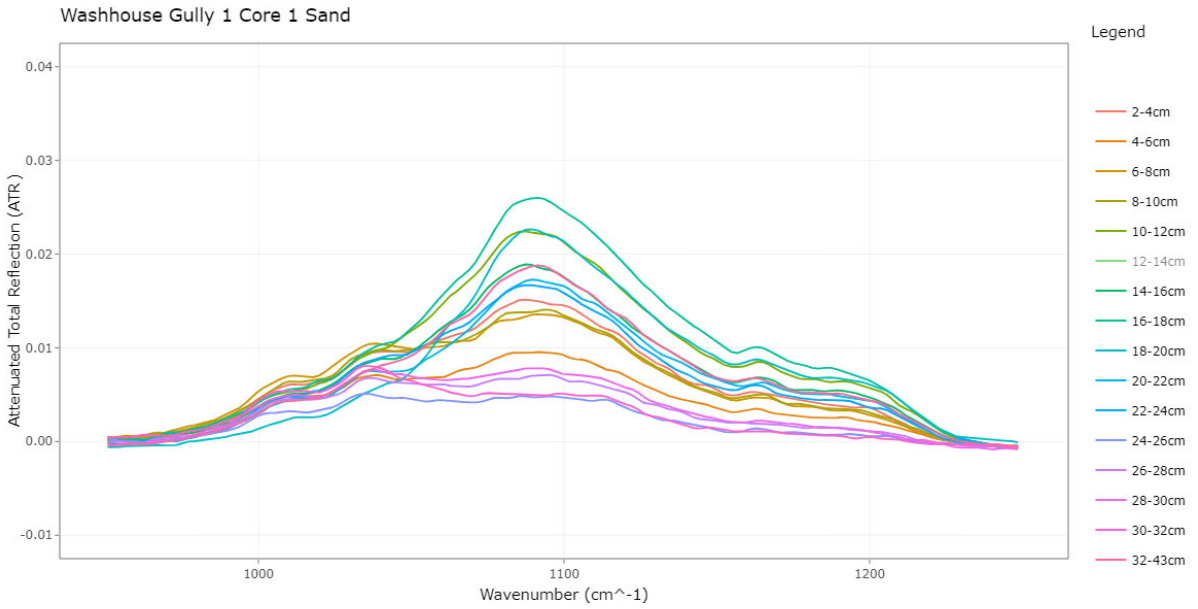

Figure 5.18 Baseline-corrected ATR-FTIR spectra highlighting the band around 1170 to 950cm^{-1} for the sand fraction from Washhouse Gully 1 Core 1 as a function of depth. Charcoal-rich layers have a reduced peak intensity contrast with non-charcoal-rich samples. Sample 12-14cm was not analysed in this band due to poor signal strength.

Decarboxylation has been attributed to the band at approximately 1732cm^{-1}. This band experiences a decrease or complete loss following heating due to a reduction in the contribution of ester carbonyl groups, for instance, uronic acid and acetyl groups from hemicellulose (Mastrolonardo *et al.*, 2014). Washhouse Gully 1 Core 1 and Rebecca Creek highlight no obvious peak or variation from background for either of the sites or fractions. This suggests that carboxylic acids are not present in sufficient quantities to register a signal.

Peak area ratios can allow for the determination of changes in organic matter content and nature following heating. The band from 3000-2800cm^{-1} is assigned to aliphatic CH_x absorption (Guo and Bustin, 1998), whilst 1750-1500cm^{-1} highlights organic matter- particularly aromatic contributions. Aliphatic bands are the first to be eliminated with heating due to the fractionation of long-chain alkanes in preference for shorter chains with lower molecular weight (Abakumov, Maksimova and Tsibart, 2018) causing a loss of soil water repellency at higher temperatures (Simkovic *et al.*, 2008). Aromatics are formed with progressively increasing temperatures (González-pérez *et al.*, 2008). By taking the area under each of these peaks and calculating the ratio of aromatic (1750-1500cm^{-1})/ aliphatic (3000-2800cm^{-1}) signal, it is possible to determine the changes in organic matter quality. The bulk fraction for Washhouse Gully 1 Core 1 exhibits a significant increase in the aromatic/aliphatic ratio within the charcoal-rich layer (Figure 5.19a). This suggests an increase in the production of aromatic compounds and subsequent loss of aliphatic bonds for the charcoal-rich layer contrast with the remainder of the core. The other three fractions show no obvious trend between the charcoal-rich and non-charcoal-rich samples (Figure 5.19). The silt fraction experienced high noise effects and

was not analysed for peak area ratios. The sand fraction is largely inorganic, potentially overprinting the organic signal and masking the changes in aromatic/aliphatic ratio. The ratio can also be influenced by the vegetation type and section of the plant that predominates within the sample. Wood has a higher composition of lignin which forms recalcitrant aromatic structures, significantly increasing aromatic bands (Guo and Bustin, 1998). Aromatic signal may also increase as a result of the thermal decomposition of aliphatics, carboxylic and carbonyl groups (Abakumov, Maksimova and Tsibart, 2018). This is dependent on temperature and combustion completeness, influencing ash properties (Dlapa *et al.*, 2013). Leaves form charred material at lower temperatures than wood, therefore influencing aliphatic signal more significantly due to increased deformation of aliphatic CH_2 and C-O-C phenolic -OH groups (Guo and Bustin, 1998). Due to high aromaticity, charcoal is able to persist in the soil longer than some of its mineral counterparts, giving rise to its classification as a stable pool of organic carbon (Nocentini *et al.*, 2010).

The peak area ratio of aromatics to inorganic bonds allows the determination of changes to organic bonds as a result of heating. The band at 750-600cm^{-1} is assigned to Si-O stretching vibrations (Hahn *et al.*, 2018) which do not undergo dehydroxylation during heating. Charcoal was not included in the analysis of this ratio due to the expected lack of inorganic signal. The bulk fraction highlights a similar trend to the aromatic/aliphatic ratio with major peaks occurring within the charcoal-rich layer at 24-32cm depth (Figure 5.19). The other three fractions show no significant trend, however, may be in part caused by the noise effects in these spectra Figure 5.19). Since Si-O bonds are not affected by heating, they allow a sensitive tracer to changes in organic matter percentage composition with depth. Aliphatic compounds undergo thermal decomposition when heated (Abakumov, Maksimova and Tsibart, 2018) giving way to aromatic formation which are more resistant to temperature-induced change. This ratio highlights the significant enrichment in organics in the charcoal rich layer.

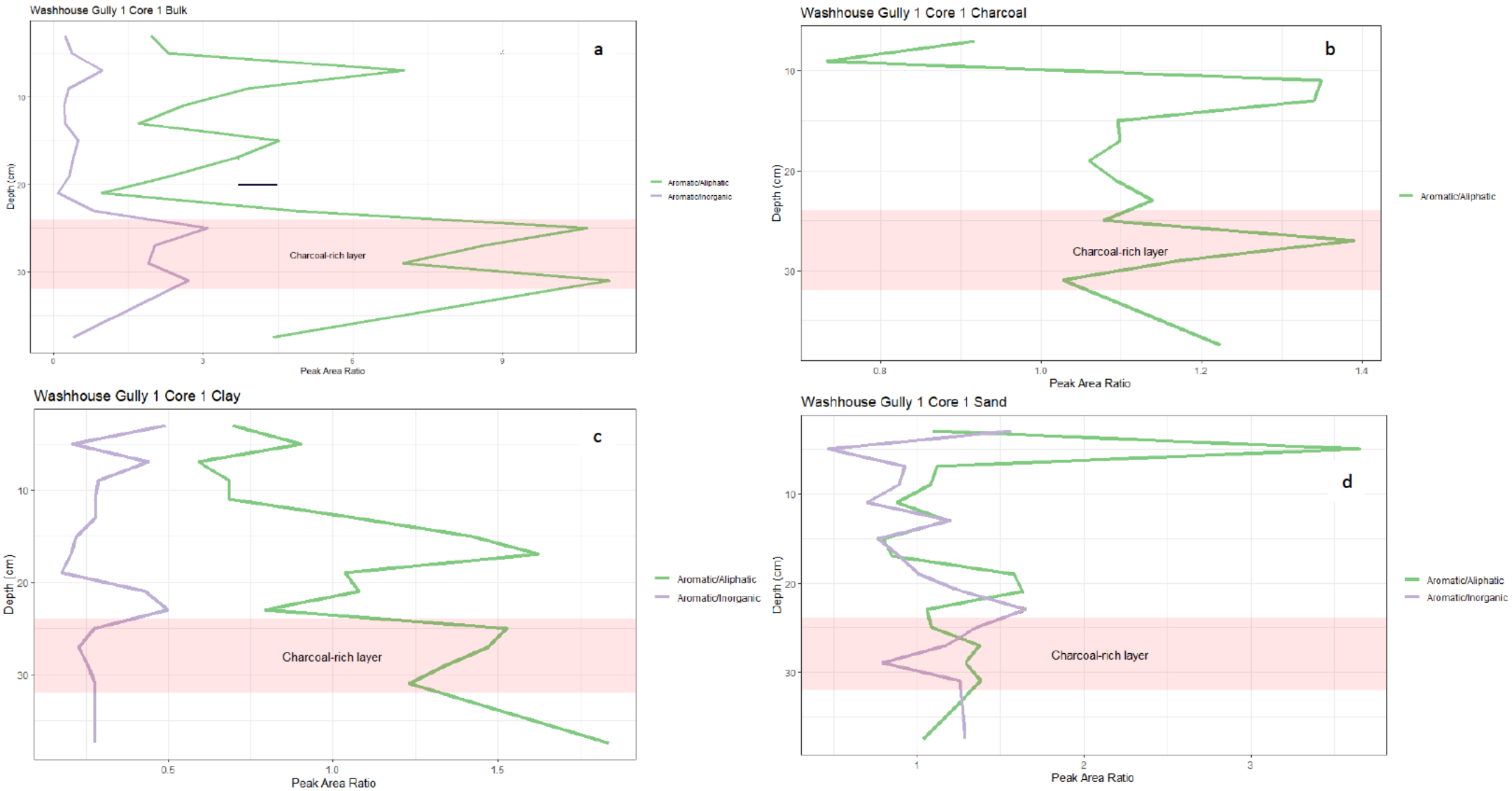

Figure 5.19 Peak area ratios expressing changes in organic matter content ($A_{1750\text{-}1500}/A_{750\text{-}600}$) (aromatic/inorganic) and organic matter quality ($A_{1750\text{-}1500}/A_{3000\text{-}2800}$) (aromatic/aliphatic).

5.4.2 Hydrophobicity and Water Repellency

Soil water repellency typically causes the most significant changes to the FTIR spectra and affects the band from 3020-2800cm^{-1}, however, can also occur as a weak band at 3400cm^{-1} (Krull, Thompson and Skjemstad, 2004; Simkovic *et al.*, 2008). All five fractions (Appendix D.9-13) and Rebecca Creek (Appendix C.3) show little variation from background at these wavenumbers. Soil hydrophobicity can arise from a number of processes including stretching of methyl and methylene groups, increased aromatic and olefinic substances (Smidt *et al.*, 2005; Simkovic *et al.*, 2008), reduced long-chain alkanes with higher molecular weights (Almendros, Martin and Gonzalez-Vila, 1988; Simkovic *et al.*, 2008) or the clogging of pores from increased ash input and clay mobilisation (Certini, 2005). Hydrophobic elements, such as aliphatic hydrocarbons, undergo gasification at temperatures between 200 and 250°C. They then move deeper into the soil profile in response to the changing temperature gradient where they condense on aggregates and single grains, creating a uniform coating. These hydrocarbons decompose completely and irreversibly at temperatures greater than 280°C (Certini, 2005). Canopy consumption, and therefore fire severity, can be approximated from three temperature classifications: low (200-300°C), moderate (400-600°C) and high (600-700°C) (Gosling, Cornelissen and McMichael, 2019). Washhouse Gully and Rebecca Creek both drained an area experiencing the highest severity fire in 2013, therefore, it stands to reason that the sediments transported from the surrounding hillslopes were burnt at temperatures greater than 280°C. Thus, hydrophobicity would likely have been destroyed during the fire and may provide explanation for the lack of peak at 3020-2800cm^{-1} and 3400cm^{-1}. Alternatively, the band at 3400cm^{-1} can also highlight OH bond stretching which may overshadow the peak resulting from hydrophobicity (Simkovic *et al.*, 2008). Since all samples were dried prior to analysis, the OH stretching band may have been reduced or eliminated, causing a subsequent loss of the hydrophobicity trends also.

5.4.3 Combustion Type

A naturally-occurring fire event is not solely a complete combustion reaction; often accompanied by pyrolysis conditions (Mastrolonardo *et al.*, 2014). The reduction of the band at 1095cm^{-1} has been suggested to highlight anaerobic conditions (Doelsch *et al.*, 2009). The bulk and sand fractions highlight a decrease in peak intensity at 1095cm^{-1} for the charcoal-rich samples (24-32cm) (Figures 5.20 and 5.22), whilst the charcoal fraction highlights a decrease in peak for all depths (Figure 5.21). The clay and silt fractions show no significant distinction between samples (Appendix D.14 and D.15). Rebecca Creek highlights a reduction in peak for the deeper charcoal layer (37-40cm), however, the reduction for the 25-30cm depth range is less significant (Figure 5.22). During a bushfire, surface temperatures increase rapidly, resulting in the quick release of volatiles. If there is insufficient air to disperse into the burning material, then pyrolysis conditions predominate (Fang *et al.*, 2006). At temperatures of 300-500°C, pyrolysis increases rapidly and results in the occurrence of additional

exothermic reactions that further increase the temperature unless the heat produced can dissipate (Bartlett, Hadden and Bisby, 2019). Subsequently, pyrolysis results in anaerobic conditions, with many of the reactions occurring in a nitrogen atmosphere, promoting the thermal decomposition of aliphatic C-O bonds (Fang *et al.*, 2006). The decrease in peak highlights the breaking of C-O alcohol group bonds from sugars or C-O acid, ester and ether group bonds (Doelsch *et al.*, 2009). Since the 2013 fire is the first high severity fire in the area for approximately the last 30 years, it is likely that the charcoal dispersed throughout the core is from the same fire and would have been subject to the same severity. This could explain the lack of distinguishable trend in the charcoal fraction between charcoal-rich and non-charcoal-rich layers down core. Since the bulk and sand fractions experience a reduction in peak at 1095cm^{-1}, it suggests the occurrence of pyrolysis conditions during the 2013 bushfire.

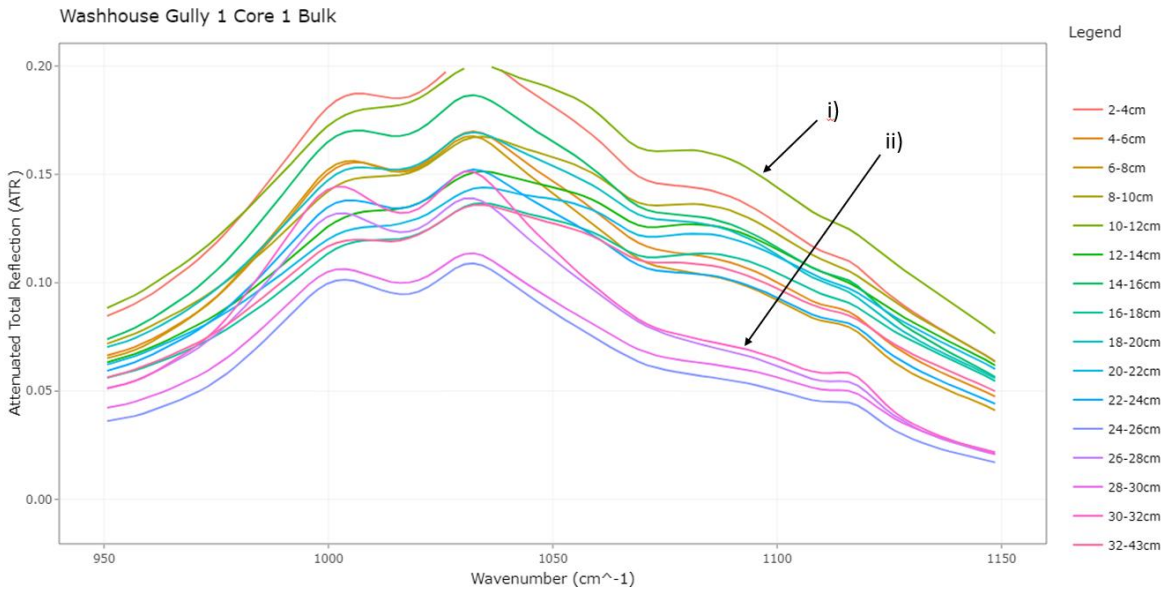

Figure 5.20 Baseline-corrected ATR-FTIR spectra highlighting the band at 1095cm^{-1} for the bulk fraction from Washhouse Gully 1 Core 1. Arrow i) indicates non-charcoal-rich samples (2-24, 32-43cm) and ii) charcoal-rich samples (24-32cm), emphasising the decrease in peak for charcoal-rich samples.

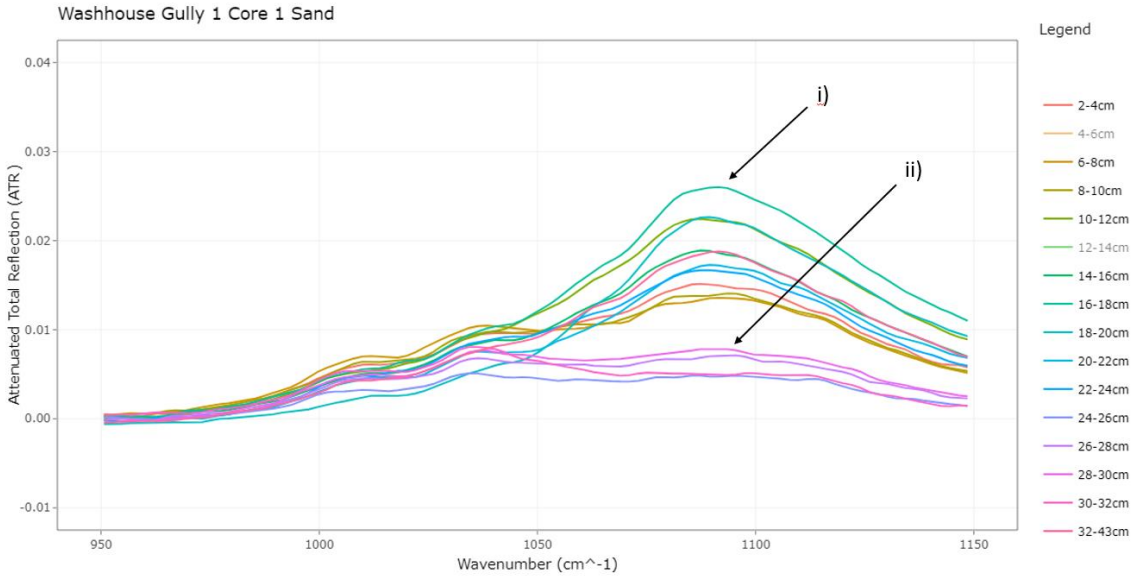

Figure 5.21 Baseline-corrected ATR-FTIR spectra highlighting the band at 1095cm^{-1} for the sand fraction from Washhouse Gully 1 Core 1. Arrow i) indicates non-charcoal-rich samples (2-24, 32-43cm) and ii) charcoal-rich samples (24-32cm), emphasising the decrease in peak for charcoal-rich samples. Sediment collected at 12-14cm depth was not analysed in this band due to poor signal strength.

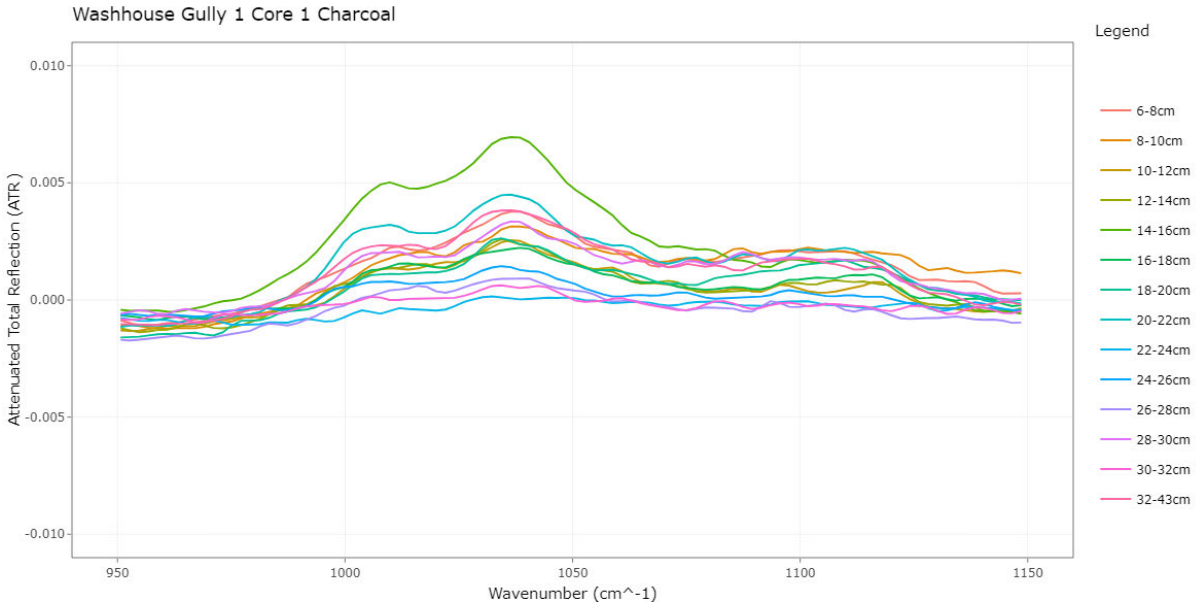

Figure 5.22 Baseline-corrected ATR-FTIR spectra highlighting the band at 1095cm^{-1} for the charcoal fraction from Washhouse Gully 1 Core 1 as a function of depth, emphasising the decrease in peak for all samples in this band.

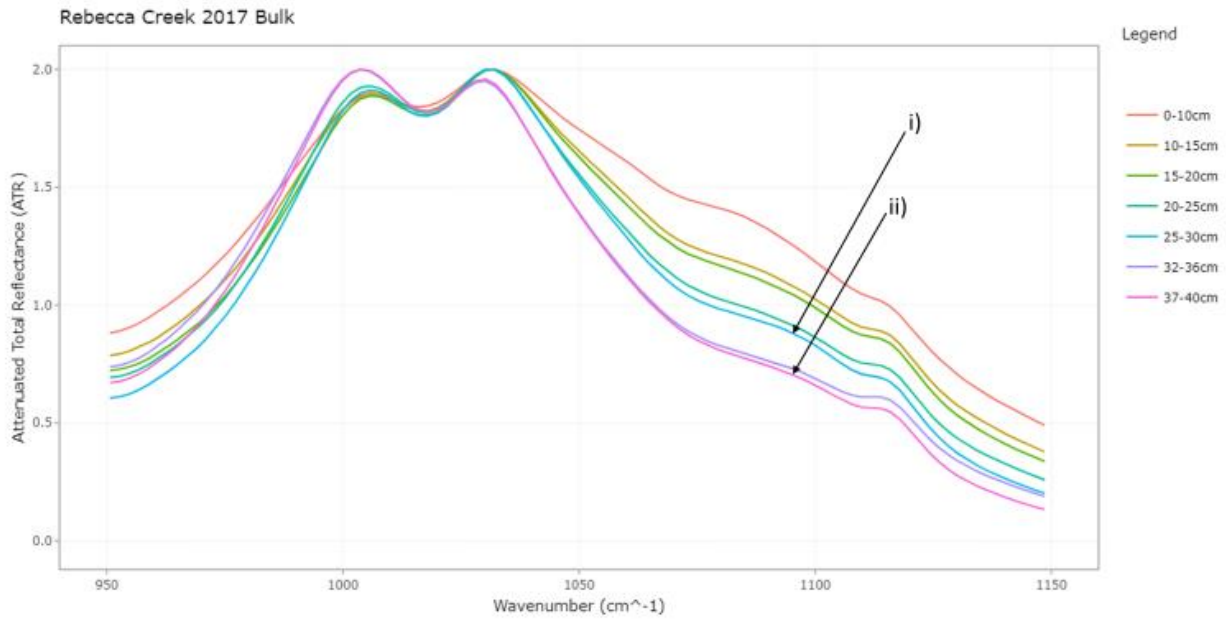

Figure 5.23 Baseline-corrected ATR-FTIR spectra highlighting the band at 1030cm^{-1} for the bulk fraction from the Rebecca Creek 2017 samples. Arrow i) indicates 25-30cm depth and ii) 37-40cm depth, emphasising the decrease in peak intensity for the deeper charcoal-rich layer.

Pyrolysis conditions also affect the bands at 1698cm^{-1} and 1582cm^{-1}. Washhouse Gully 1 Core 1 highlights an increase in peak intensity at 1582cm^{-1} for the bulk fraction (Figure 5.24), and a subsequent reduction at 1698cm^{-1}, as do the samples from Rebecca Creek (Figure 5.25). The charcoal, clay, sand and silt fractions from Washhouse Gully remain at relative background level for all samples. Pyrolysis results in the stretch of the C=O bond in ketones and C=C stretch in aromatic ring structures, resulting in the removal of the peak at 1698cm^{-1} and increase in peak at 1582cm^{-1} respectively (Mastrolonardo *et al.*, 2015). Since Washhouse Gully 1 Core 1 and Rebecca Creek highlight these changes at 1698cm^{-1} and 1582cm^{-1}, this further advocates for the occurrence of pyrolysis conditions during the 2013 bushfire.

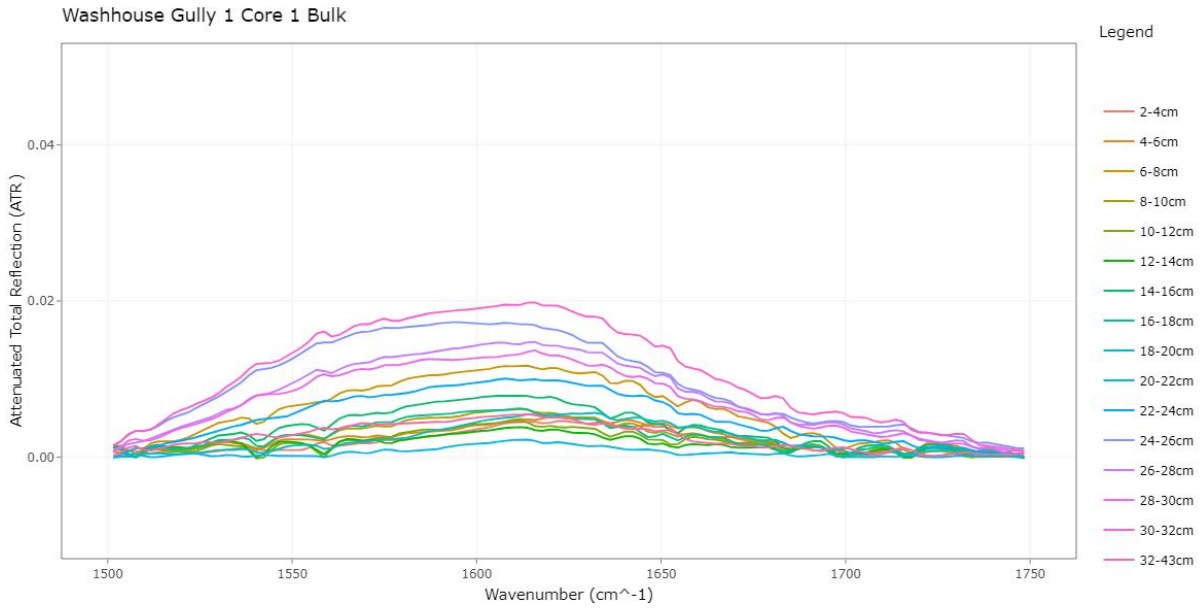

Figure 5.24 Baseline-corrected ATR-FTIR spectra highlighting the bands at 1582 and 1698cm^{-1} for the bulk fraction from Washhouse Gully 1 Core 1 as a function of depth. Charcoal-rich layers have an increased and decreased peak intensity in each of these bands respectively.

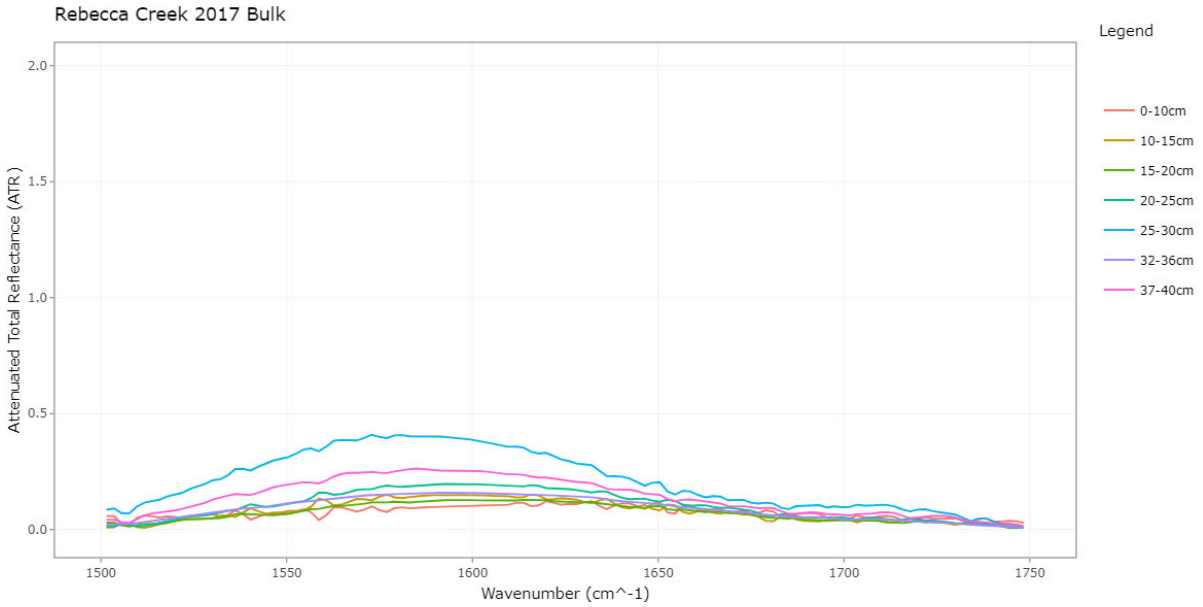

Figure 5.25 Baseline-corrected ATR-FTIR spectra highlighting the bands at 1582 and 1698cm^{-1} for the bulk fraction from Rebecca Creek 2017 samples as a function of depth. Charcoal-rich layers have an increased and decreased peak intensity in each of these bands respectively.

5.4.4 Temperature and Heating Duration

A number of bands in the FTIR spectra reflect temperature and heating duration effects. One such band is that from 900-700cm^{-1} (Guo and Bustin, 1998). The clay, charcoal and silt fractions highlight no significant trend between sample types; however, the bulk and sand fractions indicate an increased peak for non-charcoal rich samples (Figures 5.26 and 5.27). Rebecca Creek highlights a decrease in peak intensity with increasing depth (Figure 5.28). This band varies with charcoal reflectance (Guo and

Bustin, 1998). As temperature and heating duration increase, so too does cell wall reflectance of charcoal (McParland *et al.*, 2009). Charcoal formed at temperatures greater than 400°C yield less C=O groups and experience increased aromatic CH out-of-plane deformation contrasting with charcoals formed at lower temperatures. This results in a more intense peak in the band of 900-700cm^{-1} for temperatures greater than 400°C (Guo and Bustin, 1998). Application to Washhouse Gully 1 Core 1 would suggest that non-charcoal-rich samples (2-24 and 32-43cm) were subject to higher temperatures and/or longer heating duration, proving at odds with other hypotheses presented in this section. Some existing studies have eliminated this region from analysis due to large standard deviations and noise effects (Gosling, Cornelissen and McMichael, 2019).

Temperature gradients are also evident in the region of 800-600cm^{-1} and 1200-900cm^{-1} (Chen *et al.*, 2012). Washhouse Gully 1 Core 1 samples display an increase in peak intensity for non-charcoal-rich samples for the bulk and sand fractions (Figures 5.26 and 5.27). The silt and clay fractions show a less distinct trend with charcoal content (Appendix D.17 and D18). Rebecca Creek also highlights an increase in peak intensity for non-charcoal-rich samples (Figure 5.28). Peak intensity in the bands around 800-600cm^{-1} and 1200-900cm^{-1} are influenced by temperature-resistant Si-O-Si antisymmetric and symmetric stretching respectively, deriving from inorganic minerals (Chen *et al.*, 2012). A more intense peak suggests higher temperatures. This is at odds with other hypotheses presented in this section. Eliminating wavenumbers below 950cm^{-1}, the remaining band from 1200-900cm^{-1} may be explained by the predominance of sand throughout the sediment profile (as supported by grain size analysis for Washhouse Gully). Therefore, the charcoal-rich layer has a greater organic input, possibly reducing the Si-O-Si signal for charcoal-rich samples and increased peak for non-charcoal-rich samples through a bias.

Finally, temperature affects the regions of 1300-1000cm^{-1}. Washhouse Gully 1 Core 1 bulk and sand fractions highlight a decrease in peak intensity for charcoal-rich samples in this band (Figures 5.26 and 5.27). Rebecca Creek shows a decrease in peak with increasing depth (Figure 5.28). This peak reduction arises from changes in C-C, C-N and C-O bonds as a result of exposure to higher temperatures (Chen *et al.*, 2012; Esfandbod *et al.*, 2017; Gosling, Cornelissen and McMichael, 2019). The Washhouse Gully 1 Core 1 bulk fraction also highlights the possibility of exposure to different temperatures within the charcoal-rich layer. Samples from 24-26cm and 28-30cm experience a more significant reduction in peak suggesting exposure to higher temperatures compared with the remaining samples taken from the charcoal-rich layer. Since a fire does not burn homogenously (Kolka *et al.*, 2014), it is possible that there was some temperature variation within the high severity classification. Heterogenous temperature and heating duration could also explain the lack of trend observed in the charcoal

fraction (Figure 5.29). The temperature distinction is not as prominent in the other grain size fractions or for Rebecca Creek.

Peak shifts can also highlight temperature differences such as that from 1631cm^{-1} to 1619cm-^{1} due to increased presence of temperature-resistant aromatics (Simkovic *et al.*, 2008; Mastrolonardo *et al.*, 2014). However, this peak shift is not evident in any of the five fractions analysed for Washhouse Gully 1 Core 1 nor Rebecca Creek, with the spectra not exceeding background in this band. This may be due to masking by the OH bend vibrations of water interactions with phyllosilicate layers (Mastrolonardo *et al.*, 2014). Since all samples were dried for equal duration before analysis, it is possible that dehydration and loss of the OH bonds resulted in this loss of peak shift.

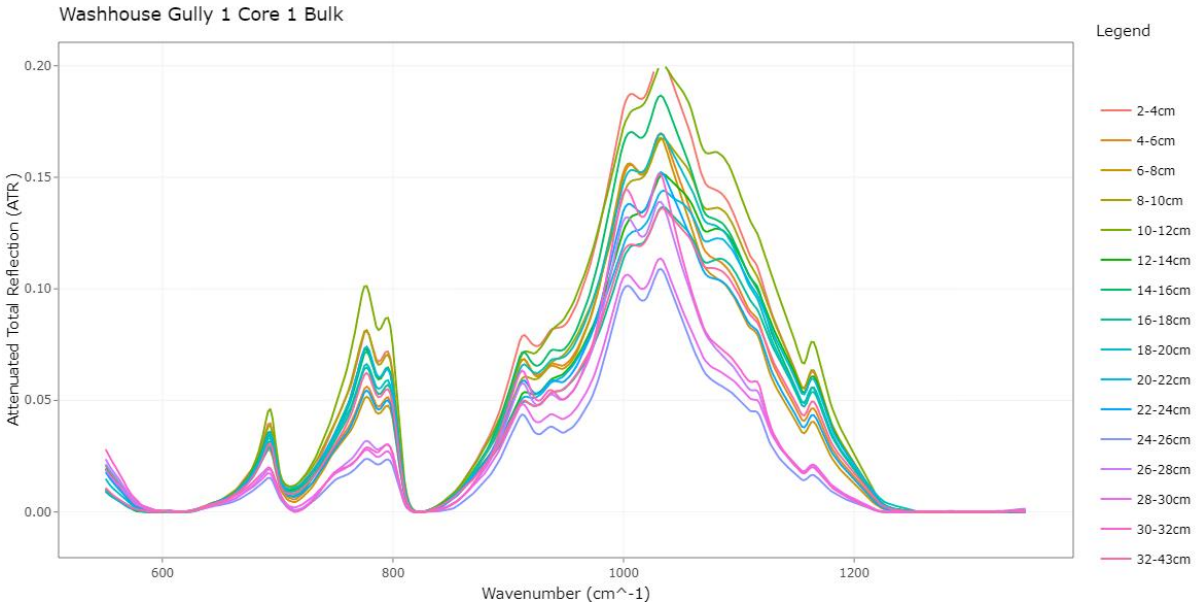

Figure 5.26 Baseline-corrected ATR-FTIR spectra highlighting the bands around 800-600, 900-700 and 1300-1000 cm^{-1} for the bulk fraction from Washhouse Gully 1 Core 1 as a function of depth. Charcoal-rich layers have a reduced peak intensity contrast with non-charcoal-rich samples.

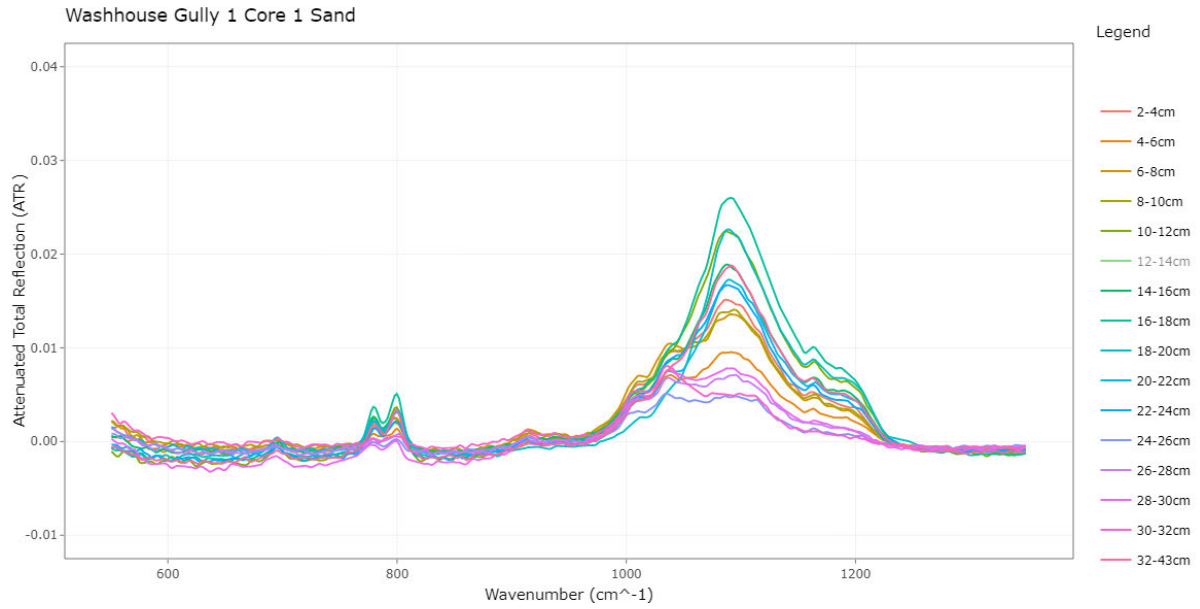

Figure 5.27 Baseline-corrected ATR-FTIR spectra highlighting the bands around 800-600, 900-700 and 1300-1000 cm^{-1} for the sand fraction from Washhouse Gully 1 Core 1 as a function of depth. Charcoal-rich layers have a reduced peak intensity contrast with non-charcoal-rich samples. Sample 12-14cm was not analysed in this band due to poor signal strength.

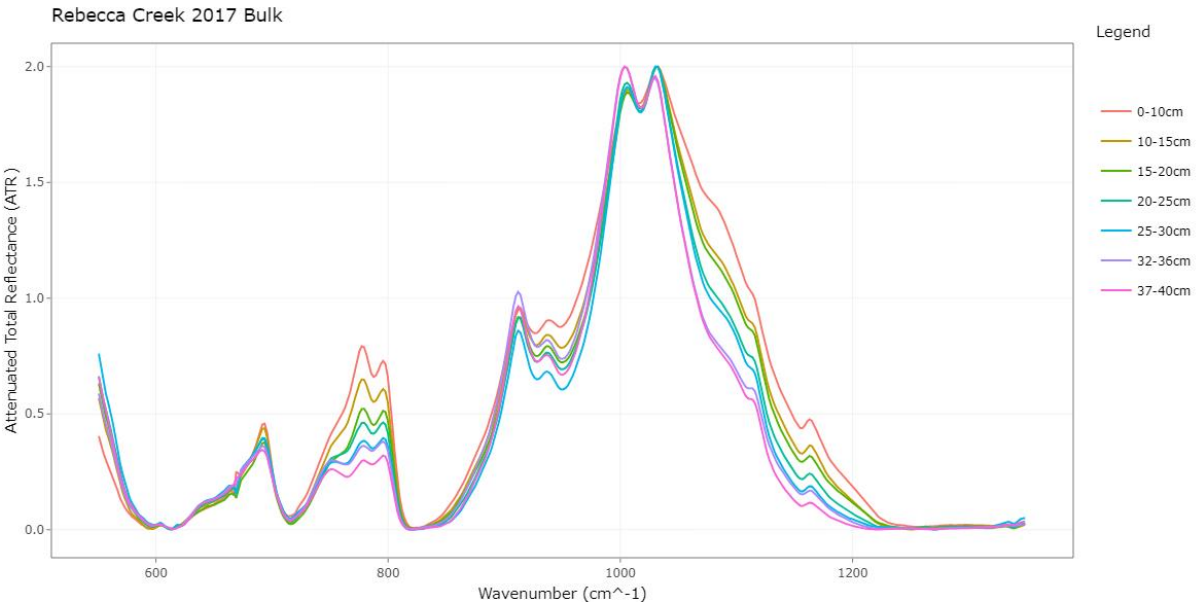

Figure 5.28 Baseline-corrected ATR-FTIR spectra highlighting the bands around 800-600, 900-700 and 1300-1000 cm^{-1} for the bulk fraction from Rebecca Creek as a function of depth. The charcoal-rich layer at 37-40cm depth has a reduced peak intensity contrast with non-charcoal-rich samples.

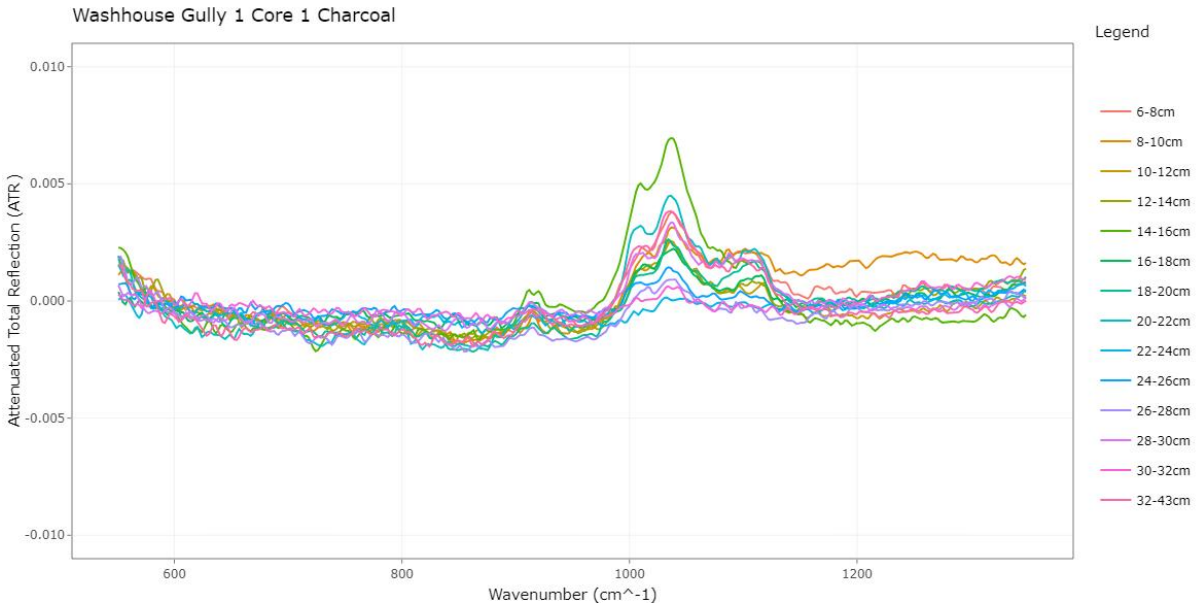

Figure 5.29 Baseline-corrected ATR-FTIR spectra highlighting the bands around 800-600, 900-700 and 1300-1000 cm^{-1} for the sand fraction from Washhouse Gully 1 Core 1 as a function of depth. The lack of a significant trend between samples suggests heterogeneous temperature and heating duration effects.

5.4.5 Methods Comparison: KBr- vs ATR- FTIR

The potassium bromide (KBr) disc method is widely used for the preparation of solid samples for FTIR analysis. The method involves the pressing of a sample into a pellet in the presence of potassium bromide (Madejová and Komadel, 2001). A film can be placed over the sample to prevent the exchange of K into the sample and subsequent alteration of bonds (Madejová and Komadel, 2001). This is in contrast with the ATR method in which total internal reflectance is used to determine the evanescent wave attenuated in various bands of the infrared region. The ATR method requires less sample preparation and is non-destructive, simplifying the FTIR process (Madejová and Komadel, 2001). The complete KBr spectrum for Washhouse Gully 1 Core 1 bulk fraction are presented in Figure 5.30.

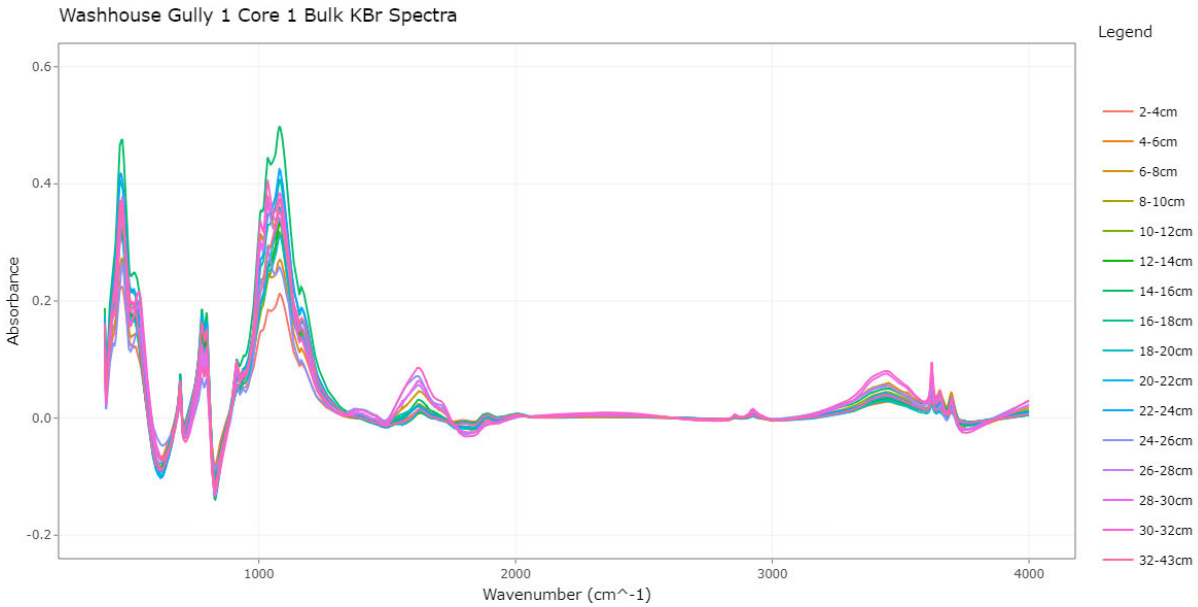

Figure 5.30 Complete KBr-FTIR spectra from 4000 to 400cm^{-1} for Washhouse Gully 1 Core 1 bulk fraction.

Analysis of the peak area ratio of aromatic to aliphatic compounds allows for the determination of charcoal rich samples (Figure 5.31). By taking the ratio of the area under the curve from 3000-2800cm^{-1} to that of 1800-1500cm^{-1} highlights sample 3 (6-8cm) and 12-15 (24-32cm) as charcoal-rich. Sample 3 was not identified as charcoal-rich in the ATR-FTIR spectra.

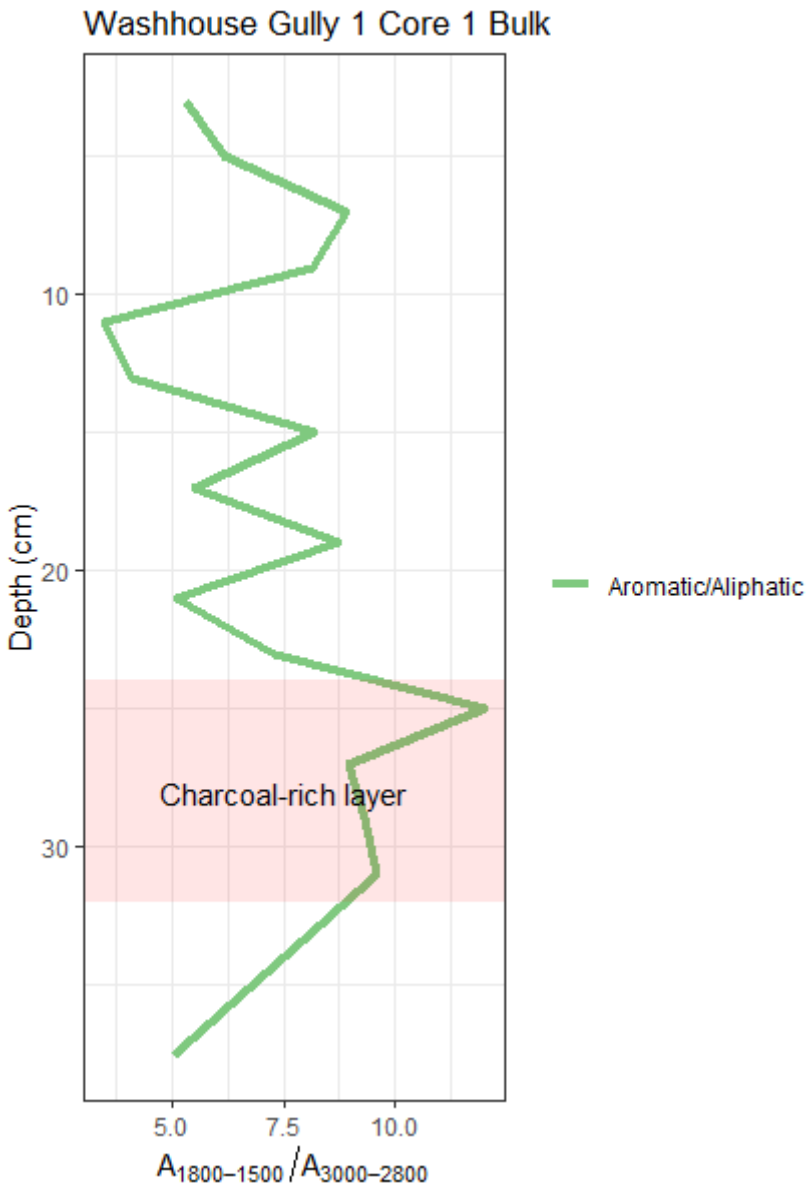

Figure 5.31 Peak area ratio of aromatics ($A_{1800-1500}$)/aliphatics ($A_{3000-2800}$) for the KBr spectra formulated for Washhouse Gully 1 Core 1 as a function of depth.

Some differences exist between the ATR and KBr spectra produced for Washhouse Gully 1 Core 1 bulk samples. The most significant difference in the spectra can be identified in the band at 3400cm^{-1} (Figures 5.32 and Figure 5.33), attributed to the OH bending of water (Simkovic *et al.*, 2008). This band has also been attributed to the deformation and stretching of NH_4^+ vibrations; these bonds typically react with the K^+ in the KBr added to the sample (Madejová and Komadel, 2001). The charcoal-rich samples appear to have the most significant increase in this band. Bushfires can result in an increase in the formation of ammonium nitrate arising from the input of ash into the soil (Bodí *et al.*, 2014), therefore, the KBr spectra suggests a possible increase in NH_4^+ development in the 2013 bushfire that then forms increased NH_4Br absorption bands. Alternatively, since the charcoal-rich samples likely

experience increased dehydration from heating, it is possible that the adsorption capability of charcoal-rich samples is greater than that of non-charcoal rich samples.

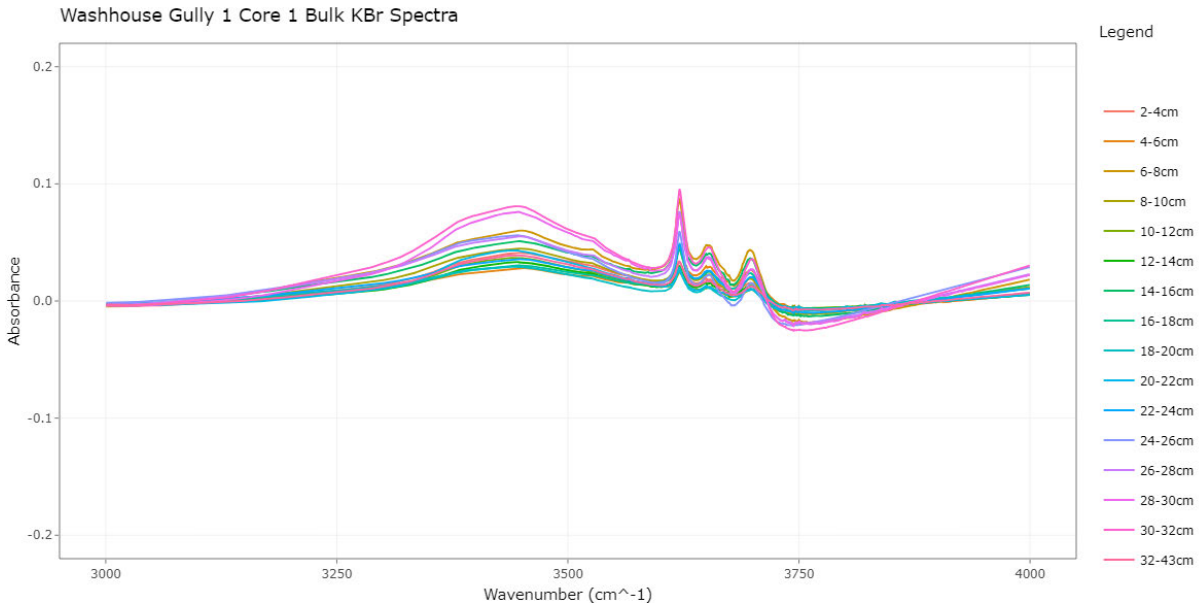

Figure 5.32 Baseline-corrected KBr spectra highlighting the band at 3400cm^{-1} of the bulk fraction for Washhouse Gully 1 Core 1 as a function of depth.

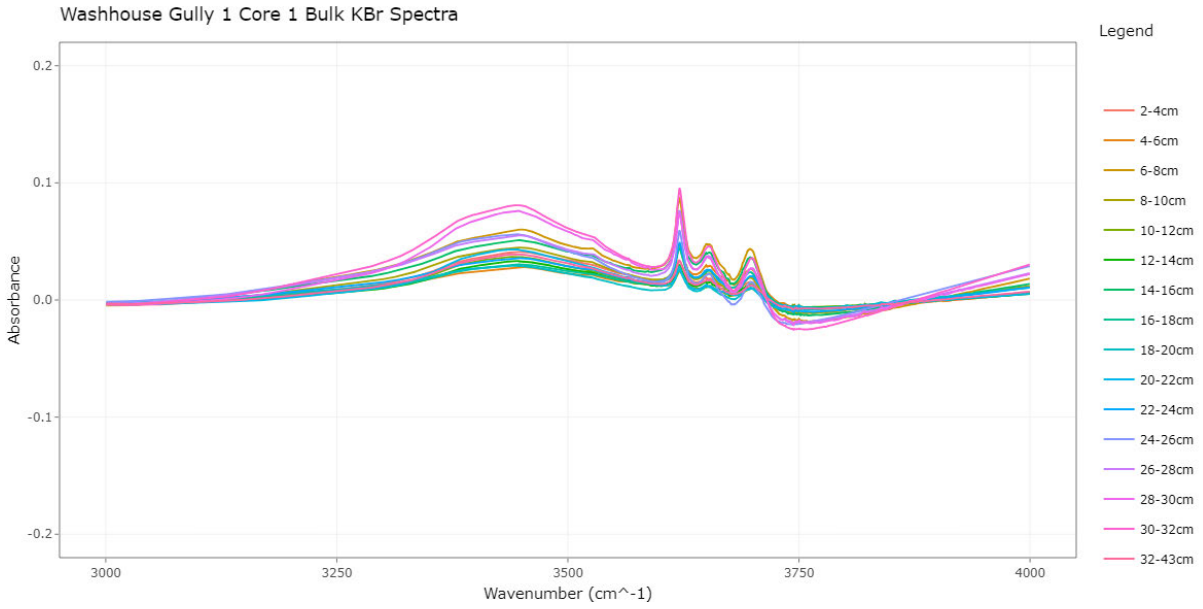

Figure 5.33 Baseline corrected ATR-FTIR spectra highlighting the band at 3400cm^{-1} of the bulk fraction for Washhouse Gully 1 Core 1 as a function of depth.

Several bands emphasise the presence of both quartz and kaolinite. Quartz typically exists as a doublet at approximately 797 and 779cm^{-1} (Dlapa *et al.*, 2013). Si-O bending can also be assigned to the bands at 1084 and 1038cm^{-1} (Sheikh and Barua, 2013). Kaolinite is assigned to a number of the bands in the lower wavenumbers around 915-1100cm^{-1} as well as weak hydroxyl bands around 3700 and 3620cm^{-1} (Sheikh and Barua, 2013). Examination of charcoal-rich contrast with non-charcoal-rich samples

highlights an apparent shift from increased quartz composition to kaolinite composition with fire exposure (Figure 5.34). Kaolinite typically undergoes transformation around 400-600°C where it experiences dihydroxylation and subsequent weakening of the kaolinite bands (Dlapa *et al.*, 2013; Sheikh and Barua, 2013). Heat penetration of the soil is limited to approximately the top 0-5cm depth (Sawyer *et al.*, 2018b), therefore, it is possible that the temperature of the fire had less of an effect on the transformation of kaolinite and mobilisation of finer grain sizes from vegetation loss (Dinis *et al.*, 2020) and an increase in pH result in the observed increase. The production of ash following a high severity fire results in a release of inorganic ions during the first rainfall event post-fire. Kaolinite, like a number of oxide and hydroxide species, varies in charge with pH and electrolyte composition of the soil (Durgin and Vogelsang, 1984). With more alkaline pH, the edges of kaolinite gain increasing negative charge, promoting flocculation and dispersion (Durgin and Vogelsang, 1984). The release of clay comprised of differing charges increases the erodibility of the soil, therefore increasing its mobilisation (Durgin and Vogelsang, 1984) and providing a possible explanation for the increase in kaolinite within the charcoal-rich layer at 24-32cm depth for Washhouse Gully 1 Core 1. Some existing studies, however, have shown that burning reduces clay content and results in a subsequent increase in sand from the formation of aluminosilicates and amorphous Si and Al from the thermal decomposition of kaolinite with heating (Blake *et al.*, 2005).

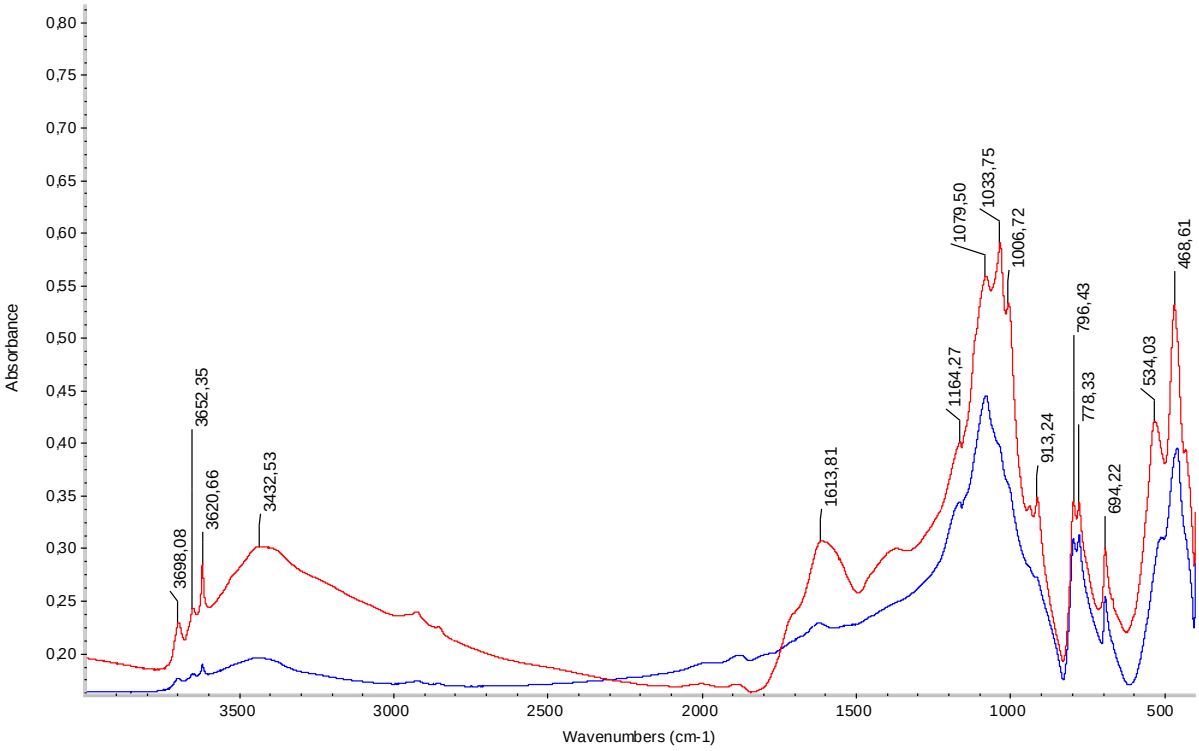

Figure 5.34 Sample 12 (24-26cm) (shown in red) and Sample 16 (32-43cm) (shown in blue) comparison across the spectra with key peaks labelled.

Comparing the KBr spectra for Washhouse Gully 1 Core 1 with the Rebecca Creek samples, there is a gradual decrease in the quartz doublet with depth (Figure 5.35), however, kaolinite also appears to experience a decrease for the uppermost charcoal rich layer. Since this is a depositional environment, a fining upwards succession of grain size would be anticipated as flow intensity decreases (Fisher *et al.*, 2008), however, Rebecca Creek shows a possible degradation of Si-O quartz bonds with depth. This may occur as a result of the slow migration of ripples or a small sand bar with the water current. Typically there is a large amount of forward migration and coarsening upwards succession where there is a greater current speed at the top of ripples and sand bars compared with the trough (Olariu *et al.*, 2012). Since the area is dominated by sand, this could result in the observed trend of increased quartz content towards the surface of the pit.

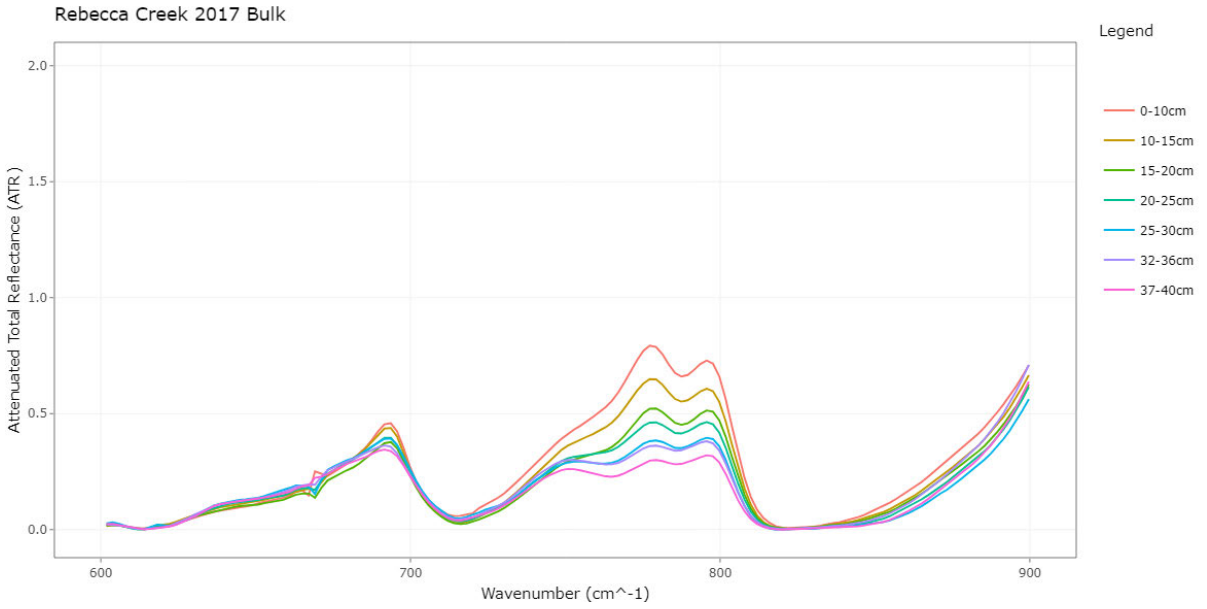

Figure 5.35 Baseline-corrected ATR-FTIR spectra for the 2017 Rebecca Creek samples, highlighting the quartz doublet which decreases with increasing depth.

The bands associated with temperature gradients and type of combustion do not show a clear distinction between charcoal-rich and non-charcoal samples in the KBr spectra when compared with ATR. The ATR spectra highlighted a decrease in the band around 1095cm^{-1} suggesting the effects of anaerobic conditions (Doelsch *et al.*, 2009) and subsequent pyrolysis for the charcoal-rich layers. Whilst the sample collected at 24-26cm depth highlights a decrease in peak in this band, the remaining charcoal-rich samples do not display this trend in the KBr spectra (Figure 5.36). Furthermore, the decreased peak for 2-4cm depth would suggest anaerobic conditions at the surface of the sedimentary sequence. Temperature gradients were also identified in the band around 1300-1000cm^{-1} in the ATR spectra, highlighting a decrease in peak associated with the thermal decomposition of C-C, C-N and C-O bonds (Chen *et al.*, 2012; Esfandbod *et al.*, 2017; Gosling, Cornelissen and McMichael, 2019). This reduction in peak is not shown for any of the charcoal-rich layers despite allowance for small peak

shifts anticipated between the methods. Therefore, analysis by KBr discs alone would suggest no significant temperature or combustion type effects from peak height within the spectra.

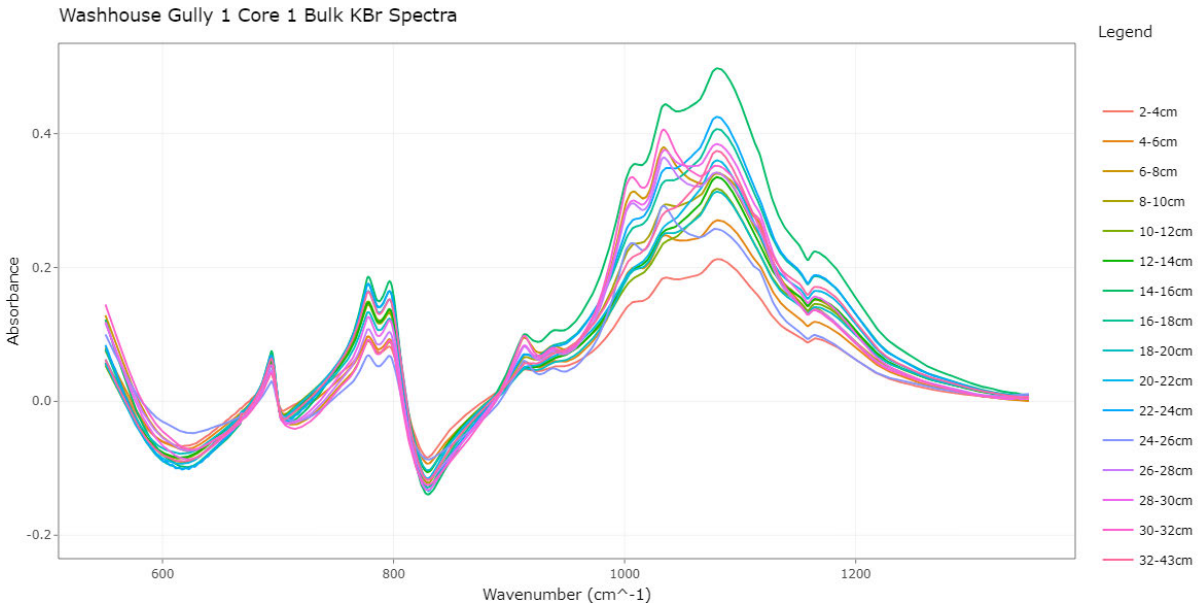

Figure 5.36 Baseline-corrected Washhouse Gully 1 Core 1 KBr bulk spectra highlighting the bands typically associated with temperature gradients between 600 and 1300cm^{-1}.

Comparison of the two techniques- ATR and KBr, highlights advantages for the use of both techniques. The results from the Washhouse Gully 1 Core 1 bulk fraction highlights increased sensitivity of the ATR method in investigating the lower wavenumbers (<1700cm^{-1}), particularly bands associated with the thermal decomposition of aliphatic bonds post-fire. ATR also proves advantageous in terms of reduced sample preparation time. KBr, on the other hand, highlights greater sensitivity to water content and inorganic bonds particularly kaolinite. The use of peak area ratios for both methods proves advantageous in understanding the changes to organic matter content and composition with exposure to bushfire conditions.

5.4.6 FTIR Synthesis

This section aims to summarise the main findings determined using ATR and KBr methods of FTIR.

The most significant changes to the FTIR spectra post-fire were observed in bands associated with organic matter content and biopolymers. The bulk fraction for both Washhouse Gully 1 Core 1 and Rebecca Creek reflected a reduction in cellulose, hemicellulose and lignin bonds following exposure to fire. A reduction was also observed for polysaccharide bonds, highlighting the effects of thermal decomposition and temperature-induced transformations of biopolymers during a fire. Peak area ratios emphasised an increase in both organic matter content and aromatic bonds compared with aliphatic, suggesting exposure to higher temperatures which eliminated aliphatic bonds.

Whilst bonds associated with hydrophobicity typically experience the greatest change in the FTIR spectra following fire, Washhouse Gully 1 Core 1 and Rebecca Creek showed little variation from background in these bands. It was hypothesised that temperatures exceeded that of hydrophobicity effects, resulting in its destruction.

The bulk and sand fractions for Washhouse Gully 1 Core 1 indicated the possible occurrence of pyrolysis conditions during the 2013 bushfire through a reduction in C-O absorption. This was supported by the loss of absorbance associated with stretching vibrations of C=O in ketones and increase in aromatic C=C stretch for the bulk fractions for both creeks, also suggesting pyrolysis conditions. Higher temperatures were also identified by a loss of C-C, C-N and C-O bonds for the fire affected layers in all of the Washhouse Gully 1 Core 1 fractions, with the exception of the clay fraction. Rebecca Creek also suggested a decrease in peak with increasing depth.

Finally, the methods comparison between ATR and KBr highlighted an increased sensitivity of KBr to water and inorganic bonds, specifically that associated with kaolinite. ATR proved advantageous for analysis of the lower wavenumbers as well as thermal decomposition of aliphatic carbon-containing bonds. Advantages were identified for each method, providing encouraging results for their use to determine fire-induced changes to charcoal and the matrix of sediment samples.

5.5 Boron Isotopes

Washhouse Gully 1 Core 1 exhibits a range of $\delta^{11}B$ values from -7.01 (18-20cm) to -1.38‰ (24-26cm). The $\delta^{11}B$ value highlights a general decreasing trend with increasing depth until the surface of the charcoal-rich layer where a peak is evident, marking the start of the 2013 bushfire (Figure 5.37). The boron isotope ratio is expected to decrease with depth as a result of altered influences of atmospheric inputs and biological recycling (Ercolani, Lemarchand and Dosseto, 2019). Atmospheric inputs of boron can include anthropogenic gas emissions, dust deposition and evaporation of seawater, resulting in subsequent entry into the system through rainfall and throughfall (Cividini *et al.*, 2010; Roux *et al.*, 2017). These inputs decrease exponentially with depth and are more significant in coastal environments (Roux *et al.*, 2017; Ercolani, Lemarchand and Dosseto, 2019). Biological recycling, on the other hand, is highest where plant root density is at its maximum and decreases with depth beyond this point (Ercolani, Lemarchand and Dosseto, 2019). Atmospheric inputs and biological recycling of boron result in higher $\delta^{11}B$ values but these impacts are limited to the near-surface. Therefore, clays formed at greater depths have a reduced atmospheric and biological signature, identified by a lower $\delta^{11}B$ value (Ercolani, Lemarchand and Dosseto, 2019).

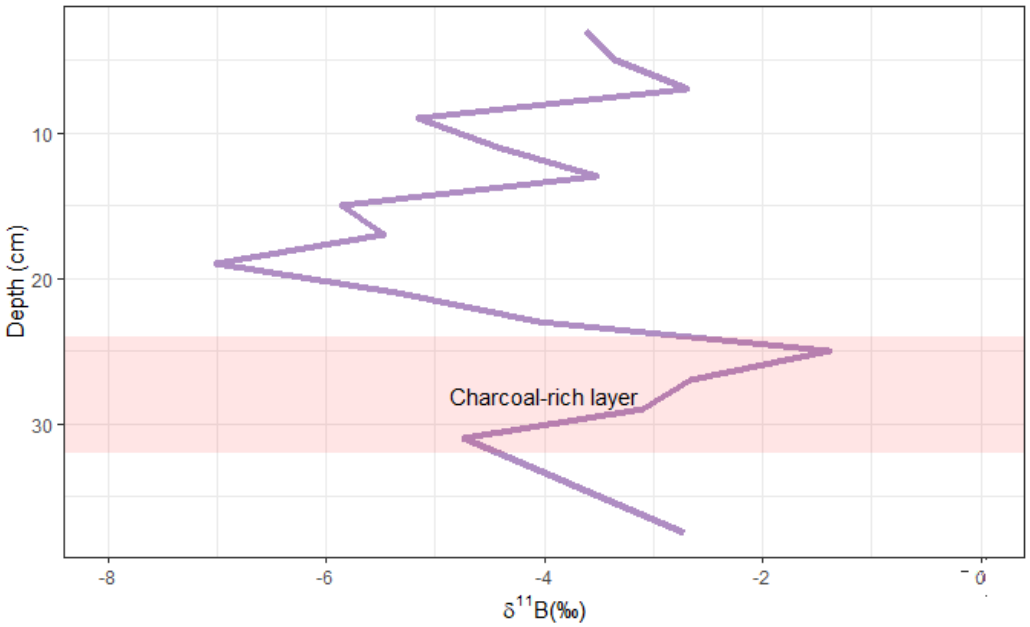

Figure 5.37 Boron isotope results for Washhouse Gully 1 Core 1, highlighting $\delta^{11}B$ variation as a function of depth and in relation to the 2013 fire layer (emphasised by the shaded red rectangle).

The peak in $\delta^{11}B$ value at 24-26cm depth is at odds with the results found by Peltola and Åström (2006) where sediment cores from a lake in Finland highlighted a decrease in $\delta^{11}B$ value associated with the fire affected layer, suggesting an enrichment in ^{10}B. Peltola and Åström (2006) hypothesised that this decrease was the result of increased ash input causing an elevated pH and subsequent increase in tetrahedral coordination, thus producing the enrichment of ^{10}B in clay adsorption (Peltola and Åström, 2006). The alkalinity of the soil increases with fire severity due to changes in the rate of formation of calcium carbonate (Pereira, Úbeda and Martin, 2012). Combustion of wood results in the mineralisation of elements, particularly alkaline metals, to oxides. When exposed to carbon dioxide and moisture in the atmosphere, these oxides undergo various transformations (Etiegni and Campbell, 1991; Pereira, Úbeda and Martin, 2012) Temperature, therefore, influences ash alkalinity (Pereira, Úbeda and Martin, 2012). One possible explanation for the contrasting enrichment in boron isotopes between studies is the methods of sample preparation employed. Peltola and Åström (2006) performed aqua regia digestion prior to ICP-MS analysis, contrast with alkali fusion used for the Washhouse Gully 1 Core 1 samples. Aqua regia primarily extracts boron from the mineral surface, allowing for analysis of the adsorbed minerals on the surface of clays. Alkali fusion, however, extracts boron from the crystal matrix (Vengosh *et al.*, 1991; Gonfiantini *et al.*, 2003), allowing for analysis of structural boron. Since adsorbed boron experiences greater fractionation as a result of higher alkalinity, this provides a possible explanation for the enrichment in ^{10}B determined by Peltola and Åström (2006) that was not seen for Washhouse Gully.

Several studies have shown an enrichment of ^{11}B in plant leaves compared with soil which, following fire events of various severities, could alter the contribution of ^{11}B enriched organic material to the surface soil (Marentes, Vanderpool and Shelp, 1997; Geilert *et al.*, 2015; Xu *et al.*, 2015). Low severity fire typically deposit a highly decomposition-resistant layer of heat-affected leaves and twigs to the surface soil, contrast with high severity fires in which mineralised ash is deposited (Sawyer *et al.*, 2018a). Therefore, during high severity fires, ash consists of higher proportions of combusted leaves from tree canopies, resulting in increased input of ^{11}B to the surface soil. Following rainfall, ash enriched in ^{11}B is then leached into the sediment profile, resulting in higher substitution and formation of clays enriched in the heavier isotope (Lehto, Ruuhola and Dell, 2010; Sun *et al.*, 2019). This could suggest a possible cause for the elevated $\delta^{11}B$ value seen at the surface of the charcoal-rich layer for Washhouse Gully 1 Core 1. The decline in peak for the remainder of the charcoal layer could be the result of a grain size gradient since the surface of the charcoal-rich layer was also marked by an increase in finer grain sizes and a reduction in sand. Since organics are typically fine-grained, particularly following complete combustion to ash, there may be a depositional gradient of ash and subsequent availability of ^{11}B for leaching and substitution.

Transformations of borate and boric acid under various temperatures could result in the increase in the $\delta^{11}B$ value at the surface of the charcoal-rich layer, diminishing the pH effects, which largely altered the adsorbed boron. When exposed to increasing temperatures, borate liquids dissociate into symmetric BO_{3S} species and non-bridging oxygen (NBO)(Equation 3) (Sen, Xu and Stebbins, 1998). This increases the proportion of boric acid at higher temperatures.

$$BO_4 \rightleftharpoons BO_{3S} + NBO \quad (3)$$

At temperatures above 80°C, boric acid begins to be transformed, forming metaboric acid at approximately 130°C (Balci, Sezgi and Eren, 2012). With a continuous increase in temperature, boron behaves like a metal, allowing the formation of boron oxide. This reaction slows when temperatures exceed 450°C (Balci, Sezgi and Eren, 2012). Boron oxide more readily reacts with silicates to form temperature-resistant borosilicate minerals. Washhouse Gully 1 Core 1 is largely composed of quartz sandstone, providing an abundant supply of silica for this reaction. Borosilicates that are exposed to increasing temperatures, experience fractionation, causing a significant reduction in the tetrahedral species due to formation of non-bridging oxygen (Stebbins and Ellsworth, 1996; Sen, Xu and Stebbins, 1998). Subsequently, the trigonal species, $B(OH)_3$, which is has a greater affinity for ^{11}B (Lemarchand, Schott and Gaillardet, 2005; Sun *et al.*, 2019), is enriched, thus providing a possible explanation for the increase in $\delta^{11}B$ value at the start of the charcoal layer. Aside from this peak at 24-26cm depth, the remainder of the charcoal-rich layer experiences a reduced peak. When boron oxide reacts with

the environment and bonds with hydrogen, boric acid is reformed. Since these layers would have been deposited first, it is possible that the remainder of the charcoal layer was exposed to the environment and rehydrated prior to formation of borosilicates, therefore experiencing less fractionation and subsequent enrichment in ^{11}B when compared with the layer at 24-26cm depth (Figure 5.38). The decrease in peak does not display the same reduction in $\delta^{11}B$ values experienced in the layers above the charcoal-rich layers. This suggests that there is still some loss of the tetrahedral species in the remainder of the charcoal-rich layers.

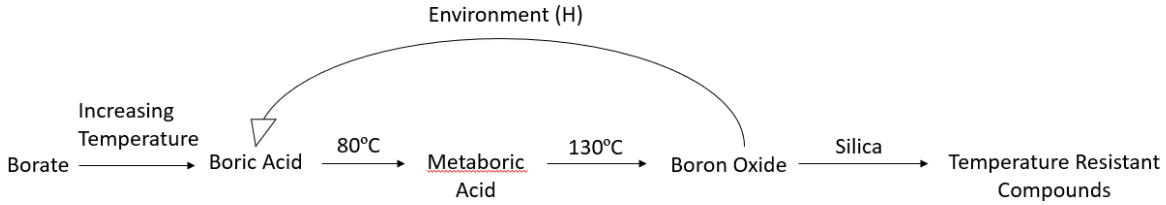

Figure 5.38 Flow diagram for the transformation of borate and boric acid with temperature.

The speciation of boron with temperature is confirmed in the FTIR spectra. The trigonal species, boric acid, is defined by a clear band at 1400cm^{-1} as a result of B-O stretching, whilst borate is defined by the band at 950cm^{-1}. An overlapping band at 1150cm^{-1}, associated with B-O-H bending, is characteristic of both species (Peak, Luther and Sparks, 2003). The highest $\delta^{11}B$ value and hypothesised boric acid enrichment is assigned to 24-26cm. Comparing this to a non-charcoal rich sample at 32-43cm depth, there is a distinct increase in the band at approximately 1400cm^{-1} for 24-26cm in both the KBr and ATR spectra (Figures 5.39 and 5.40). This increase is also evident to a lesser degree in each of the charcoal-rich samples. The increase in boric acid in the FTIR spectra has been linked to pH, with the shift to borate requiring pH greater than 11.5 (Peak, Luther and Sparks, 2003). Nuclear Magnetic Resonance (NMR) has been typically used to highlight the temperature-induced loss of the borate peak (Stebbins and Ellsworth, 1996; Sen, Xu and Stebbins, 1998), also highlighting a possible speciation effect as a result of temperature.

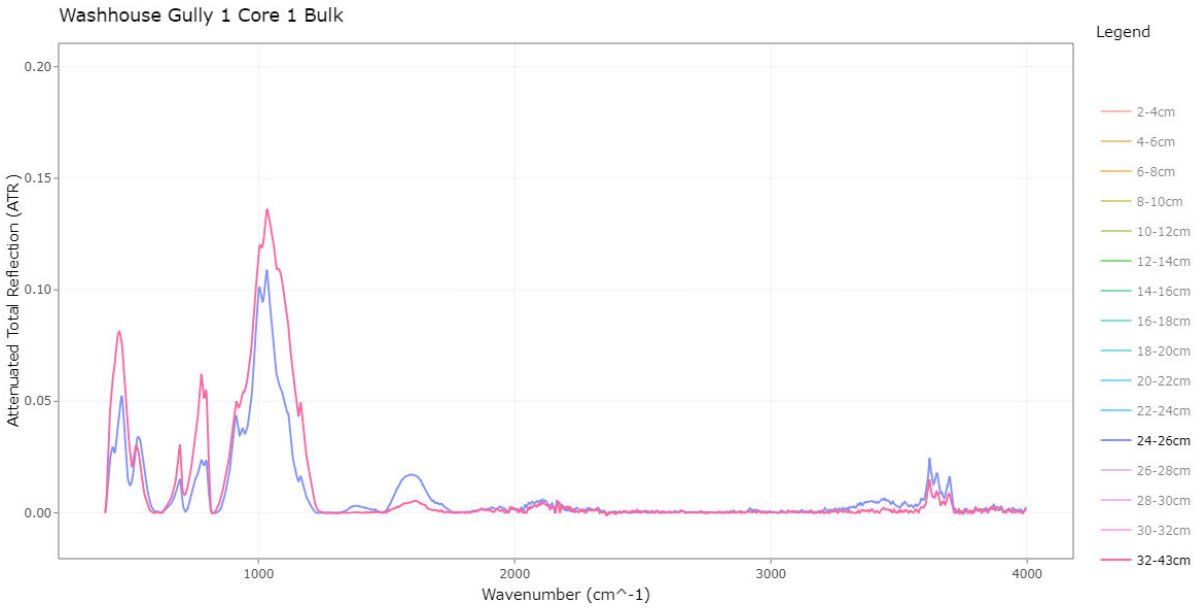

Figure 5.39 Baseline-corrected ATR-FTIR spectra for 24-26cm and 32-43cm depth, highlighting the increase in peak intensity for the sediment at 24-26cm depth (purple) for the band around 1400cm^{-1} associated with boric acid enrichment.

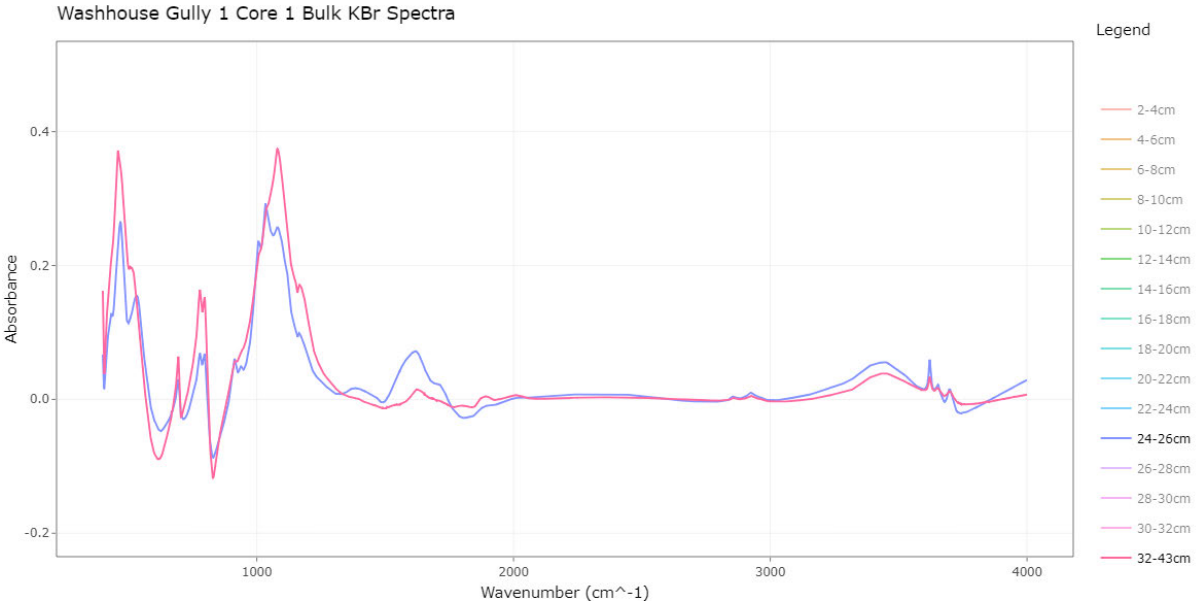

Figure 5.40 Baseline-corrected KBr-FTIR spectra for 24-26cm and 32-43cm depth, highlighting the increase in peak intensity for the sediment at 24-26cm depth (purple) for the band around 1400cm^{-1} associated with boric acid enrichment.

Comparing the boron isotope results for Washhouse Gully 1 Core 1 with Rebecca Creek, the $\delta^{11}B$ values range from -2.92 (15-20cm) to -0.05‰ (25-30cm). An increase in the $\delta^{11}B$ value is also experienced for the upper-most charcoal-rich layer (25-30cm), however, the second charcoal-rich layer (37-40cm) does not highlight the same peak (Figure 5.41). It is possible that the sediment transportation rates between the two creeks differ, therefore resulting in two charcoal-rich layers for Rebecca Creek. The lower-most charcoal layer at 37-40cm depth may represent the *in situ* effects of the fire and may be largely dominated by macrocharcoals due to mobilisation of ash and

microcharcoals downstream during the first rainfall event post-fire. The second charcoal-rich layer at 25-30cm potentially formed in a later rainfall event where transported microcharcoals and ash from upstream were deposited, therefore creating an appearance of a possible temperature difference.

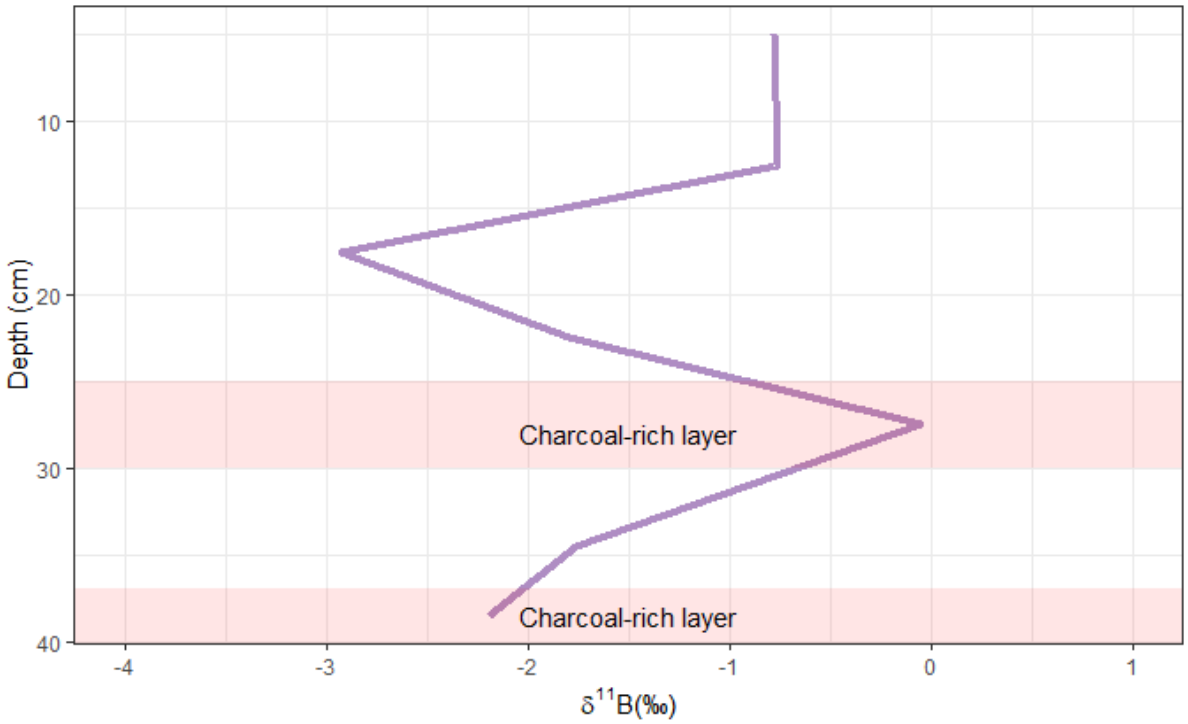

Figure 5.41 Boron isotope results highlighting changes in $\delta^{11}B$ as a function of depth and in relation to the 2013 fire charcoal layers (emphasised by the shaded red rectangles) for Rebecca Creek 2017 samples.

6 Future Developments, Limitations and Conclusions

6.1 Conclusions

The aim of this project was to calibrate boron isotopes and FTIR against known fire occurrence in the Upper Nepean catchment to determine their suitability as proxies. Existing methods for reconstructing past fire records, total carbon and nitrogen analysis and radiocarbon dating, were also analysed to determine advantages and advances of the use of these novel techniques. Through analysis of the changes in $\delta^{11}B$ value and molecular composition of Washhouse Gully 1 Core 1 and Rebecca Creek, the following conclusions were formulated:

- Total carbon and nitrogen analysis highlighted anomalies in nitrogen concentration within the charcoal-rich layers that had flow-on effects in the success of the C/N ratio as a proxy for determining past fire occurrence. Radiocarbon ages for Rebecca Creek highlighted some analytical error and subsequent age discrepancy as the charcoal was less than 100 years old. The severity of the 2013 fire was also indeterminant from these two proxies.
- Analysis of the FTIR spectra produced for the five fractions of Washhouse Gully 1 Core 1 highlighted exposure to higher temperatures and pyrolysis conditions in the charcoal-rich layer associated with the 2013 bushfire compared with the remainder of the core. The bulk fraction also exhibited a significant transition from aliphatic to aromatic dominance as well as an increase in kaolinite in the charcoal-rich layers. Comparison with Rebecca Creek highlighted larger variation between the two charcoal-rich layers, however, a possible temperature gradient is still evident.
- Analysis of the boron isotope results for both Washhouse Gully 1 Core 1 and Rebecca Creek highlight an enrichment in the heavier isotope ^{11}B, causing an increase in the $\delta^{11}B$ value for the fire affected layers. This is suggested to result from either the deposition of ash enriched in the heavier isotope or the possible temperature-induced transformations of boric acid, resulting in subsequent speciation of boron. This speciation was also substantiated in the FTIR spectra providing encouraging results for the success of boron isotopes as a proxy for determining past fire.

6.2 Limitations and Future Directions

Some limiting factors were experienced over the course of this study requiring further analysis and contemplation in future studies of both boron isotopes and FTIR spectroscopy to determine past fire. These are outlined as follows:

- High noise effects and low signal strength were encountered throughout analysis of samples, leading to some difficulties in analysis of the higher wavenumbers. It is recommended that future research targets re-evaluation to remove these effects and improve accuracy.
- Since some variation is observed between the $\delta^{11}B$ values between charcoal layers for Rebecca Creek, it is advised that further analysis is conducted to determine the effects of overprinting between fire events. This could be extended to analyse older fire events to determine whether time since last fire affects the boron isotope ratio.
- In this study, detailed analysis was limited to one core. Increasing the number of cores analysed along the creek would allow for greater investigation into signal transport. This is beyond the scope of this study, however, is recommended as an area for future research.
- This study calibrated two new proxies, boron isotopes and FTIR, in sediment samples known to have experienced a high severity fire. Since the two proxies were successful in producing a signature to identify high severity, further analysis targeting low to moderate severity fire events, including the effects of cultural burning, is recommended to investigate the ability of the proxies to distinguish between the severity and intensity of events.

7 References

Abakumov, E., Maksimova, E. and Tsibart, A. (2018) 'Assessment of postfire soils degradation dynamics : Stability and molecular composition of humic acids with use of spectroscopy methods', *Land Degrad Dev.*, (29), pp. 2092–2101. doi: 10.1002/ldr.2872.

Alcañiz, M. *et al.* (2018) 'Effects of prescribed fires on soil properties: A review', *Science of the Total Environment*. Elsevier B.V., 613–614, pp. 944–957. doi: 10.1016/j.scitotenv.2017.09.144.

Almendros, G., Martin, F. and Gonzalez-Vila, F. J. (1988) 'Effects of Fire on Humic and Lipid Fractions in a Dystric Xerochrept in Spain', *Geoderma*, 42, pp. 115–127.

Balci, S., Sezgi, N. A. and Eren, E. (2012) 'Boron oxide production kinetics using boric acid as raw material', *Industrial and Engineering Chemistry Research*, 51(34), pp. 11091–11096. doi: 10.1021/ie300685x.

Bartlett, A. I., Hadden, R. M. and Bisby, L. A. (2019) 'A Review of Factors Affecting the Burning Behaviour of Wood for Application to Tall Timber Construction', *Fire Technology*. Springer US, 55(1), pp. 1–49. doi: 10.1007/s10694-018-0787-y.

Bento-Gonçalves, A. *et al.* (2012) 'Fire and soils: Key concepts and recent advances', *Geoderma*. Elsevier B.V., 191, pp. 3–13. doi: 10.1016/j.geoderma.2012.01.004.

Bigio, E. R., Swetnam, T. W. and Pearthree, P. A. (2017) 'Late Holocene fire – climate relationships of the western San Juan Mountains , Colorado', *International Journal of Wildland Fire*, 26, pp. 944–962.

Black, M. P., Mooney, S. D. and Haberle, S. G. (2007) 'The fire, human and climate nexus in the Sydney Basin, eastern Australia', *Holocene*, 17(4), pp. 469–480. doi: 10.1177/0959683607077024.

Blake, W. H. *et al.* (2005) 'Impacts of wildfire on effective sediment particle size : implications for post-fire sediment budgets', *Sediment Budgets*, 1(April), pp. 143–150.

Bodí, M. B. *et al.* (2014) 'Wildland fire ash: Production, composition and eco-hydro-geomorphic effects', *Earth Science Reviews*. Elsevier B.V., 130, pp. 103–127. doi: 10.1016/j.earscirev.2013.12.007.

Bordy, E. M. *et al.* (2018) 'A Holocene "Frozen Accident": Sediments of Extreme Paleofloods and Fires in the Bedrock-Confined Upper Huis River, Western Cape, South Africa', *Journal of Sedimentary Research*, 88(June), pp. 696–716.

Bradstock, R. *et al.* (2014) 'Divergent responses of fire to recent warming and drying across south-eastern Australia', *Global Change Biology*, 20, pp. 1412–1428. doi: 10.1111/gcb.12449.

Bradstock, R. A. (2010) 'A biogeographic model of fire regimes in Australia: Current and future implications', *Global Ecology and Biogeography*, 19(2), pp. 145–158. doi: 10.1111/j.1466-8238.2009.00512.x.

Bureau of Meteorology (2014) *New South Wales in 2013*. Available at: http://www.bom.gov.au/climate/current/annual/nsw/archive/2013.summary.shtml (Accessed: 11 June 2020).

Bureau of Meteorology (2015) *New South Wales in 2014*. Available at: http://www.bom.gov.au/climate/current/annual/nsw/archive/2014.summary.shtml (Accessed: 11 June 2020).

Bureau of Meteorology (no date) *Daily Rainfall graph - 068166 - Bureau of Meteorology*. Available at: http://www.bom.gov.au/jsp/ncc/cdio/weatherData/av?p_display_type=dataDGraph&p_stn_num=068166&p_nccObsCode=136&p_month=13&p_startYear=2014 (Accessed: 22 June 2020).

Cadd, H. R. *et al.* (2020) 'The potential for rapid determination of charcoal from wetland sediments using infrared spectroscopy', *Palaeogeography, Palaeoclimatology, Palaeoecology*, 542(October 2019). doi: 10.1016/j.palaeo.2019.109562.

Certini, G. (2005) 'Effects of fire on properties of forest soils: A review', *Oecologia*, 143(1), pp. 1–10. doi: 10.1007/s00442-004-1788-8.

Chen, K. Y. *et al.* (2012) 'Chromate removal as influenced by the structural changes of soil components upon carbonization at different temperatures', *Environmental Pollution*. Elsevier Ltd, 162, pp. 151–158. doi: 10.1016/j.envpol.2011.10.036.

Chetelat, B. *et al.* (2009) 'Boron isotopes geochemistry of the Changjiang basin rivers', *Geochimica et Cosmochimica Acta*, 73(20), pp. 6084–6097. Available at: internal-pdf://0383823587/1-s2.0-S0016703709004815-main.pdf.

Cividini, D. *et al.* (2010) 'From biological to lithological control of the B geochemical cycle in a forest watershed (Strengbach , Vosges)', *Geochimica et Cosmochimica Acta*. Elsevier Ltd, 74(11), pp. 3143–3163. doi: 10.1016/j.gca.2010.03.002.

Department of Environment and Heritage, T. (2017) *Draft Plan of Management Upper Nepean State Conservation Area*.

Dibiase, R. A. *et al.* (2017) 'Journal of Geophysical Research : Earth Surface', *Journal of Geophysical Research: Earth Surface*, 122, pp. 941–960. doi: 10.1002/2016JF003970.

Dinis, P. A. *et al.* (2020) 'Applied Clay Science Post-wild fire denudation assessed from compositional features of river sediments (Central Portugal)', *Applied Clay Science*. Elsevier, 193(May), p. 105675. doi: 10.1016/j.clay.2020.105675.

Dlapa, P. *et al.* (2013) 'FT-IR spectroscopy reveals that ash water repellency is highly dependent on ash chemical composition', *Catena*. Elsevier B.V., 108, pp. 35–43. doi: 10.1016/j.catena.2012.02.011.

Doelsch, E. *et al.* (2009) 'Spectroscopic characterization of organic matter of a soil and vinasse mixture during aerobic or anaerobic incubation', *Waste Management*. Elsevier Ltd, 29(6), pp. 1929–1935. doi: 10.1016/j.wasman.2008.12.009.

Doerr, S. H. *et al.* (2014) *Water contamination threat from bushfire ash : the Balmoral bushfire , October 2013*.

Durgin, P. B. and Vogelsang, P. J. (1984) 'Dispersion of Kaolinite by Water Extracts of Douglas-Fir Ash', *Canadian Journal or Soil Science*, 439, pp. 439–443.

Earl, N. and Simmonds, I. (2017) 'Variability, trends, and drivers of regional fluctuations in Australian fire activity', *Journal of Geophysical Research*, 122(14), pp. 7445–7460. doi: 10.1002/2016JD026312.

Eaton, B. C. *et al.* (2010) 'Geomorphology Wildfire , morphologic change and bed material transport at Fishtrap Creek , British Columbia', *Geomorphology*. Elsevier B.V., 118(3–4), pp. 409–424. doi: 10.1016/j.geomorph.2010.02.008.

Ercolani, C., Lemarchand, D. and Dosseto, A. (2019) 'Insights on catchment-wide weathering regimes from boron isotopes in riverine material', *Geochimica et Cosmochimica Acta*. Elsevier Ltd, 261, pp. 35–55. doi: 10.1016/j.gca.2019.07.002.

Esfandbod, M. *et al.* (2017) 'Role of oxygen-containing functional groups in forest fire-generated and pyrolytic chars for immobilization of copper and nickel', *Environmental Pollution*. Elsevier Ltd, 220, pp. 946–954. doi: 10.1016/j.envpol.2016.10.080.

Etiegni, L. and Campbell, A. G. (1991) 'Physical and Chemical Characteristics of Wood Ash', *Bioresource technology*, 37(July 1990), pp. 173–178.

Fang, M. X. *et al.* (2006) 'Kinetic study on pyrolysis and combustion of wood under different oxygen concentrations by using TG-FTIR analysis', *Journal of Analytical and Applied Pyrolysis*, 77(1), pp. 22–27. doi: 10.1016/j.jaap.2005.12.010.

Fisher, J. A. *et al.* (2008) 'Sedimentology and architecture of the Douglas Creek terminal splay , Lake Eyre , central Australia', *Sedimentology*, pp. 1915–1930. doi: 10.1111/j.1365-3091.2008.00974.x.

Florsheim, J. L. *et al.* (2016) 'Geomorphology Short-term post-wild fire dry-ravel processes in a chaparral fluvial system', *Geomorphology*, 252, pp. 32–39. doi: 10.1016/j.geomorph.2015.03.035.

Gaillardet, J. and Lemarchand, D. (2009) 'Boron in the Weathering Environment', in *Boron Isotopes*, pp. 1–26.

Gangjian, W. *et al.* (2013) 'Measurement on high-precision boron isotope of silicate materials by a single column purification', *J. Anal. At. Spectrom*, 28, pp. 606–612. doi: 10.1039/c3ja30333k.

Geilert, S. *et al.* (2015) 'Mass Spectrometry & Purification Techniques Boron Isotope Fractionation in Bell Pepper', *Mass Spectrometry & Purification Techniques*, 1(1), pp. 1–6. doi: 10.4172/mso.1000101.

Gillespie, R. *et al.* (1992) 'AMS Dating of Alluvial Sediments on the Southern Tablelands of New South Wales, Australia', *Radiocarbon*, 34(1), pp. 29–36.

Goldberg, S. (1997) 'Reactions of boron with soils', *Plant and Soil*, 193, pp. 35–48.

Gonfiantini, R. *et al.* (2003) 'Intercomparison of Boron Isotope and Concentration Measurements . Part II : Evaluation of Results', *The Journal of Geostandards and Geoanalysis*, 27(1), pp. 41–57.

Gonfiantini, R. and Pennisi, M. (2006) 'The behaviour of boron isotopes in natural waters and in water–rock interactions', *Journal of Geochemical Exploration*, 88(1), pp. 114–117.

González-pérez, J. A. *et al.* (2008) 'Organic Geochemistry Use of multiple biogeochemical parameters to monitor the recovery of soils after forest fires', *Organic Geochemistry*, 39, pp. 940–944. doi: 10.1016/j.orggeochem.2008.03.014.

Gordon, V. (2017) 'Historic Heritage Assessment and Aboriginal Cultural Heritage Assessment', 2(November).

Gosling, W. D., Cornelissen, H. L. and McMichael, C. N. H. (2019) 'Reconstructing past fire temperatures from ancient charcoal material', *Palaeogeography, Palaeoclimatology, Palaeoecology*. Elsevier, 520(March 2018), pp. 128–137. doi: 10.1016/j.palaeo.2019.01.029.

Guo, Y. and Bustin, R. M. (1998) 'FTIR spectroscopy and reflectance of modern charcoals and fungal decayed woods : implications for studies of inertinite in coals', *International Journal of Coal Geology*, 37, pp. 29–53.

Hahn, A. *et al.* (2018) 'Using Fourier transform infrared spectroscopy to determine mineral phases in sediments', *Sedimentary Geology*. Elsevier B.V., 375, pp. 27–35. doi: 10.1016/j.sedgeo.2018.03.010.

Haworth, R. J. (2003) 'The shaping of Sydney by its urban geology', *Quarternary International*, 103, pp.

41–55.

Heath, J. T. *et al.* (2016) ‘Post-Fire Recovery of Eucalypt-Dominated Vegetation Communities in the Sydney Basin, Australia’, *Fire Ecology*, 12(3), pp. 53–79. doi: 10.4996/fireecology.1203053.

Hua, Q., Barbetti, M. and Rakowski, A. Z. (2013) ‘Atmospheric radiocarbon for the period 1950–2010’, *Radiocarbon*, 55(4), pp. 2059–2072.

Jull, A. J. T. and Geertsema, M. (2006) ‘Over 16,000 Years of Fire Frequency Determined from AMS Radiocarbon Dating of Soil Charcoal in an Alluvial Fan at Bear Flat, Northeastern British Columbia’, *Radiocarbon*, 48(3), pp. 435–450.

Kennedy, L. M., Tech, V. and Horn, S. P. (2008) ‘A Late Holocene Pollen and Charcoal Record from La Selva Biological Station , Costa Rica’, *Biotropica*, 40(1), pp. 11–19.

Kharaka, Y. K. and Hanor, J. S. (2003) ‘Deep Fluids in the Continents: I. Sedimentary Basins’, *Treatise on Geochemistry*, 5–9, pp. 1–48. doi: 10.1016/B0-08-043751-6/05085-4.

Kolka, R. *et al.* (2014) ‘Post-Fire Comparisons of Forest Floor and Soil Carbon, Nitrogen, and Mercury Pools with Fire Severity Indices’, *Northern American Forest Soils Conference Proceedings*. doi: 10.2136/sssaj2013.08.0351nafsc.

Krebs, P. *et al.* (2010) ‘Fire regime: History and definition of a key concept in disturbance ecology’, *Theory in Biosciences*, 129(1), pp. 53–69. doi: 10.1007/s12064-010-0082-z.

Krull, E. S., Thompson, C. H. and Skjemstad, J. O. (2004) ‘Chemistry, Radiocarbon ages and Development of a Subtropical Acid Peat in Queensland, Australia’, *Australian Journal of Soil Research*, 42, pp. 411–425.

Lamb, M. P. *et al.* (2013) ‘Sediment storage by vegetation in steep bedrock landscapes : Theory , experiments , and implications for post fire sediment yield’, *Journal of Geophysical Research: Earth’ Surface*, 118(June), pp. 1147–1160. doi: 10.1002/jgrf.20058.

Lammers, K., Arbuckle-Keil, G. and Dighton, J. (2009) ‘FT-IR study of the changes in carbohydrate chemistry of three New Jersey pine barrens leaf litters during simulated control burning’, *Soil Biology and Biochemistry*. Elsevier Ltd, 41(2), pp. 340–347. doi: 10.1016/j.soilbio.2008.11.005.

Lehto, T., Ruuhola, T. and Dell, B. (2010) ‘Forest Ecology and Management Boron in forest trees and forest ecosystems’, *Forest Ecology and Management*. Elsevier B.V., 260(12), pp. 2053–2069. doi: 10.1016/j.foreco.2010.09.028.

Lemarchand, D. *et al.* (2002) ‘An optimized procedure for boron separation and mass spectrometry

analysis for river samples', *Chemical Geology*, 182(2–4), pp. 323–334. doi: http://dx.doi.org/10.1016/S0009-2541(01)00329-1.

Lemarchand, D. *et al.* (2012) 'Boron isotopes in different grain size fractions : Exploring past and present water – rock interactions from two soil profiles (Strengbach , Vosges Mountains)', *Geochimica et Cosmochimica Acta*. Elsevier Ltd, 98, pp. 78–93. doi: 10.1016/j.gca.2012.09.009.

Lemarchand, E., Schott, J. and Gaillardet, J. É. (2005) 'Boron isotopic fractionation related to boron sorption on humic acid and the structure of surface complexes formed', *Geochim. Cosmochim. Acta*, 69(14), pp. 3519–3533. doi: 10.1016/j.gca.2005.02.024.

Liland, K. H., Mevik, B.-H. and Canteri, R. (2020) 'Package " baseline "'.

Lynch, A. H. *et al.* (2007) 'Using the Paleorecord to Evaluate Climate and Fire Interactions in Australia', *Annual Review of Earth and Planetary Sciences*, 35(1), pp. 215–239. doi: 10.1146/annurev.earth.35.092006.145055.

Madejová, J. and Komadel, P. (2001) 'Baseline Studies of the Clay Minerals Society Source Clays: Infrared Methods', *Clays and Clay Minerals*, 49(5), pp. 410–432.

Marentes, E., Vanderpool, R. A. and Shelp, B. J. (1997) 'Boron-isotope fractionation in plants', *Short Communication*, (Shelp 1993), pp. 10–12.

Mariani, M. *et al.* (2016) 'ENSO controls interannual fire activity in southeast Australia', *Geophysical Research Letters*, pp. 891–900. doi: 10.1002/2016GL070572.

Mastrolonardo, G. *et al.* (2014) 'Application of thermal and spectroscopic techniques to assess fire-induced changes to soil organic matter in a Mediterranean forest', *Journal of Geochemical Exploration*. Elsevier B.V., 143, pp. 174–182. doi: 10.1016/j.gexplo.2014.04.010.

Mastrolonardo, G. *et al.* (2015) 'Soil pyrogenic organic matter characterisation by spectroscopic analysis : a study on combustion and pyrolysis residues', *J Soil Sediments*, 15, pp. 769–780. doi: 10.1007/s11368-014-1034-x.

McParland, L. C. *et al.* (2009) 'The use of reflectance values for the interpretation of natural and anthropogenic charcoal assemblages', *Archaeological and Anthropological Sciences*, 1(4), pp. 249–261. doi: 10.1007/s12520-009-0018-z.

Merino, A. *et al.* (2015) 'Variability in the composition of charred litter generated by wildfire in different ecosystems', *Catena*. Elsevier B.V., 133, pp. 52–63. doi: 10.1016/j.catena.2015.04.016.

Meyer, G. A. *et al.* (1992) 'Response of Alluvial Systems to Fire and Climate Change in Yellowstone

National Park', *Letters to Nature*, 357(May), pp. 147–150.

Morgan, P. *et al.* (2014) 'Challenges of assessing fire and burn severity using field measures, remote sensing and modelling', *International Journal of Wildland Fire*, 23(8), pp. 1045–1060. doi: 10.1071/WF13058.

Nave, L. E., Vance, E. D. and Swanston, C. W. (2011) 'Fire effects on temperate forest soil C and N storage', *Ecological Applications*, 21(4), pp. 1189–1201.

Nelson, N. A. (2010) 'Late-Holocene relationships among fire , climate and vegetation in a forest-sagebrush ecotone of southwestern Idaho , USA', *The Holocene*, 20(July 2009), pp. 1179–1194. doi: 10.1177/0959683610371992.

Nocentini, C. *et al.* (2010) 'Organic Geochemistry Nature and reactivity of charcoal produced and added to soil during wildfire are particle-size dependent', *Organic Geochemistry*. Elsevier Ltd, 41(7), pp. 682–689. doi: 10.1016/j.orggeochem.2010.03.010.

Nyman, P. *et al.* (2020) 'Debris-flow-dominated sediment transport through a channel network after wildfire', *Earth Surface Processes and Landforms*, 1167(February), pp. 1155–1167. doi: 10.1002/esp.4785.

Office of Environment of Heritage (2014) *Statement of Management Intent Upper Nepean State Conservation Area*.

Olariu, C. *et al.* (2012) 'Tidal dunes versus tidal bars : The sedimentological and architectural characteristics of compound dunes in a tidal seaway , the lower Baronia Sandstone (Lower Eocene), Ager Basin, Spain', *Sedimentary Geology*. Elsevier B.V., 279, pp. 134–155. doi: 10.1016/j.sedgeo.2012.07.018.

Orians, G. H. and Milewski, A. V (2007) 'Ecology of Australia : the effects of nutrient-poor soils and intense fires', *Biological Reviews*, 82, pp. 393–423. doi: 10.1111/j.1469-185X.2007.00017.x.

Peak, D., Luther, G. W. and Sparks, D. L. (2003) 'ATR-FTIR spectroscopic studies of boric acid adsorption on hydrous ferric oxide', *Geochimica et Cosmochimica Acta*, 67(14), pp. 2551–2560. doi: 10.1016/S0016-7037(03)00096-6.

Peltola, P. and Åström, M. (2006) 'Can boron and boron isotopes be used as a sedimentary marker for fire events? A case study from a historic urban fire event in W Finland', *Applied Geochemistry*, 21(6), pp. 941–948. doi: 10.1016/j.apgeochem.2006.01.005.

Pereira, P., Úbeda, X. and Martin, D. A. (2012) 'Fire severity effects on ash chemical composition and

water-extractable elements', *Geoderma*. Elsevier B.V., 191, pp. 105–114. doi: 10.1016/j.geoderma.2012.02.005.

Pierce, J. L., Meyer, G. A. and Jull, A. J. T. (2004) 'Fire-induced erosion and millennial- scale climate change in northern ponderosa pine forests', *Letters to Nature*, 432(November), pp. 87–90. doi: 10.1038/nature03028.Published.

Prosser, I. (1987) 'Fire , Humans and Denudation at Wangrah Creek, Southern Tablelands, NSW', *Australian Geographical Studies*.

Recher, H. F., Hutchings, P. A. and Rosen, S. (1993) 'The biota of the Hawkesbury-Nepean catchment : reconstruction and restoration', *Australian Zoologist*, 29(1–2), pp. 3–41.

Richards, A. E. *et al.* (2012) 'Effect of fire and tree-grass patches on soil nitrogen in Australian tropical savannas', *Austral Ecology*, 37, pp. 668–677. doi: 10.1111/j.1442-9993.2011.02335.x.

Romer, R. L. and Meixner, A. (2014) 'Lithium and boron isotopic fractionation in sedimentary rocks during metamorphism – The role of rock composition and protolith mineralogy', *Geochimica et Cosmochimica Acta*, 128(0), pp. 158–177. doi: http://dx.doi.org/10.1016/j.gca.2013.11.032.

Roux, P. *et al.* (2014) 'A Rapid Method for Determining Boron Concentration (ID-ICP-MS) and δ11B (MC-ICP-MS) in Vegetation Samples after Microwave Digestion and Cation Exchange Chemical Purification', *Geostandards and Geoanalytical Research*, 39(4), pp. 453–466. doi: 10.1111/j.1751-908X.2014.00328.x.

Roux, P. *et al.* (2017) 'Boron Dissolved and Particulate Atmospheric Inputs to a Forest Ecosystem (Northeastern France)', *Environmental science & technology*, 51, p. 14038−14046. doi: 10.1021/acs.est.7b03226.

Sah, R. N. and Brown, P. H. (1997) 'Techniques for boron determination and their application to the analysis of plant and soil samples', *Plant and Soil*, 193(1–2), pp. 15–33. doi: 10.1007/978-94-011-5580-9_2.

Sawyer, R. *et al.* (2018a) 'Fire intensity drives post-fire temporal pattern of soil carbon accumulation in Australian fire-prone forests', *Science of the Total Environment*. Elsevier B.V., 610–611, pp. 1113–1124. doi: 10.1016/j.scitotenv.2017.08.165.

Sawyer, R. *et al.* (2018b) 'Soil carbon in Australian fire-prone forests determined by climate more than fire regimes', *Science of the Total Environment*. Elsevier B.V., 639, pp. 526–537. doi: 10.1016/j.scitotenv.2018.05.169.

Schmitt, A. D. *et al.* (2012) 'Processes controlling the stable isotope compositions of Li, B, Mg and Ca in plants, soils and waters: A review', *Comptes Rendus - Geoscience*, 344(11–12), pp. 704–722. doi: 10.1016/j.crte.2012.10.002.

Sen, S., Xu, Z. and Stebbins, J. F. (1998) 'Temperature dependent structural changes in borate , borosilicate studies', *Journal of Non-Crystalline Solids*, 226, pp. 29–40.

Shakesby, R. A. *et al.* (2003) *Fire severity, water repellency characteristics and hydrogeomorphological changes following the Christmas 2001 Sydney forest fires*, *Australian Geographer*. doi: 10.1080/00049180301736.

Sheikh, R. and Barua, A. G. (2013) 'X-ray diffraction and Fourier transform infrared spectra of the bricks of the Kamakhya temple', *Indian Journal of Pure and Applied Physics*, 51(November), pp. 745–748.

Shih, S.-M. and Komar, P. D. (1990) 'Differential bedload transport rates in a gravel-bed stream: A grain-size distribution approach', *Earth Surface Processes and Landforms*, 15, pp. 539–552. doi: 10.1002/esp.3290170608.

Shima, M. (1963) 'Geochemical study of boron isotopes', *Geochimica et Cosmochimica Acta*, 27(8), pp. 911–913.

Simkovic, I. *et al.* (2008) 'Thermal destruction of soil water repellency and associated changes to soil organic matter as observed by FTIR spectroscopy', *Catena*, 74, pp. 205–211. doi: 10.1016/j.catena.2008.03.003.

Singhvi, A. K. *et al.* (2011) 'Changes in Natural OSL Sensitivity During Single Aliquot Regeneration Procedure and Their Implications for Equivalent Dose Determination', *Geochronometria*, 38(3), pp. 231–241. doi: 10.2478/s13386-011-0028-3.

Skjemstad, J. O., Janik, L. J. and Taylor, J. A. (1998) 'Non-Living Soil Organic Matter: What do we know about it?', *Australian Journal of Experimental Agriculture*, 38, pp. 667–680.

Smidt, E. *et al.* (2005) 'Characterization of different decomposition stages of biowaste using FT-IR spectroscopy and pyrolysis-field ionization mass spectrometry', *Biodegradation*, 16(1), pp. 67–79. doi: 10.1007/s10531-004-0430-8.

Smith, H. G. *et al.* (2011) 'Wildfire effects on water quality in forest catchments : A review with implications for water supply', *Journal of Hydrology*. Elsevier B.V., 396(1–2), pp. 170–192. doi: 10.1016/j.jhydrol.2010.10.043.

Stebbins, J. F. and Ellsworth, S. E. (1996) 'Temperature Effects on Structure and Dynamics in Borate

and Borosilicate Liquids: High-Resolution and High-Temperature NMR Results', *J. Am. Ceram. Soc*, 79(9), pp. 2247–56.

Stivrins, N. *et al.* (2019) 'Integrating fire-scar, charcoal and fungal spore data to study fire events in the boreal forest of northern Europe', *Holocene*. doi: 10.1177/0959683619854524.

Stuiver, M. and Polach, H. A. (1977) 'Discussion Reporting of 14C Data', *Radiocarbon*, 19(3), pp. 355–363.

Sun, A. *et al.* (2019) 'Extraction and Analysis of Available Boron Isotopes in Soil Using Multicollector Inductively Coupled Plasma Mass Spectrometry', *Journal of Agricultural and Food Chemistry*. American Chemical Society, 67, pp. 7183–7189. doi: 10.1021/acs.jafc.9b01455.

Thomas, R. (2001) *TUTORIAL A Beginner's Guide to ICP-MS*, *Spectroscopy*.

Vengosh, A. *et al.* (1991) 'Boron isotope geochemistry of Australian salt lakes', *Geochimica et Cosmochimica Acta*, 55(9), pp. 2591–2606.

White, I. *et al.* (2006) 'The Vulnerability of Water Supply Catchments to bushfires: Impacts of the January 2003 Wildfires on the Australian Capital Territory', *Australasian Journal of Water Resources*, 10(2), pp. 179–194. doi: 10.1080/13241583.2006.11465291.

Wickham, H. (2016) *ggplot2: Elegant Graphics for Data Analysis*.

Williams, L. B. *et al.* (2001) 'The influence of organic matter on the boron isotope geochemistry of the gulf coast sedimentary basin, USA', *Chemical Geology*, 174(4), pp. 445–461.

Xiao, J. *et al.* (2013) 'Boron isotope variations and its geochemical application in nature', *Australian Journal of Earth Sciences*, 60, pp. 431–447. doi: 10.1080/08120099.2013.813585.

Xu, Q. *et al.* (2015) 'Separation and Analysis of Boron Isotope in High Plant by Thermal Ionization Mass Spectrometry', *Hindawi Publishing Corporation*, 2015, pp. 1–6.

8 Appendix

Appendix A Hornes Creek

Appendix A is comprised of the core logs, complete, baseline corrected ATR-FTIR spectra, grain size and core moisture content data for Hornes Creek 1 cores 1 and 2.

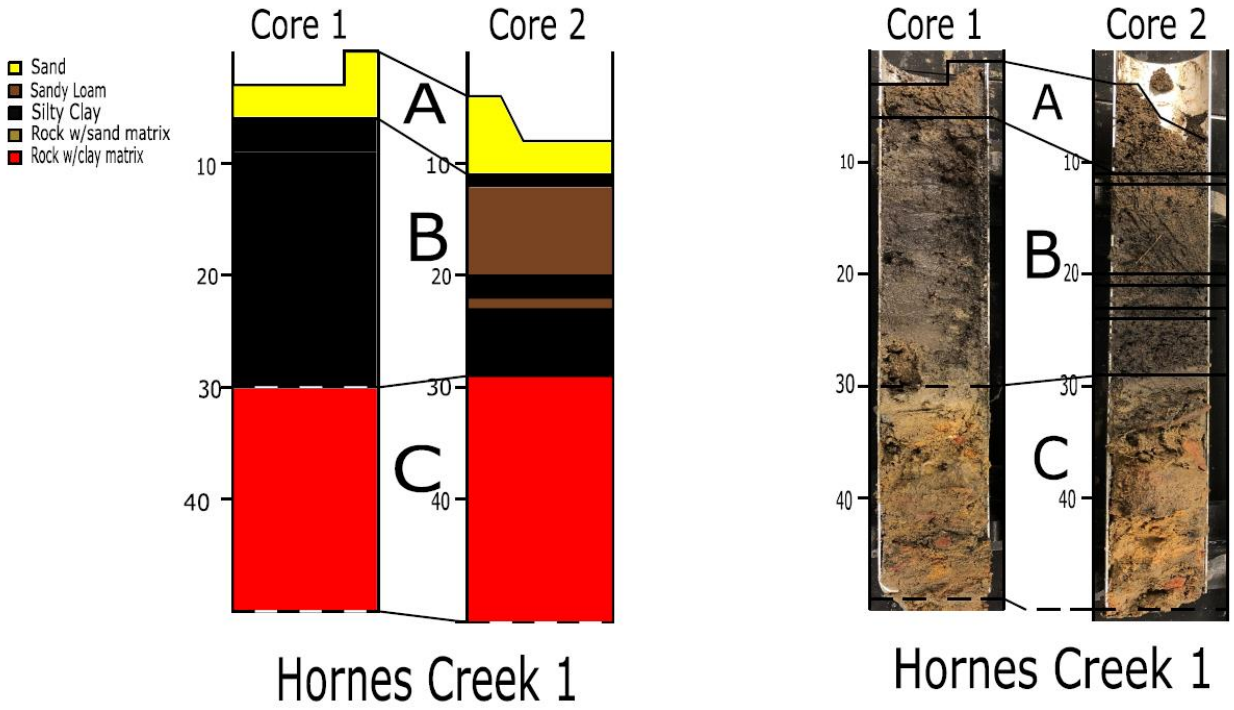

Figure A.1 Core Logs for Hornes Creek 1 Core 1 and Hornes Creek 1 Core 2.

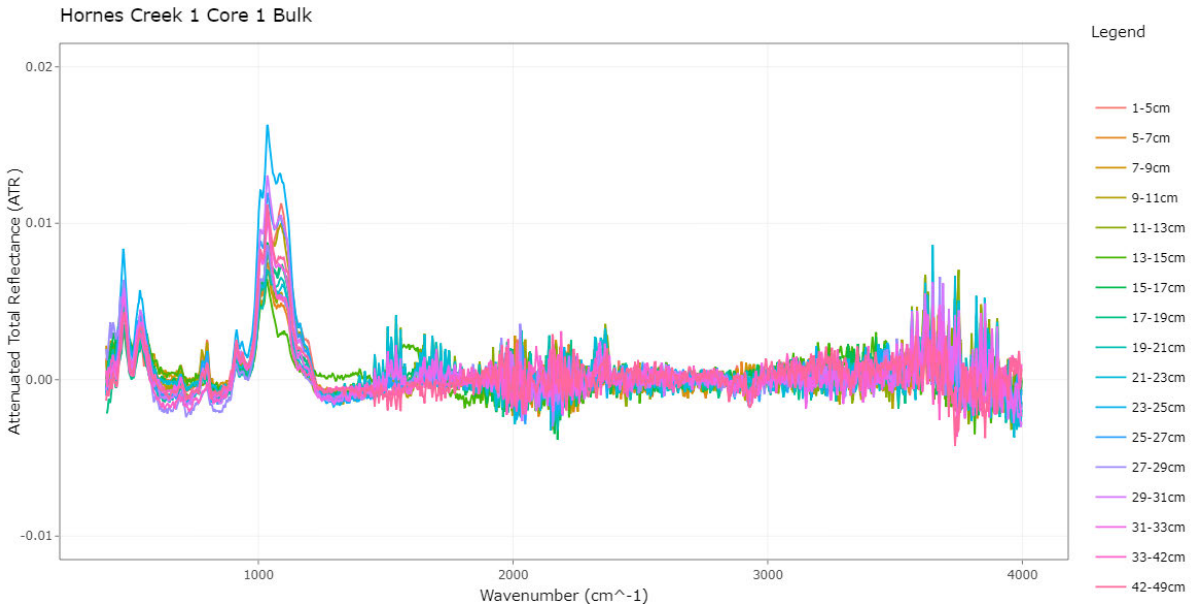

Figure A.2 Complete (4000-400cm^{-1}) baseline-corrected ATR-FTIR spectra the Hornes Creek 1 Core 1 Bulk fraction as a function of depth.

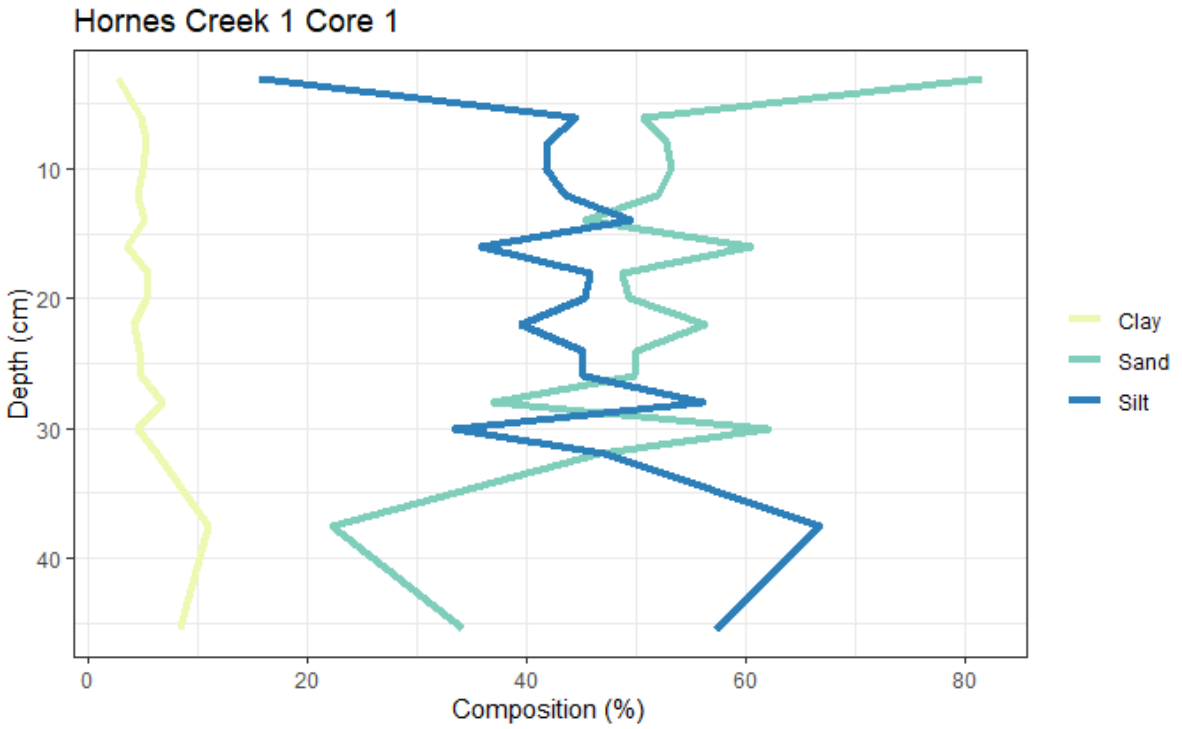

Figure A.3 Grain size data for Hornes Creek 1 Core 1, highlighting the changes in clay (yellow), sand (green) and silt (blue) as a function of depth.

Table 1 Core moisture content data for Hornes Creek 1 Core 1.

Sample No.	Depth (cm)	Moisture Content (%)
1	1-5	26.56
2	5-7	26.16
3	7-9	30.74
4	9-11	38.83
5	11-13	37.13
6	13-15	42.23
7	15-17	38.97
8	17-19	40.83
9	19-21	38.32
10	21-23	34.96
11	23-25	33.47
12	25-27	32.58
13	27-29	27.06
14	29-31	17.00
15	31-33	13.89
16	33-42	15.87
17	42-49	13.48

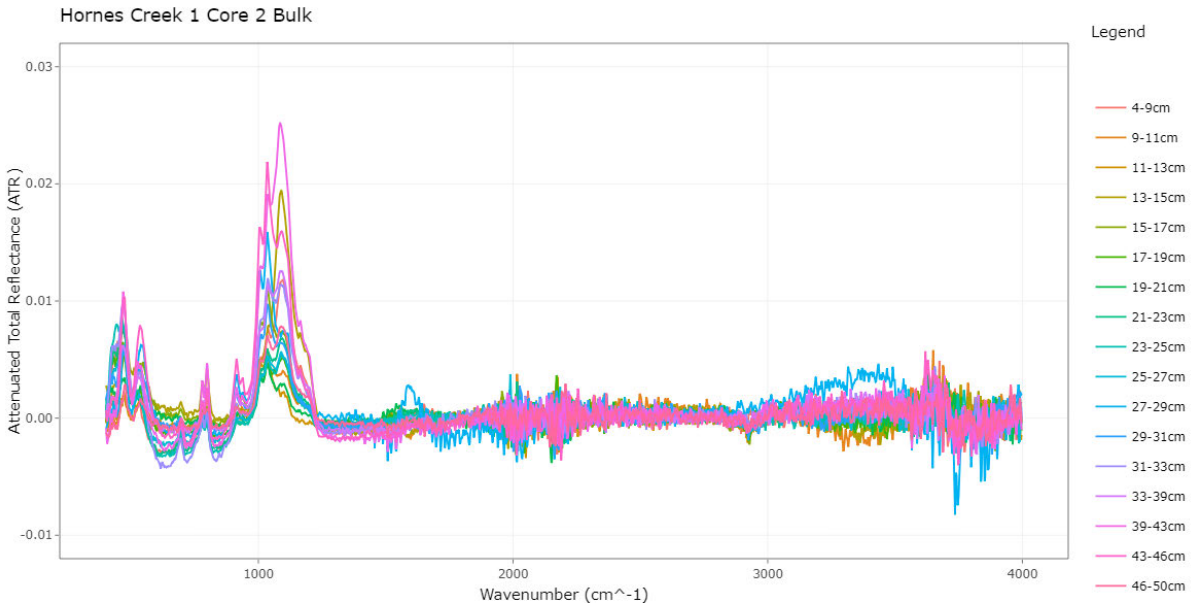

Figure A.4 Complete (4000-400cm^{-1}) baseline-corrected ATR-FTIR spectra the Hornes Creek 1 Core 2 Bulk fraction as a function of depth.

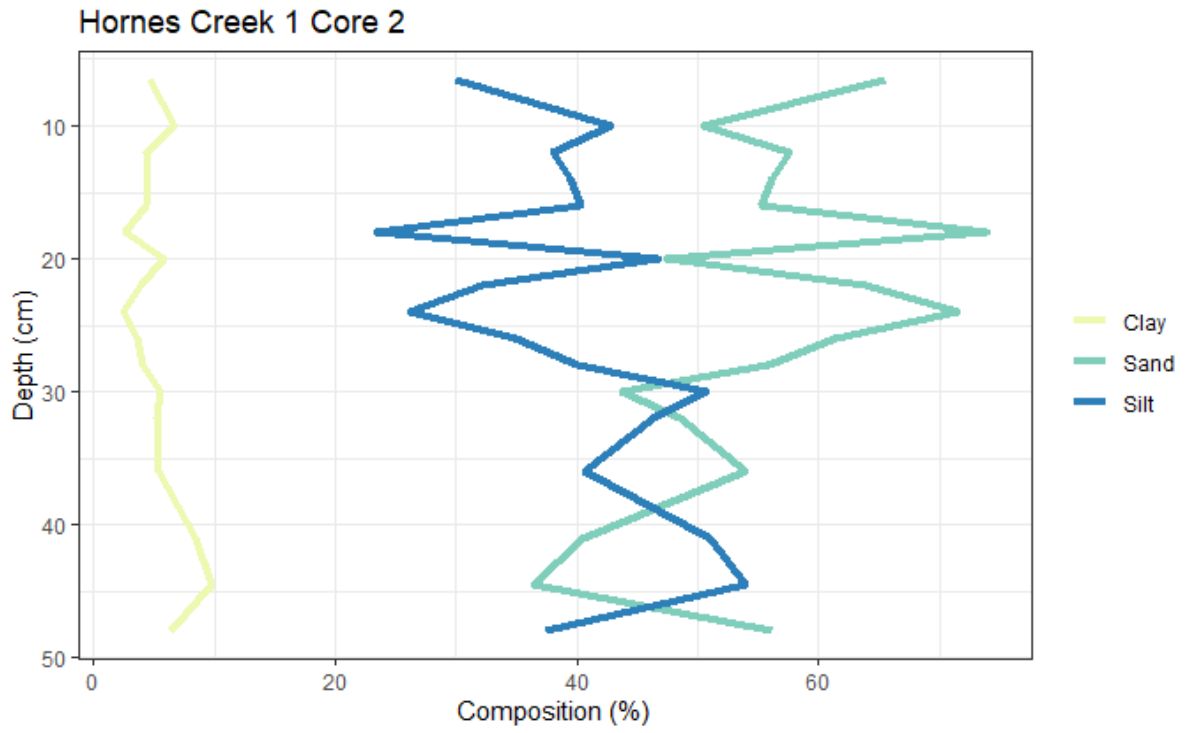

Figure A.5 Grain size data for Hornes Creek 1 Core 2, highlighting the changes in clay (yellow), sand (green) and silt (blue) as a function of depth.

Table 2 Core moisture content data for Hornes Creek 1 Core 2.

Sample No.	Depth (cm)	Moisture Content (%)
1	4-9	19.44
2	9-11	30.04
3	11-13	31.45
4	13-15	21.37
5	15-17	24.08
6	17-19	28.02
7	19-21	29.79
8	21-23	38.59
9	23-25	38.84
10	25-27	41.76
11	27-29	42.86
12	29-31	32.16
13	31-33	27.57
14	33-39	16.35
15	39-43	12.40
16	43-46	12.52
17	46-50	14.63

Appendix B Long Creek

Appendix B is comprised of the complete, baseline-corrected ATR-FTIR spectra for Long Creek 1 and 2 as well as grain size analysis and core moisture content data.

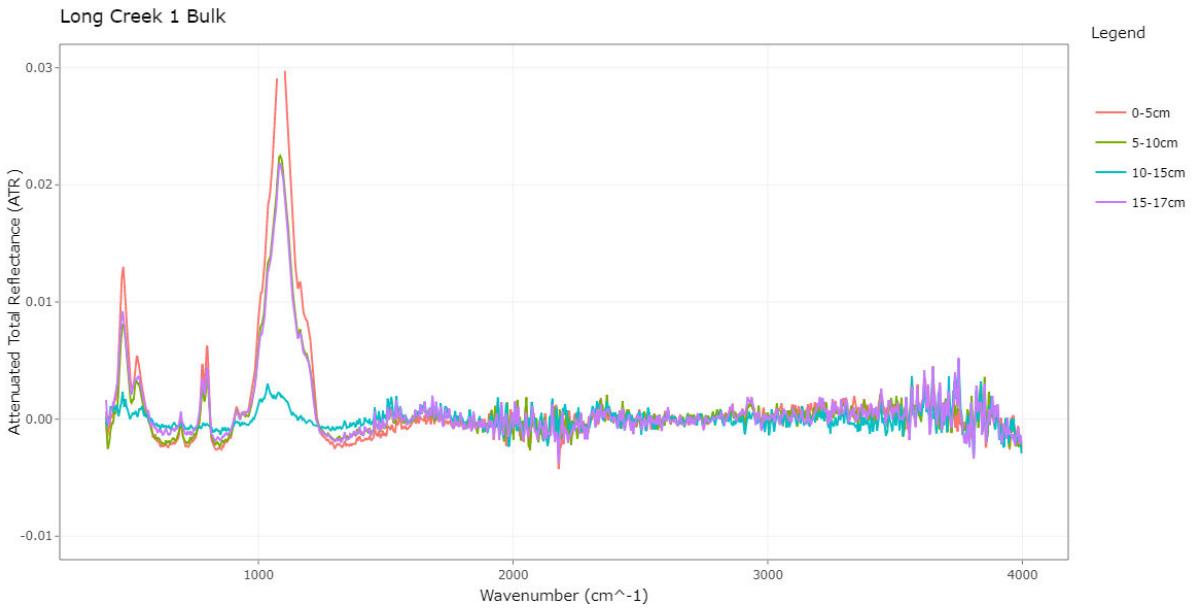

Figure B.1 Complete (4000-400cm^{-1}) baseline-corrected ATR-FTIR spectra the Long Creek 1 bulk fraction as a function of depth.

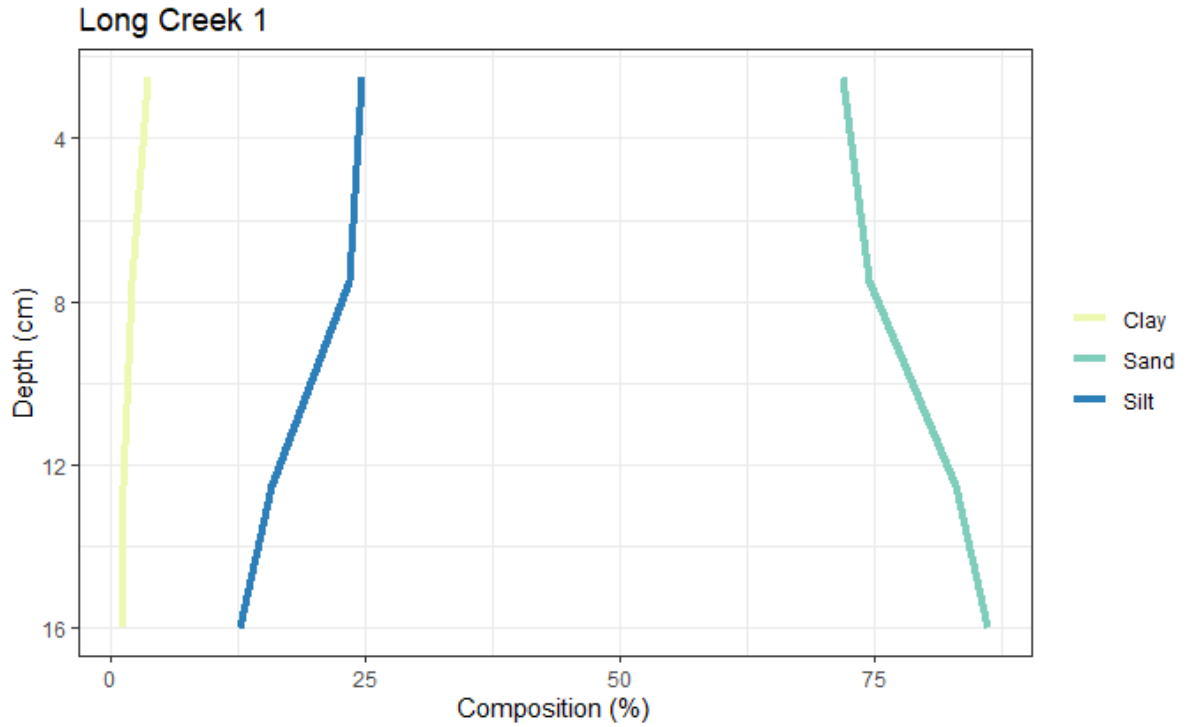

Figure B.2 Grain size data for Long Creek 1, highlighting the changes in clay (yellow), sand (green) and silt (blue) as a function of depth.

Table 3 Core moisture content data for Long Creek 1.

Depth (cm)	Moisture Content (%)
0-5cm	27.92
5-10cm	38.89
10-15cm	47.17
15-17cm	34.88

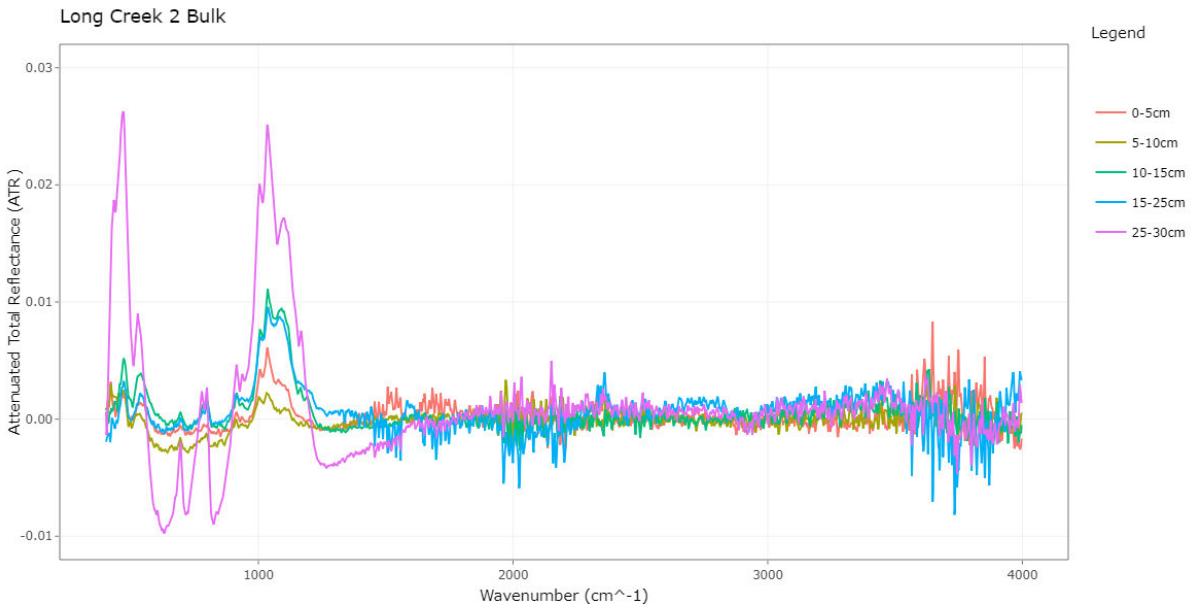

Figure B.3 Complete (4000-400cm^{-1}) baseline-corrected ATR-FTIR spectra the Long Creek 2 bulk fraction as a function of depth.

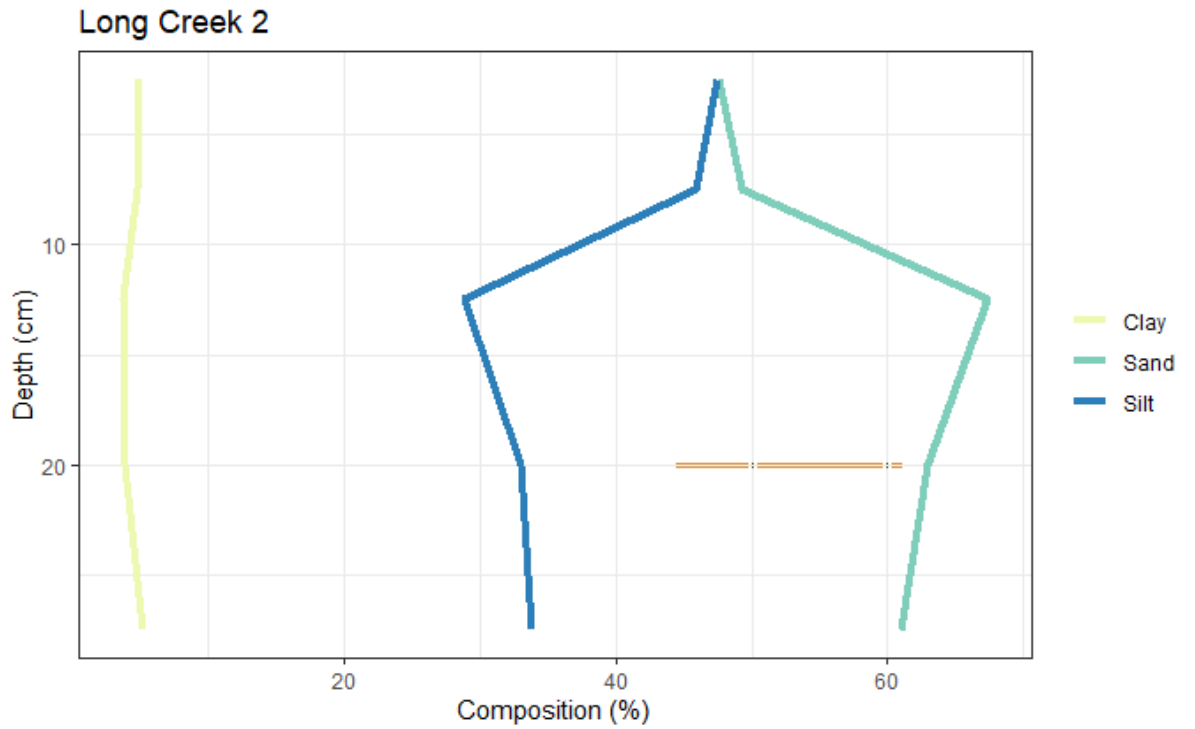

Figure B.4 Grain size data for Long Creek 2, highlighting the changes in clay (yellow), sand (green) and silt (blue) as a function of depth.

Table 4 Core moisture content data for Long Creek 2.

Depth (cm)	Moisture Content (%)
0-5cm	24.53
5-10cm	22.54
10-15cm	15.72
15-25cm	24.62
25-30cm	18.57

Appendix C Rebecca Creek

Appendix C is comprised of the core logs, baseline-corrected ATR-FTIR spectra, grain size analysis and core moisture content data for Rebecca Creek 1 Core 1, collected in 2020. It also contains spectra targeting specific bands for the Rebecca Creek samples collected in 2017 that are discussed in chapter 5.

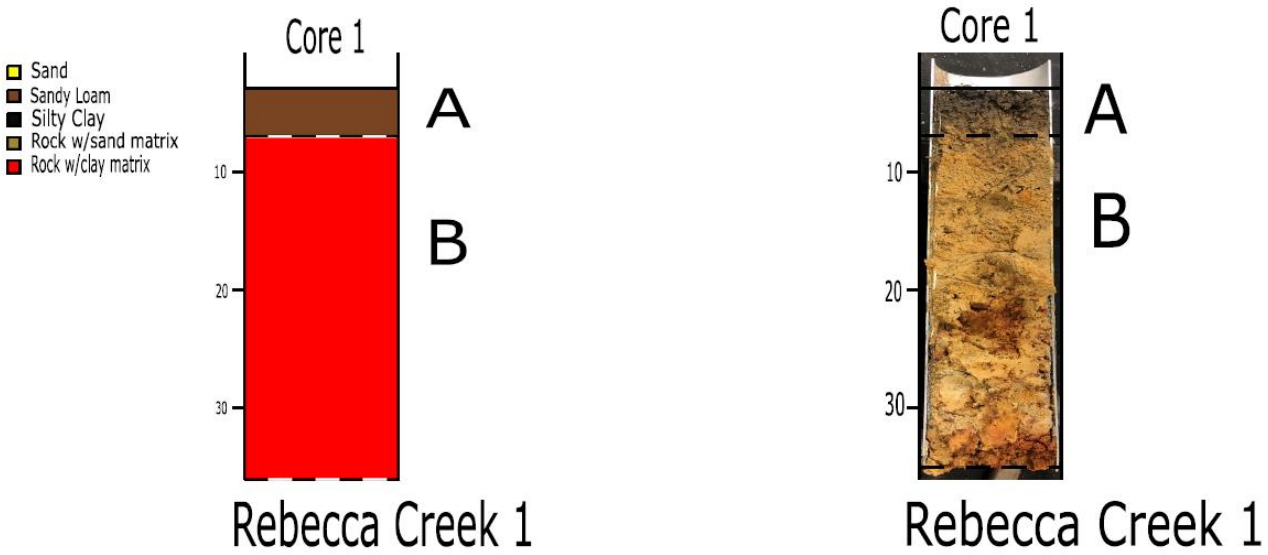

Figure C.1 Core log for Rebecca Creek 1 Core 1 collected in 2020.

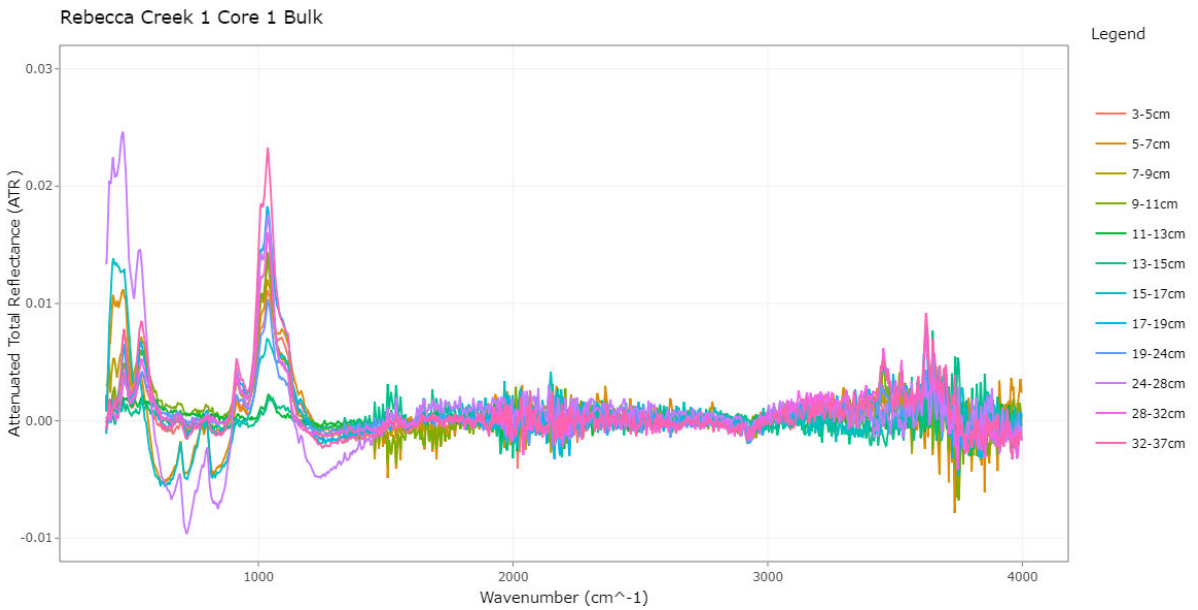

Figure C.2 Complete (4000-400cm^{-1}) baseline-corrected ATR-FTIR spectra for the Rebecca Creek 1 Core 1 bulk fraction, collected in 2020, as a function of depth.

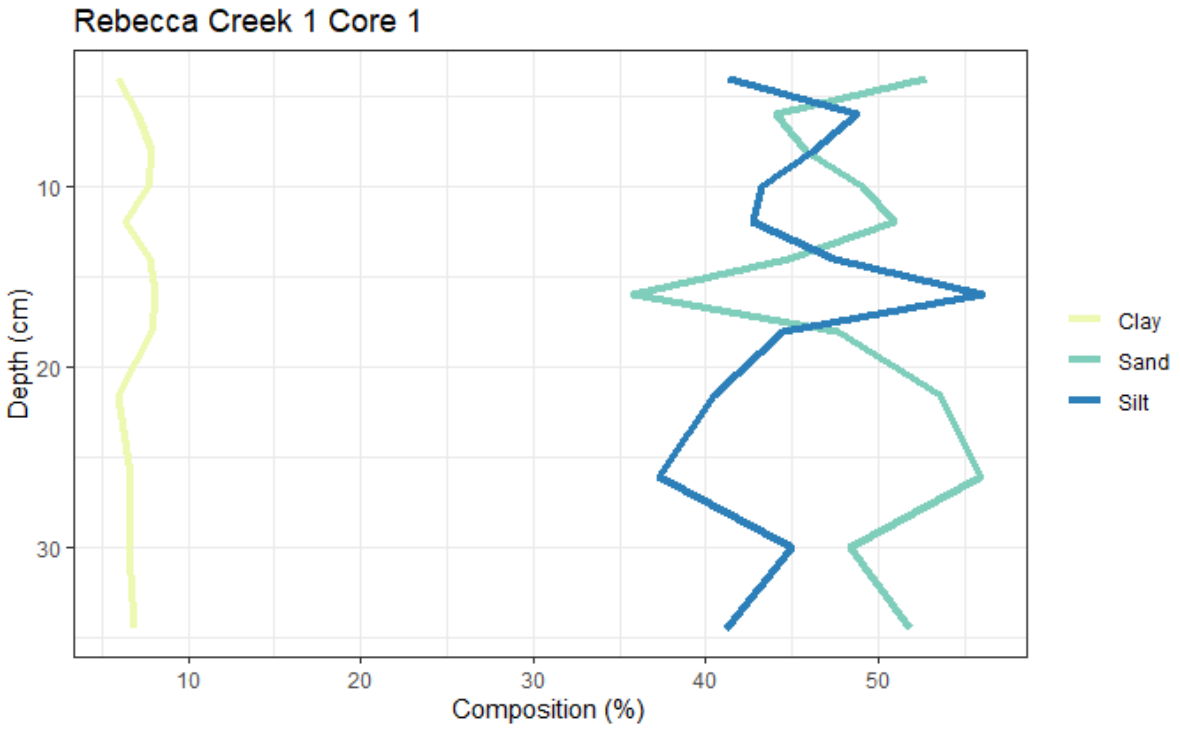

Figure C.3 Grain size data for Rebecca Creek 1 Core 1, highlighting the changes in clay (yellow), sand (green) and silt (blue) as a function of depth.

Table 5 Core moisture content data for Rebecca Creek 1 Core 1.

Sample No.	Depth (cm)	Moisture Content (%)
1	3-5	28.40
2	5-7	24.84
3	7-9	20.46
4	9-11	18.27
5	11-13	18.08
6	13-15	17.53
7	15-17	12.93
8	17-19	14.75
9	19-24	15.38
10	24-28	16.36
11	28-32	15.84
12	32-37	14.59

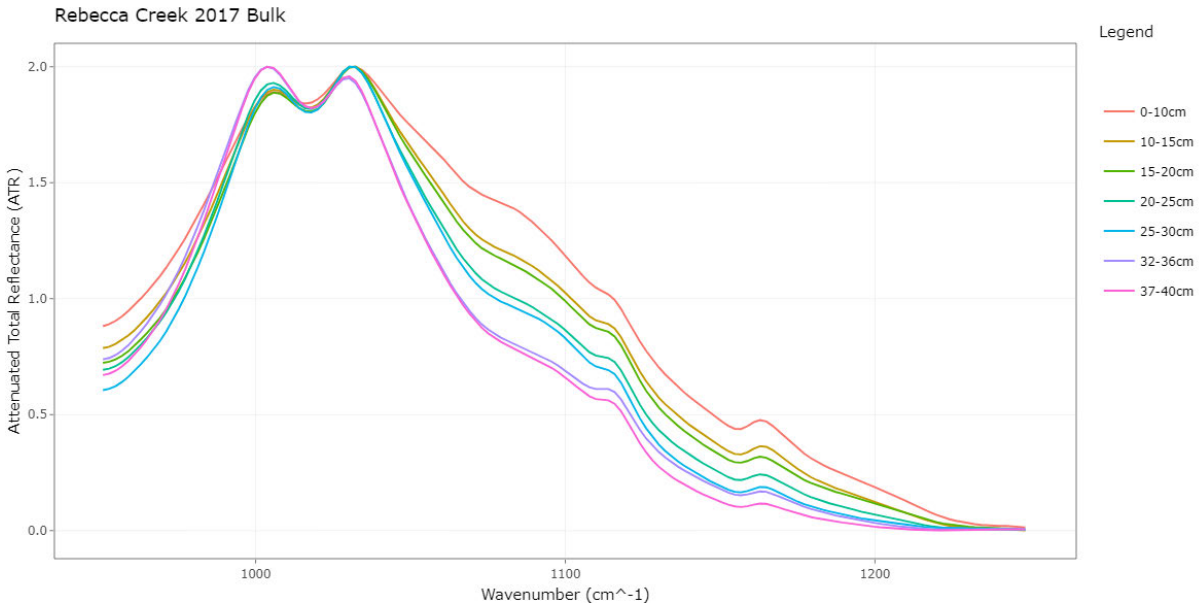

Figure C.4 Baseline-corrected ATR-FTIR spectra highlighting the band around 1170 to 950cm^{-1} for the bulk fraction from the Rebecca Creek 2017 samples as a function of depth. A general decreasing trend is evident with increasing depth.

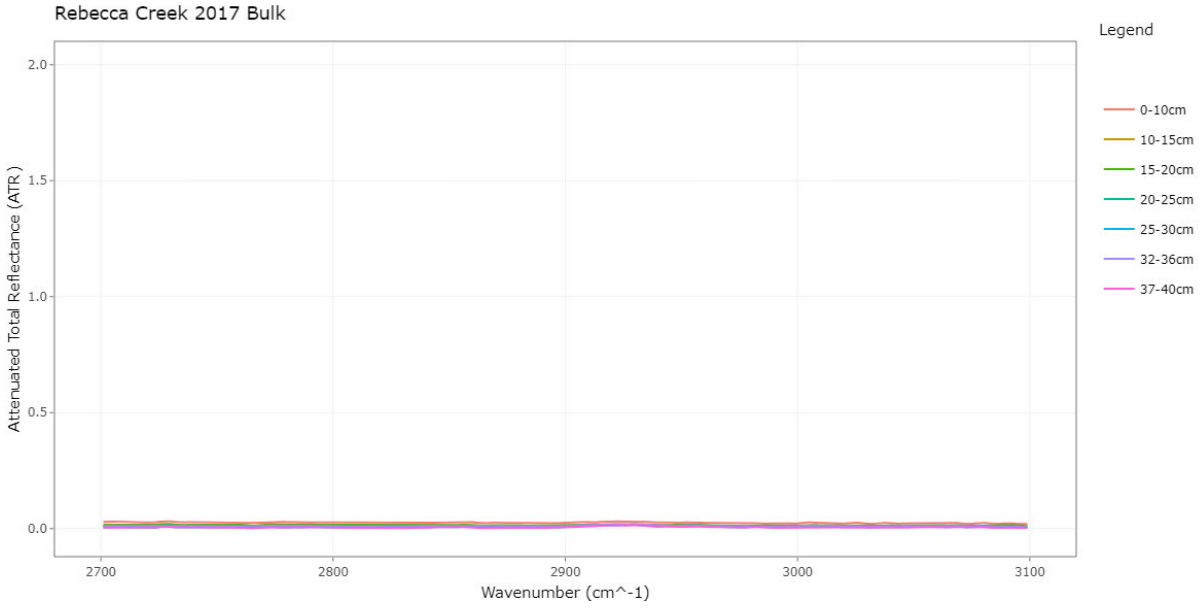

Figure C.5 Baseline-corrected spectra highlighting the bands at 3020-2800cm^{-1} and 3400cm^{-1} for the bulk fraction for the Rebecca Creek 2017 samples. No deviation from background is evident in this band.

Appendix D Washhouse Gully

Appendix D is comprised of the core logs for Washhouse Gully 1 Core 1 and Washhouse Gully 1 Core 2. It includes ATR-FTIR spectra targeting specific bands for Washhouse Gully 1 Core 1 discussed in Chapter 5 with figures arranged in the order in which they are discussed in text. Appendix D also encompasses the complete, baseline-corrected ATR-FTIR spectra and grain size analysis for Washhouse Gully 1 Core 2 and core moisture content data for both cores.

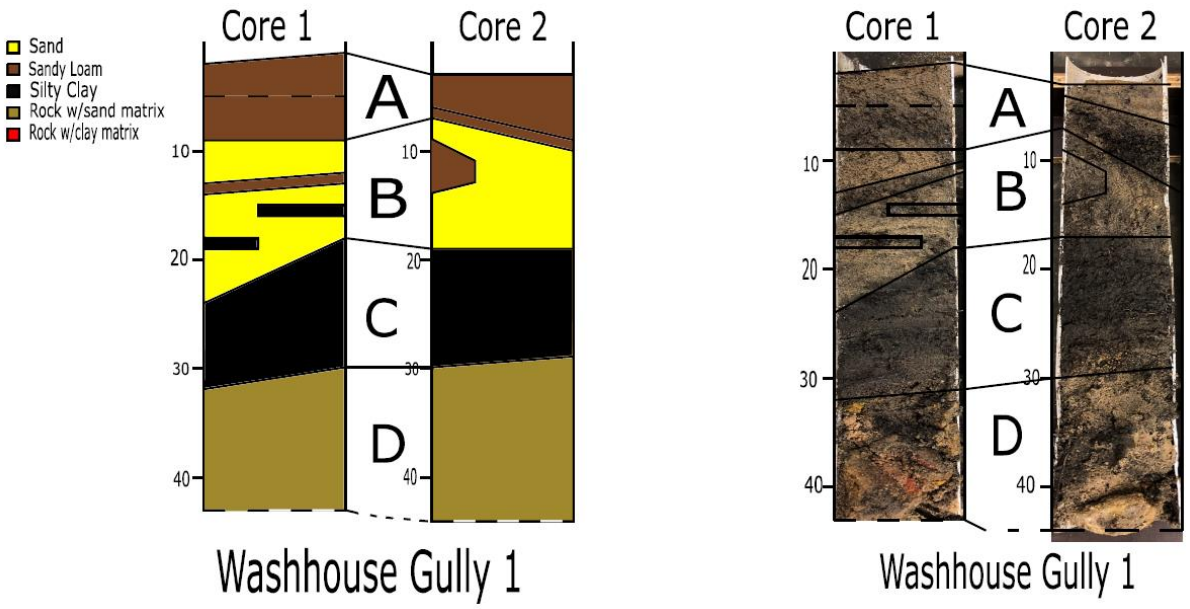

Figure D.1 Core logs for Washhouse Gully 1 Core 1 and Washhouse Gully 1 Core 2.

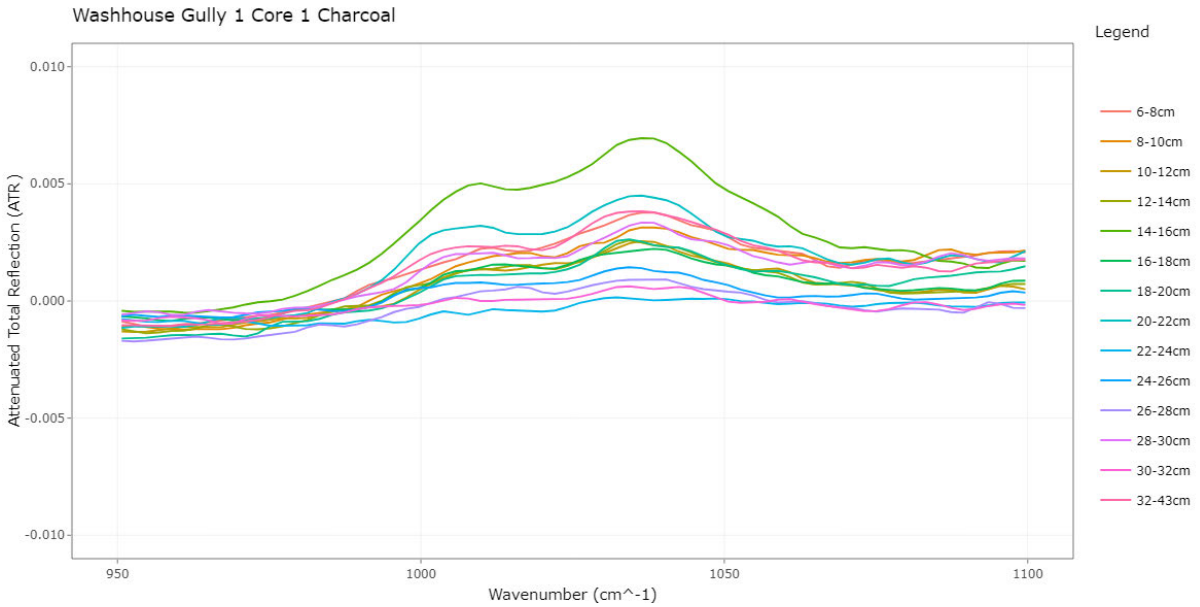

Figure D.2 Baseline-corrected ATR-FTIR spectra highlighting the band at 1030 cm^{-1} for the charcoal fraction from Washhouse Gully 1 Core 1 as a function of depth. No obvious trend is evident between charcoal-rich and non-charcoal-rich samples.

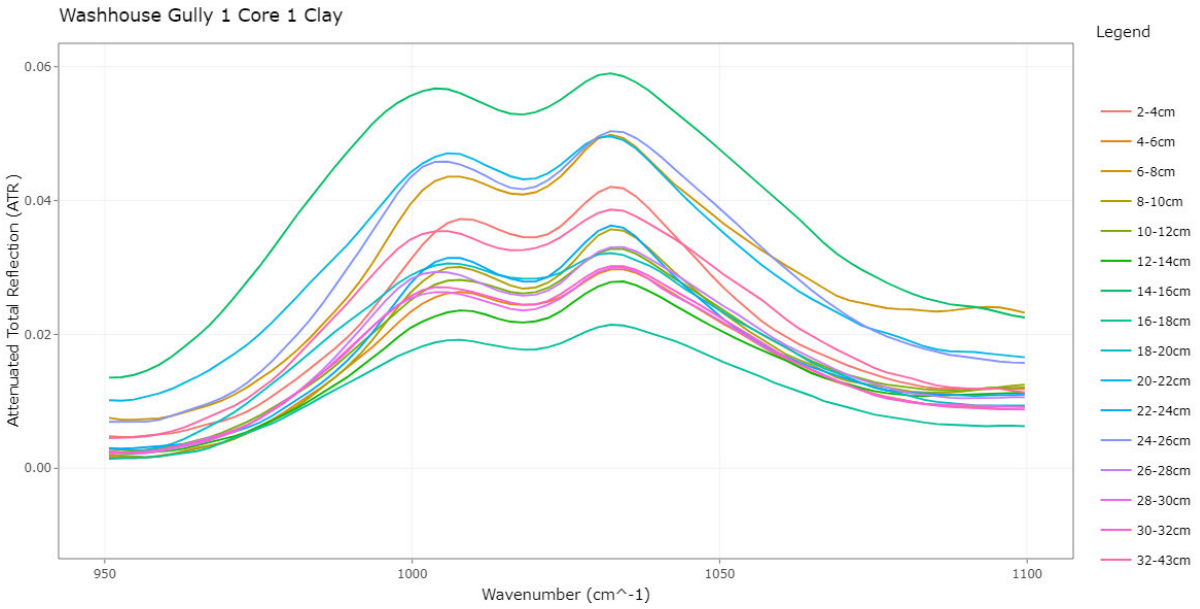

Figure D.3 Baseline-corrected ATR-FTIR spectra highlighting the band at 1030 cm^{-1} for the clay fraction from Washhouse Gully 1 Core 1 as a function of depth. No obvious trend is evident between charcoal-rich and non-charcoal-rich samples.

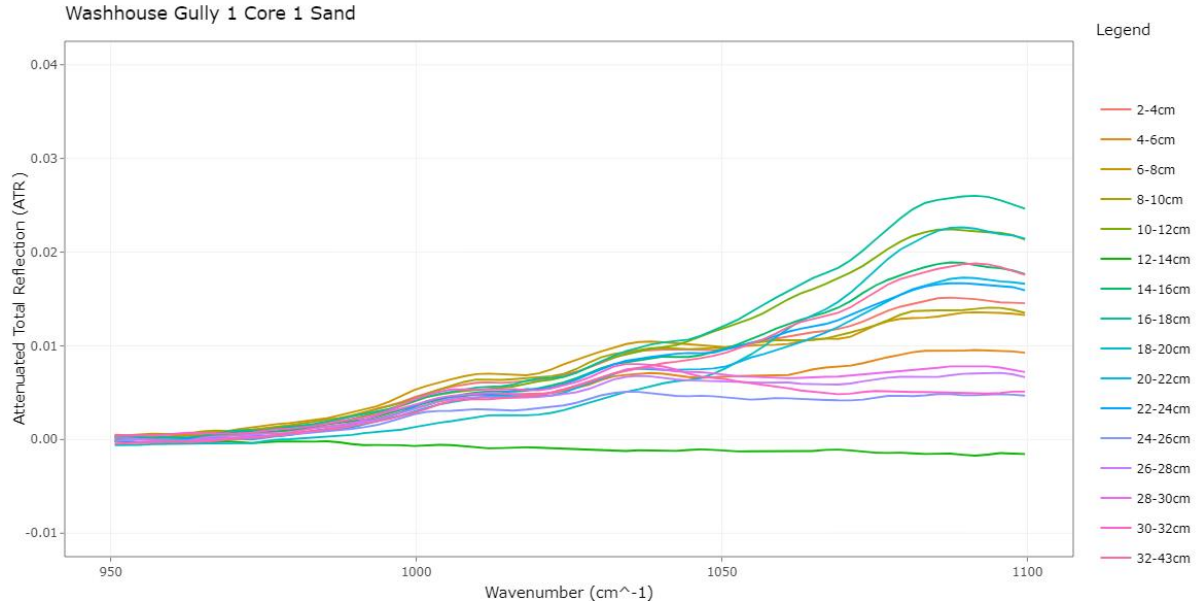

Figure D.4 Baseline-corrected ATR-FTIR spectra highlighting the band at 1030 cm^{-1} for the sand fraction from Washhouse Gully 1 Core 1 as a function of depth. No obvious trend is evident between charcoal-rich and non-charcoal-rich samples.

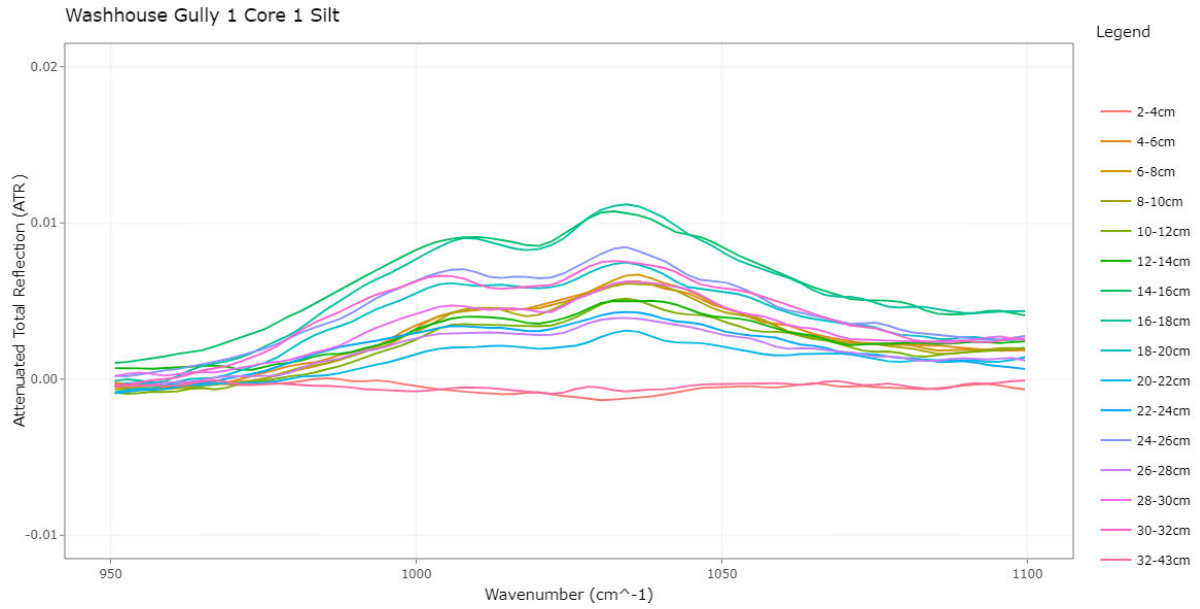

Figure D.5 Baseline-corrected ATR-FTIR spectra highlighting the band at 1030 cm^{-1} for the silt fraction from Washhouse Gully 1 Core 1 as a function of depth. No obvious trend is evident between samples.

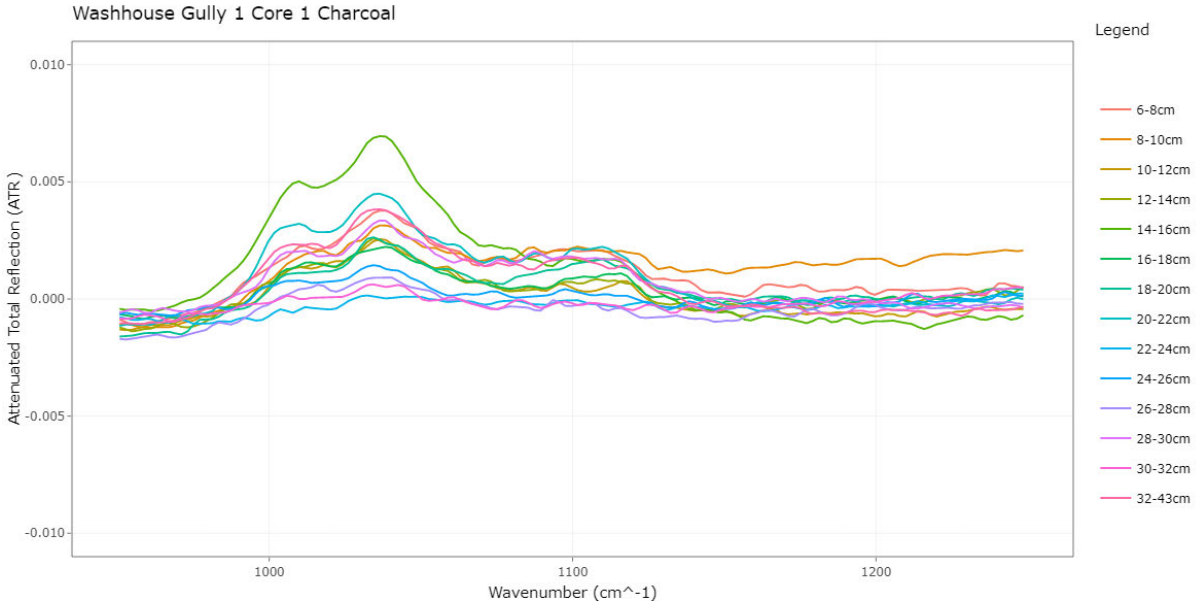

Figure D.6 Baseline-corrected ATR-FTIR spectra highlighting the band approximately 1170-950cm^{-1} for the charcoal fraction from Washhouse Gully 1 Core 1 as a function of depth. No obvious trend is evident between charcoal-rich and non-charcoal-rich samples.

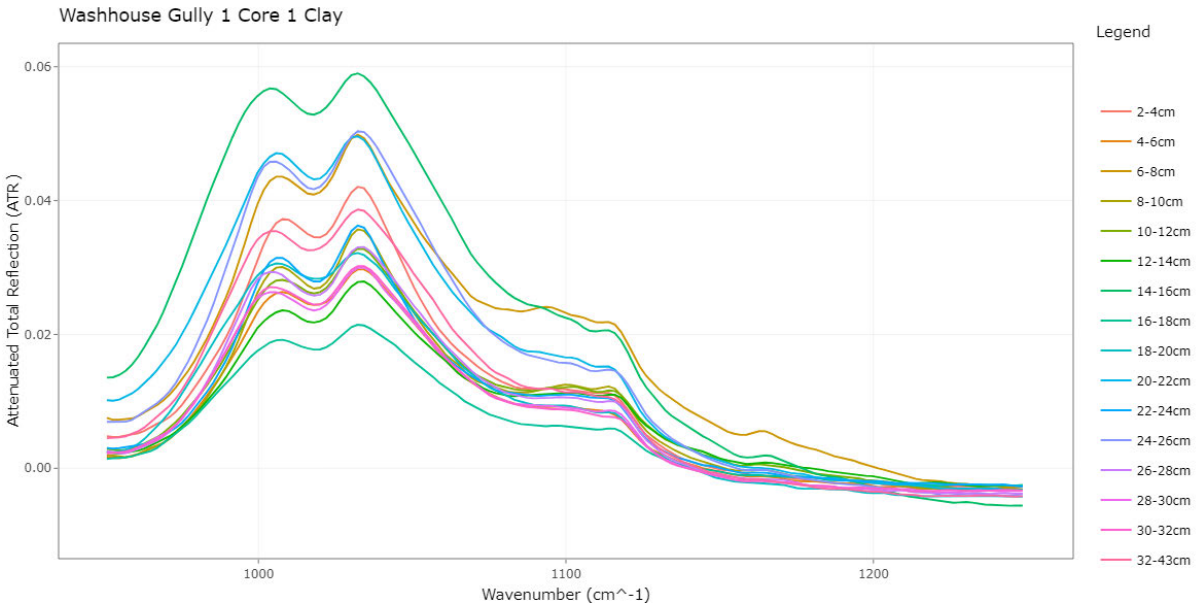

Figure D.7 Baseline-corrected ATR-FTIR spectra highlighting the band approximately 1170-950cm^{-1} for the clay fraction from Washhouse Gully 1 Core 1 as a function of depth. No obvious trend is evident between charcoal-rich and non-charcoal-rich samples.

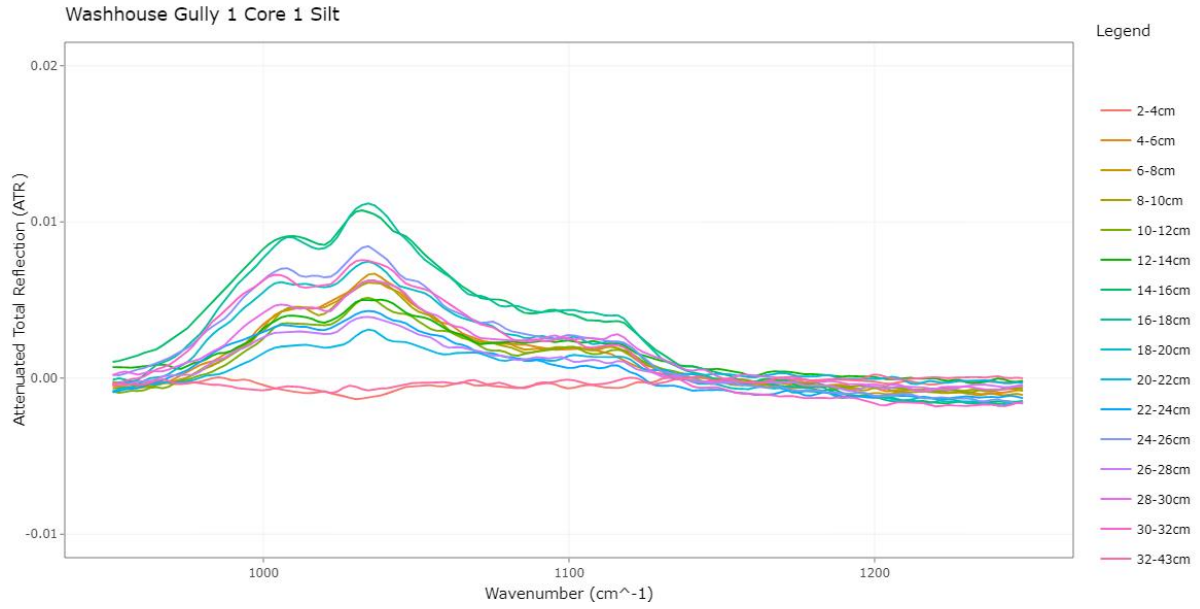

Figure D.8 Baseline-corrected ATR-FTIR spectra highlighting the band approximately 1170-950cm^{-1} for the silt fraction from Washhouse Gully 1 Core 1 as a function of depth. No obvious trend is evident between charcoal-rich and non-charcoal-rich samples.

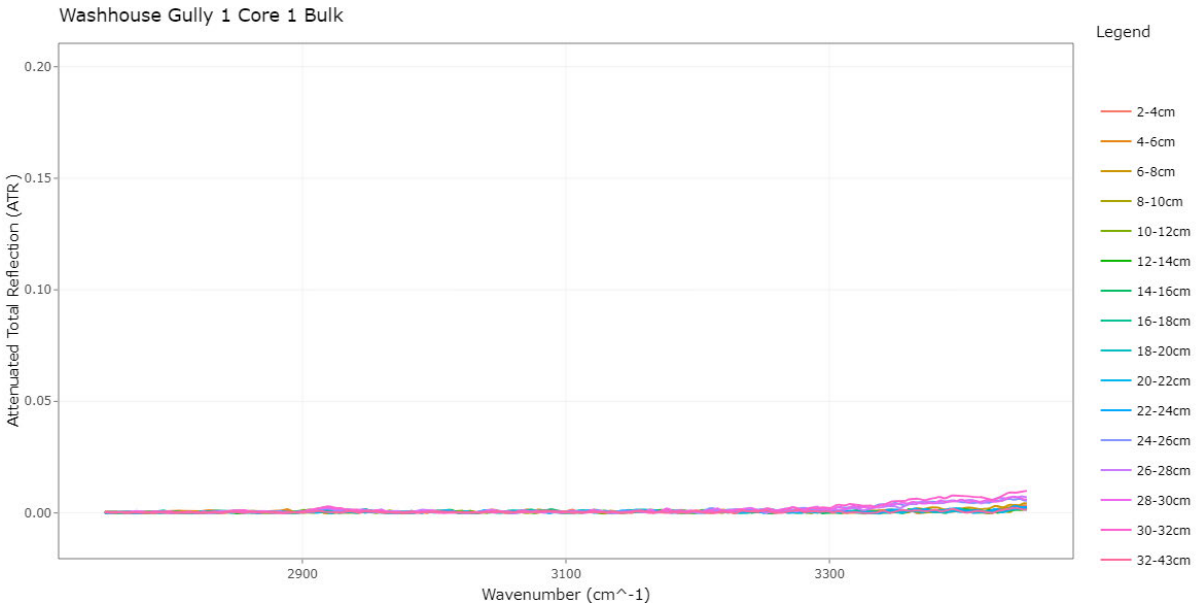

Figure D.9 Baseline-corrected ATR-FTIR spectra highlighting the bands at 3020-2800cm^{-1} and 3400cm^{-1} for the bulk fraction for Washhouse Gully 1 Core 1. No deviation from background is evident in this band.

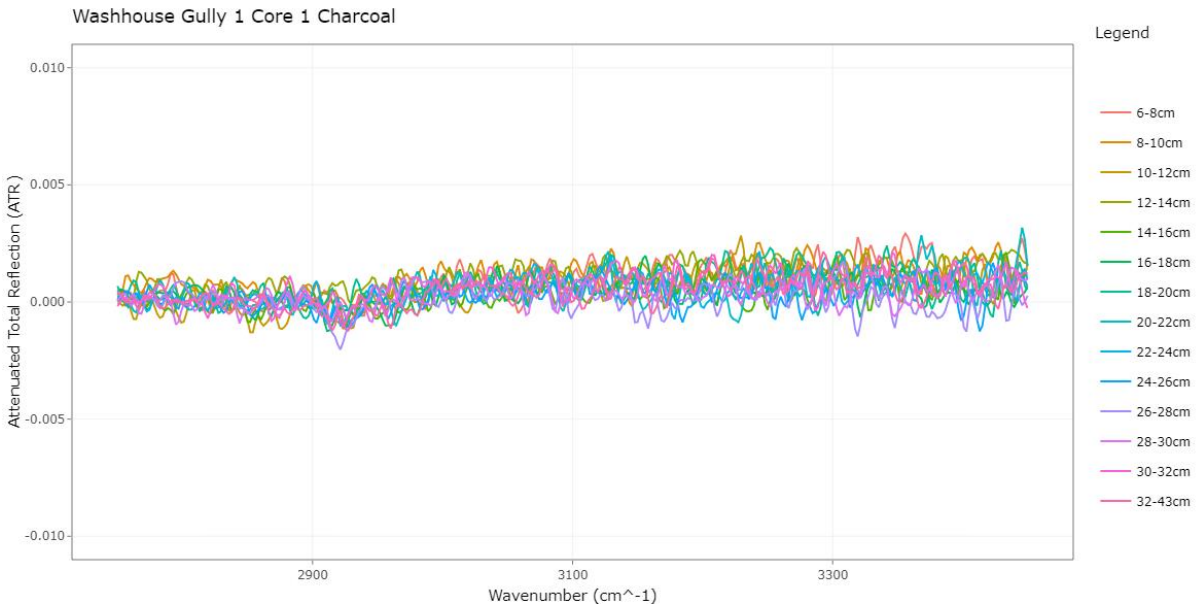

Figure D.10 Baseline-corrected ATR-FTIR spectra highlighting the bands at 3020-2800cm^{-1} and 3400cm^{-1} for the charcoal fraction for Washhouse Gully 1 Core 1. No deviation from background is evident in this band.

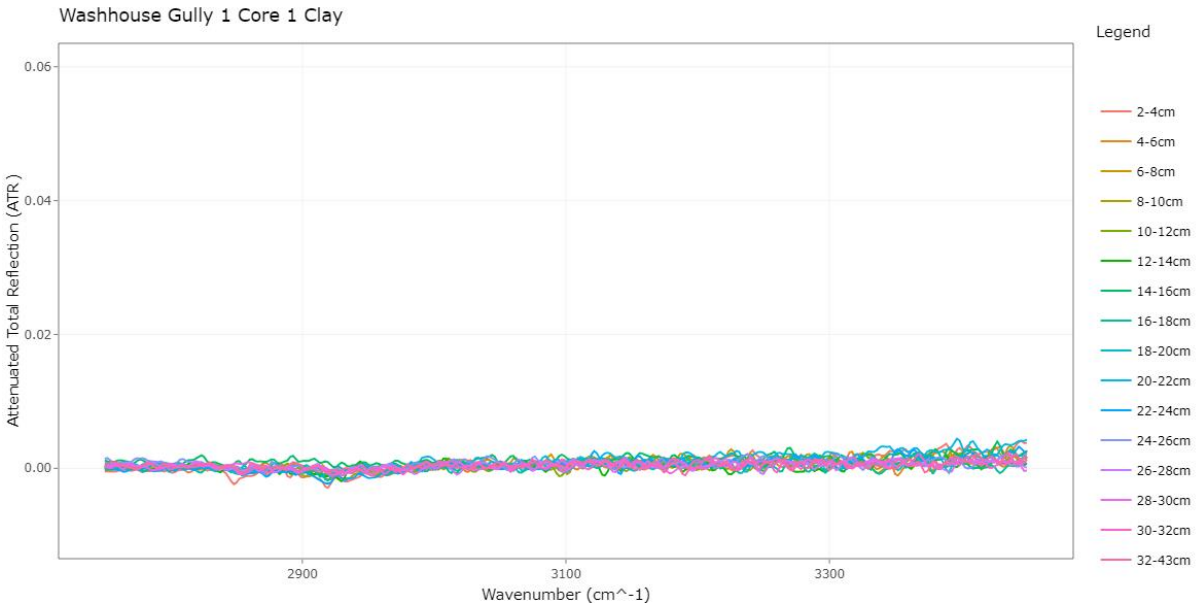

Figure D.11 Baseline-corrected ATR-FTIR spectra highlighting the bands at 3020-2800cm^{-1} and 3400cm^{-1} for the clay fraction for Washhouse Gully 1 Core 1. No deviation from background is evident in this band.

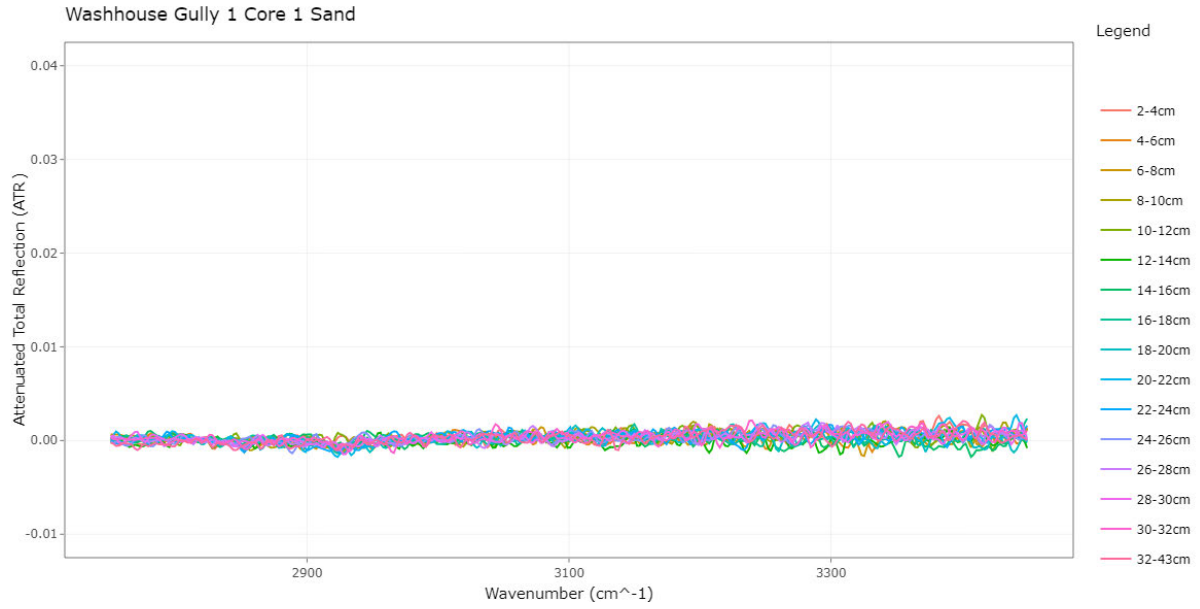

Figure D.12 Baseline-corrected ATR-FTIR spectra highlighting the bands at 3020-2800cm^{-1} and 3400cm^{-1} for the sand fraction for Washhouse Gully 1 Core 1. No deviation from background is evident in this band.

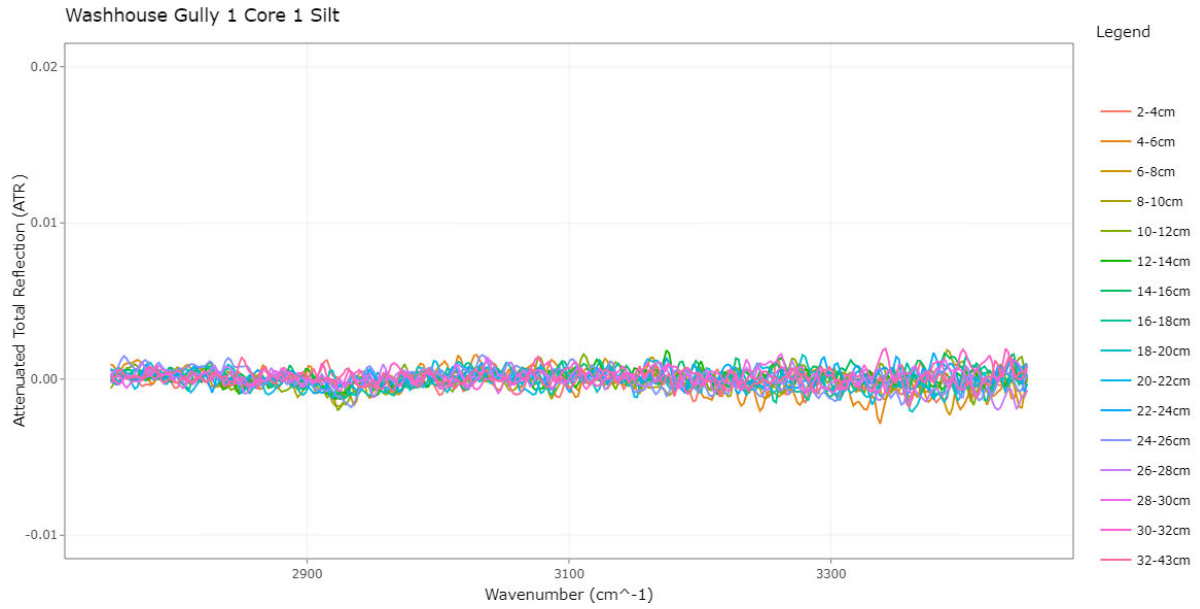

Figure D.13 Baseline corrected spectra highlighting the bands at 3020-2800cm^{-1} and 3400cm^{-1} for the silt fraction for Washhouse Gully 1 Core 1. No deviation from background is evident in this band.

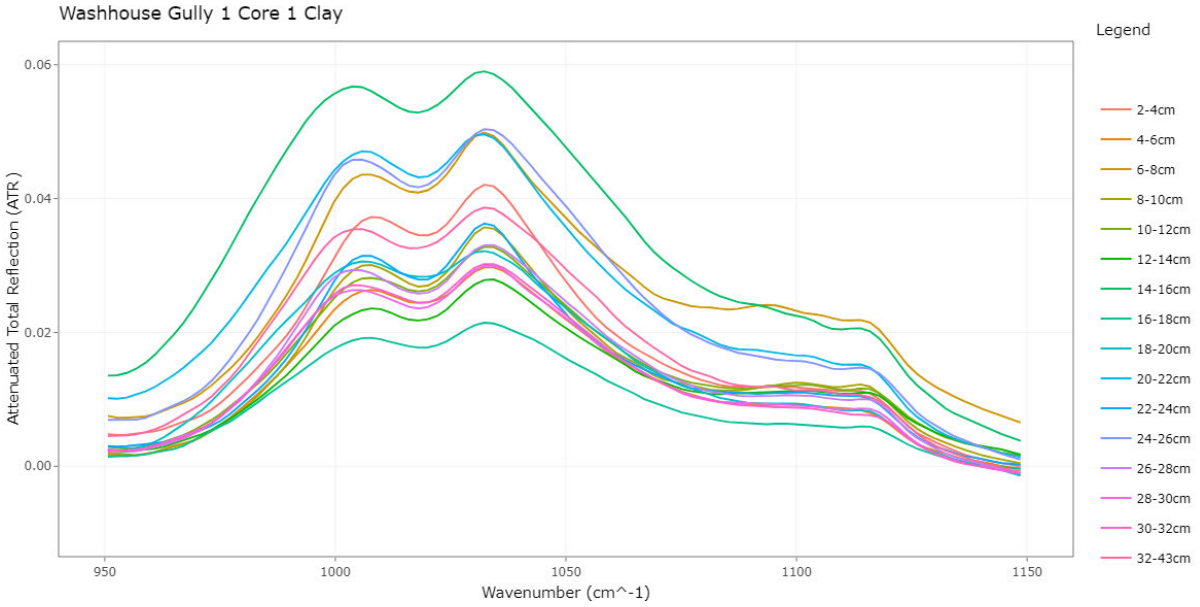

Figure D.14 Baseline corrected spectra highlighting the bands at 1095cm^{-1} for the clay fraction for Washhouse Gully 1 Core 1. No significant trend is evident between sample types.

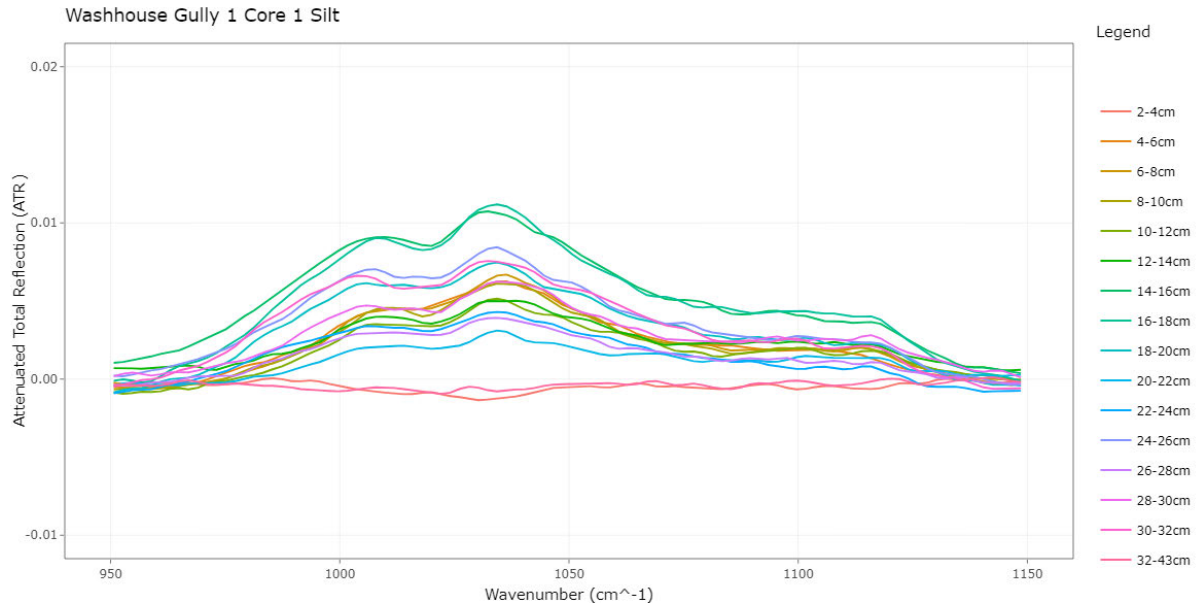

Figure D.15 Baseline-corrected ATR-FTIR spectra highlighting the bands at 1095cm^{-1} for the silt fraction for Washhouse Gully 1 Core 1. No significant trend is evident between sample types.

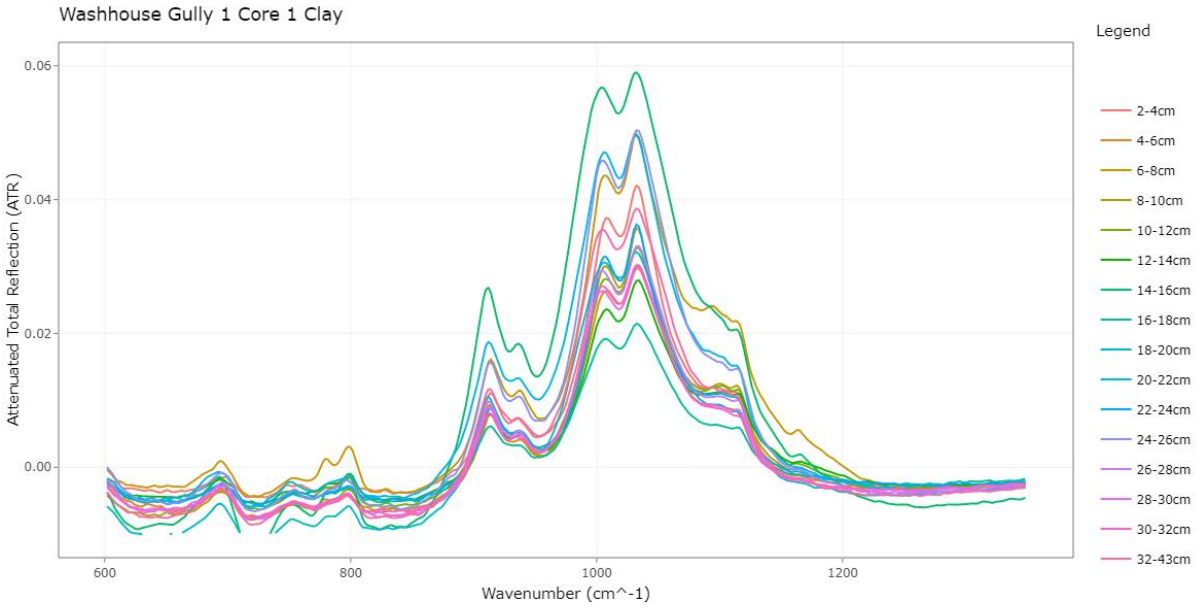

Figure D.16 Baseline-corrected ATR-FTIR spectra highlighting the bands around 800-600, 900-700 and 1300-1000 cm^{-1} for the clay fraction from Washhouse Gully 1 Core 1 as a function of depth. No significant trend is evident between samples.

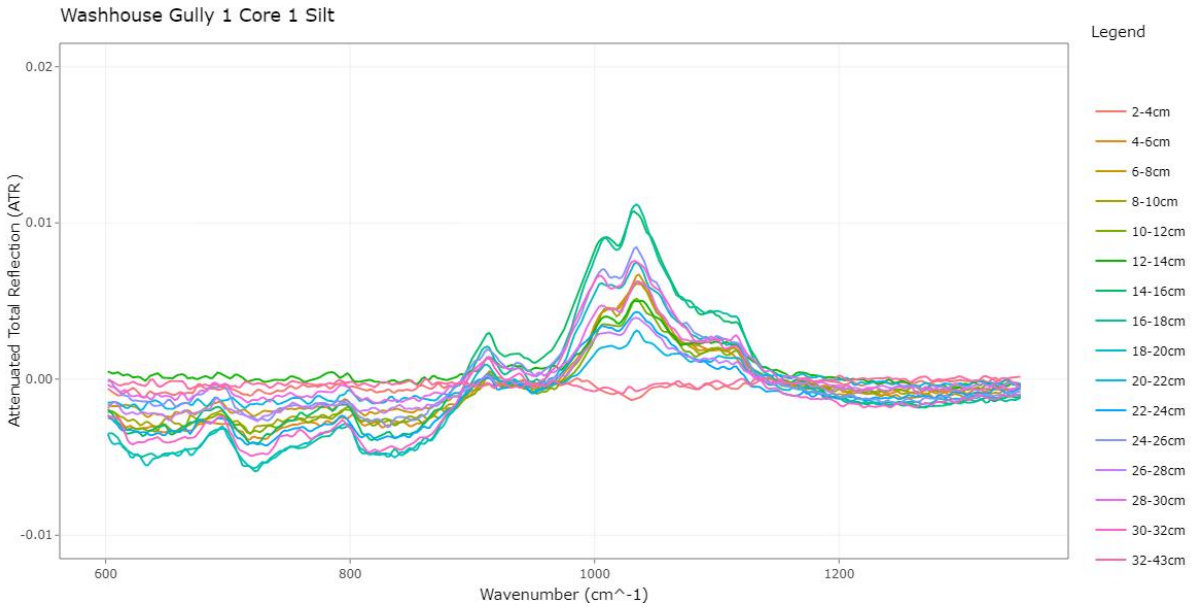

Figure D.17 Baseline-corrected ATR-FTIR spectra highlighting the bands around 800-600, 900-700 and 1300-1000 cm^{-1} for the silt fraction from Washhouse Gully 1 Core 1 as a function of depth. No significant trend is evident between samples.

Table 6 Core moisture content data for Washhouse Gully 1 Core 1. Charcoal-rich layers have the most significant increase in moisture content contrast with the remainder of the core.

Sample No.	Depth (cm)	Moisture Content (%)
1	2-4	25.45
2	4-6	30.33
3	6-8	34.64
4	8-10	30.36
5	10-12	20.53
6	12-14	23.45
7	14-16	27.93
8	16-18	25.94
9	18-20	26.21
10	20-22	26.98
11	22-24	33.63
12	24-26	39.54
13	26-28	39.59
14	28-30	44.80
15	30-32	38.04
16	32-43	27.36

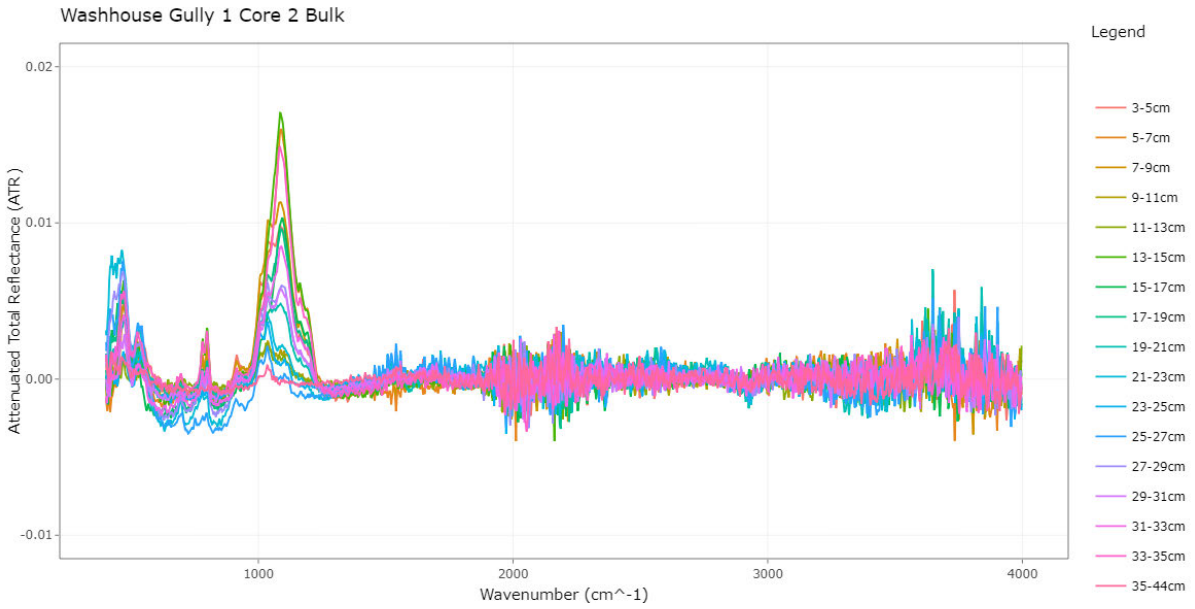

Figure D.18 Complete (4000-400cm^{-1}) baseline-corrected ATR-FTIR spectra for the Washhouse Gully 1 Core 2 bulk fraction as a function of depth.

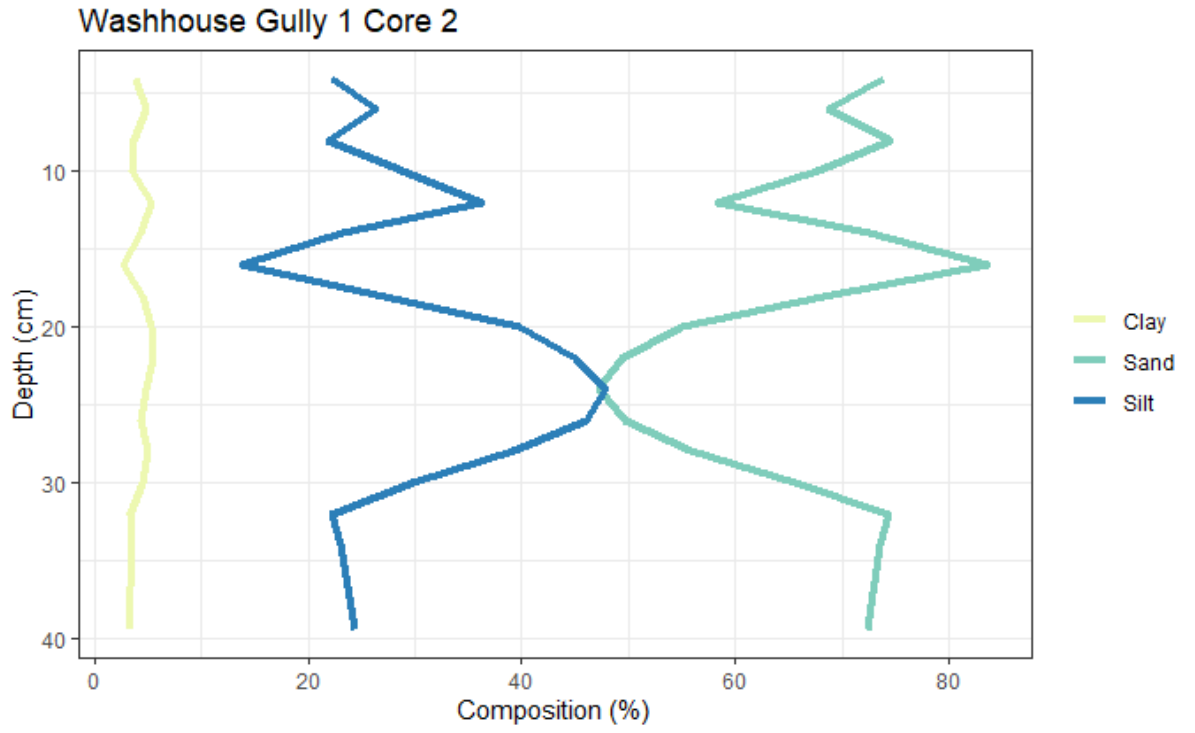

Figure D.19 Grain size data for Washhouse Gully 1 Core 2, highlighting the changes in clay (yellow), sand (green) and silt (blue) as a function of depth.

Table 7 Core moisture content data for Washhouse Gully 1 Core 2.

Sample No.	Depth (cm)	Moisture Content (%)
1	3-5	22.35
2	5-7	23.36
3	7-9	34.05
4	9-11	41.45
5	11-13	36.33
6	13-15	24.60
7	15-17	25.47
8	17-19	29.31
9	19-21	32.47
10	21-23	44.21
11	23-25	50.93
12	25-27	49.87
13	27-29	38.81
14	29-31	30.34
15	31-33	27.16
16	33-35	24.74
17	35-44	27.90

Appendix E R Codes

```
```{r WG1C1 Baseline Correction Clay}
#Convert to matrix
WG1C1clayt_matrix <- as.matrix(WG1Core1clayt_imp[ ,-1])
WG1C1claytBL <- baseline(WG1C1clayt_matrix[1,, drop=FALSE])
plot(WG1C1claytBL)
WG1C1clay_matrix2 <- matrix(nrow = nrow(WG1C1clayt_matrix), ncol = ncol(WG1C1clayt_matrix))
for (i in 1:nrow(WG1C1clayt_matrix)){
  WG1C1clay_BL<- baseline(WG1C1clayt_matrix[i,, drop=FALSE])
  x <- WG1C1clay_BL@corrected
  WG1C1clay_matrix2[i, ] <- x
}

# change name of the rows and columns
colnames(WG1C1clay_matrix2) <- colnames(WG1C1clayt_matrix)
rownames(WG1C1clay_matrix2) <- rownames(WG1C1clayt_matrix)
write.csv(WG1C1clay_matrix2,"WG1C1clayNewBL.csv")
plot(WG1C1claytBL)


```
```

Figure E.1 Rmarkdown code used for baseline-correction of all FTIR spectra using the baseline package (Liland, Mevik and Canteri, 2020).

```
```{r WG1C1 Clay Plot}
WG1C1_clay <- read_xlsx("WG1C1 clay BLC.xlsx",2)
colnames(WG1C1_clay) <- c('Wavenumber', '2-4cm', '4-6cm', "6-8cm", "8-10cm", "10-12cm",
"12-14cm", "14-16cm", "16-18cm",  "18-20cm", 20-22cm", "22-24cm", "24-26cm", "26-28cm",
"28-30cm", "30-32cm", "32-43cm")

# "melt" data frames so can plot data per depth
WG1C1clay <- melt(WG1C1_clay, id.var="Wavenumber")

# plot data
p3 <- ggplot(WG1C1clay, aes(Wavenumber, value, color = variable)) +
  xlim(400, 4000)+
  ylim(-0.01, 0.04)+
  geom_line()+ theme_bw() +
  labs(x="Wavenumber (cm^-1)", y="Attenuated Total Reflection (ATR)",
       color = "Legend", title="Washhouse Gully 1 Core 1 Clay")
ggplotly(p3)
```
```

Figure E.2 Rmarkdown code used for formulation of plots using the ggplot2 package (Wickham, 2016).